Universal parallel transmission pulse design for the human brain and spinal cord MRI at 9.4T

Dissertation

der Mathematisch-Naturwissenschaftlichen Fakultät

der Eberhard Karls Universität Tübingen

zur Erlangung des Grades eines

Doktors der Naturwissenschaften

(Dr. rer. nat.)

vorgelegt von

Ole Geldschläger

aus Stralsund

Tübingen

2021

Gedruckt mit Genehmigung der Mathematisch-Naturwissenschaftlichen Fakultät der Eberhard Karls Universität Tübingen.

Tag der mündlichen Qualifikation:	22.12.2021
Dekan:	Prof. Dr. Thilo Stehle
1. Berichterstatterin:	Prof. Dr. Anke Henning
2. Berichterstatter:	Prof. Dr. Klaus Scheffler

Erklärung:

Ich erkläre, dass ich die zur Promotion eingereichte Arbeit mit dem Titel:

“Universal parallel transmission pulse design for the human brain and spinal cord MRI at 9.4T“

selbständig verfasst, nur die angegebenen Quellen und Hilfsmittel benutzt und wörtlich oder inhaltlich übernommene Stellen als solche gekennzeichnet habe. Ich versichere an Eides statt, dass diese Angaben wahr sind und dass ich nichts verschwiegen habe. Mir ist bekannt, dass die falsche Abgabe einer Versicherung an Eides statt mit Freiheits-strafe bis zu drei Jahren oder mit Geldstrafe bestraft wird.

I hereby declare that I have produced the work entitled:

“Universal parallel transmission pulse design for the human brain and spinal cord MRI at 9.4T“

submitted for the award of a doctorate, on my own (without external help), have used only the sources and aids indicated and have marked passages included from other works, whether verbatim or in content, as such. I swear upon oath that these statements are true and that I have not concealed anything. I am aware that making a false declaration under oath is punishable by a term of imprisonment of up to three years or by a fine.

Tübingen, den 30. Dezember 2021

Datum Unterschrift

Acknowledgements

With the following sentences, I would like to thank various people without whose support I never would have become a Philosophiae Doctor (PhD).

First of all, I am deeply grateful to my entire family and especially to my parents Anett und Holger. Thank you for supporting me in each and every step from the beginning of my life, until now and in the future. I hope if you read the German abstract of this thesis, you can get a little insight of what I was doing during the past five years.

Further, I want to thank my love Heleni. Your support and motivation drove me forward, but was making the moments before each trip from Vorpommern to Tübingen quite difficult. Our relationship started just before the beginning of this PhD project. However, the end of this PhD project is definitely not the end of our personal project.

I am grateful to my supervisor Prof. Anke Henning for giving me the opportunity to do this PhD project, to travel to various places all over the world and to meet so many interesting people during the past five years. To her, and to my co-supervisor Prof. Klaus Scheffler, I would like to say thank you for your advice and fruitful discussions.

I am very grateful to all my friends and colleagues at the Max-Planck-Institute in Tübingen: Johanna, Theresia, Loreen, Pavi, Andrew and Tamás. Every lunch break was entertaining. The retreats were awesome. Thank you Nikolai for helping me with every coil problem I had. I thank Mark for all our cake and coffee sessions during the afternoons in Greifswald. I want to thank Tingting for opening me the world of pTx.

My special and from the technical point of view, most important thanks goes to my friend and colleague Dario. I am deeply impressed by your knowledge and your enthusiasm for the scanner. Thank you for being open to all my questions, for all the discussions and endless hours at the scanner. I am convinced that this thesis would not exist today in the current form without your help.

Danksagung

Mit den folgenden Zeilen, möchte ich verschiedenen Menschen danken ohne deren Unterstützung ich niemals ein Philosophiae Doctor (PhD) geworden wäre.

Zuallererst, bin ich meiner gesamten Familie und insbesondere meinen Eltern Anett und Holger zutiefst dankbar. Danke, dass ihr mich von Beginn meines Lebens an, bis jetzt und auch in Zukunft bei jedem einzelnen Schritt unterstützt habt und weiterhin werdet. Ich hoffe, wenn ihr die deutsche Zusammenfassung dieser Arbeit lest, bekommt ihr zumindest einen kleinen Einblick davon womit ich mich in den vergangenen fünf Jahren beschäftigt habe.

Weiterhin, möchte ich meiner geliebten Heleni danken. Deine Unterstützung und Motivation trieben mich an, auch wenn es die Momente vor jeder Reise von Vorpommern nach Tübingen besonders schwer gemacht hat. Zwar begann unsere Beziehung kurz bevor ich dieses PhD Projekt angefangen habe, aber das Ende dieses PhD Projektes wird garantiert nicht das Ende unseres persönlichen Projektes sein.

Ich bin sehr dankbar gegenüber meiner Betreuerin Prof. Anke Henning, dass sie mir die Möglichkeit für dieses PhD Projekt gegeben hat, ich zu verschiedenen Orten auf dieser Welt reisen konnte und so viele interessante Leute traf. Ihr, und meinem Zweitbetreuer Prof. Klaus Scheffler, möchte ich danken für ihre Hinweise und hilfreichen Diskussionen.

All meinen Freunden und Kollegen am Max-Planck-Institut in Tübingen bin ich sehr dankbar: Johanna, Theresia, Loreen, Pavi, Andrew und Tamás. Jede Mittagspause war unterhaltsam. Die Retreats waren genial. Danke an Nikolai, für die Hilfe bei jeglichen Spulen-Problemen. Ich danke Mark für alle Kuchen und Kaffee Treffen an den Nachmittagen in Greifswald. Ich möchte Tingting danken, dafür dass er mir die pTx Welt eröffnet hat.

Mein besonderer und von fachlicher Seite aus mein mit Abstand größter Dank geht an meinen Freund und Kollegen Dario. Ich bin echt beeindruckt wie viel du über den Scanner weißt und mit welchem Enthusiasmus du bei der Sache bist. Danke, dass du dir immer Zeit für all meine Fragen genommen hast, für die ganzen Diskussionen und

für die endlosen Stunden am Scanner. Ich bin davon überzeugt, dass es diese Arbeit ohne deine Hilfe heute so nicht geben würde.

Contents

Abstract

Magnetic resonance imaging is a powerful, non-invasive technology to acquire anatomical images from the human body. Operating at a magnetic field strength of 7T or higher (i.e. ultrahigh field (UHF)) provides a higher signal-to-noise ratio, facilitates higher spatial resolutions, and potentially improves diagnostic sensitivity and specificity compared to clinical field strength, such as 1.5T or 3T.

Unfortunately, UHF is accompanied with technical hurdles, from which the most problematic is the inhomogeneity in the radiofrequency transmit field. That can lead to spatially varying flip angles and, thus, to signal dropouts, local brightening or spatially altering imaging contrast.

The most flexible approach to address this issue is the parallel transmission (pTx) technique, which itself has the disadvantage of a lengthy calibration procedure. To overcome the calibration procedure the ‘universal pTx pulse’ (UP) concept was introduced. It is a radiofrequency pulse design concept that relies on a pre-collected design database. The resulting pulses then work on a wide cohort of subjects without recalibration.

As a first step, in this PhD project the advantages of imaging the human spinal cord at UHF were exploited. It was possible to acquire the first images from the human spinal cord at an ultrahigh in-plane resolution of 0.15x0.15mm^2 at 9.4T. The images showed the tiny structures of the spinal cord in great detail. The signal-to-noise ratio and T_2^*-times in the human spinal cord at 9.4T were presented.

Furthermore, in this thesis the UP concept was further developed, in order to use UHF and the pTx technique more widely.

While UPs were originally introduced for whole-brain or slice selective excitation, in this work a feasibility study for UPs for local excitation in the human brain (i.e. exciting only specific regions of the brain, while others should experience no excitation) was performed. UPs that locally excite the visual cortex area were calculated. The underlying transmit k-space trajectory for these radiofrequency pulses were ‘spiral’ trajectories. These local excitation UPs were successfully tested in vivo on non-database subjects at 9.4T.

In a next step, the UP performance was further improved by optimizing the underlying transmit k-space trajectory to match the excitation target. The trajectory optimization and the UP design algorithms have been implemented into an open source software package (called OTUP) and demonstrated using simulations and in vivo experiments at 9.4T. The code was tested for three different target excitation pattern with varying complexity.

Zusammenfassung

Die Magnetresonanz Bildgebung ist ein bedeutendes, nicht invasives Verfahren um anatomische Bilder des menschlichen Körpers zu erhalten. Das Verwenden einer Feldstärke des Hauptmagnetfeldes von 7T oder höher (sog. Ultrahoch Feld (UHF)) ermöglicht höhere Signal-zu-Rausch-Verhältnisse, räumlich höher aufgelöste Bilder und verbessert die diagnostische Genauigkeit verglichen zu klinischen Feldstärken, wie 1.5T oder 3T.

Leider ist das UHF verbunden mit einer Reihe von technischen Problemen, wovon das schwerwiegendste die Inhomogenität im Radio Frequenz Sendefeld ist. Dies kann zu räumlich sich unterscheidenden Flip- oder Anregungswinkeln führen und dadurch zu räumlich sich unterscheidenden Signalstärken auf den anatomischen Bildern.

Der flexibelste Ansatz um dieses Problem zu lösen ist die parallel transmission (pTx, ‚paralleles Senden' bzw. 'Übermitteln') Technik. Der Nachteil dieser Technik ist ihr langwieriges Kalibrierungsverfahren. Um die Kalibrierung zu umgehen, wurde das Konzept der ‚universellen pTx Pulse' (UPs) eingeführt. Dieses Radio Frequenz Puls Design Verfahren basiert auf einer vorher erfassten Design Datenbank. Der resultierende Puls funktioniert dadurch für eine große Probandengruppe ohne erneute Kalibrierung.

Als ersten Schritt dieses PhD Projektes wurden die Vorteile der UHF für die Bildgebung am menschliche Rückenmark genutzt. Mit einer Spule, die ursprünglich für die Anwendung am menschlichen Gehirn vorgesehen war, war es möglich ultrahoch aufgelöste Bilder (Auflösung von 0.15x0.15mm^2) vom Rückenmark zu erhalten. Diese Bilder zeigten detailliert die kleinen Strukturen des Rückenmarks. Die Signal-zu-Rausch-Verhältnisse und die T_2^*-Zeiten des menschlichen Rückenmarks bei einer Feldstärke von 9.4T wurden präsentiert.

Des Weiteren wurde in dieser Dissertation das UP-Konzept weiterentwickelt um UHF und das pTx Verfahren verstärkt in Kliniken einsetzen zu können.

Nachdem UPs ursprünglich dafür gedacht waren das gesamte Gehirn oder gezielt einzelne Schichten im Gehirn anzuregen, wurde in dieser Arbeit eine Studie über UPs für lokale Anregungen (d.h. es soll nur ein bestimmter Bereich im Gehirn angeregt

werden, während andere Bereiche explizit nicht angeregt werden sollen) durchgeführt. Es wurden UPs designt die lokal die Region des visuellen Cortex anregen. Die dabei zugrundeliegenden ‘sende’ k-Raum Trajektorien waren ‚spiral‘ Trajektorien. Die UPs wurden erfolgreich an Probanden getestet die nicht der Design Datenbank angehörten.

Im nächsten Schritt wurde die Performance der UPs weiter verbessert. Es wurde ein Verfahren präsentiert mit der die zugrundeliegenden ‚sende‘ k-Raum Trajektorien in Abhängigkeit der Zielanwendung optimiert werden konnten. Die Trajektorie Optimierung und der UP Design Algorithmus wurden in einem ‚Open Source‘ Software Paket (genannt OTUP) implementiert und anhand von Simulationen und 9.4T in vivo Experimenten demonstriert. Das gesamte Verfahren wurde an drei unterschiedlich komplexen Ziel-Anregungsmustern getestet.

1. Introduction

Magnetic resonance imaging (MRI) is a non-invasive method to image the human body, measure function and metabolism and derive clinical diagnoses.

The following chapter provides a basic background of MRI with a focus on ultra high field (UHF) (i.e. a main magnetic field (B_0) strength of equal or above 7T). It describes the great potential of UHF MRI to allow imaging of the human body in excellent spatial resolution and sharpness (section 1.1.). This potential was exploited in PUBLICATION 1 of this cumulative thesis, where images of human spinal cord were acquired at ultrahigh resolution (in-plane: 0.15x0.15mm^2).

Furthermore, the technical challenges UHF is accompanied with are introduced in this chapter. It provides the reader with an understanding of what these challenges are and how and why they arise at UHF (section 1.2.). As an approach to address these challenges, the technique of 'parallel transmission' (pTx) will be explained (section 1.2.). Section 1.3. describes the difference between the application of magnetic field gradients for the acquisition and the transmission case. Especially the latter is of high importance for pTx. Section 1.4. demonstrates how a pTx pulse can be designed.
Within the field of pTx, there is the concept of 'universal pulses' (section 1.5.). A powerful concept, PUBLICATION 2 and 3 were focused on.
Section 1.6. presents the research objectives of this thesis.

1.1. MRI basics and advantages of UHF

To understand the advantages of MRI at UHF, the underlying mechanisms of nuclear magnetic resonance (NMR) and MRI in general need to be discussed briefly. A more detailed overview can be found in the literature (1,2).

A hydrogen nucleus contains a single proton. Each proton possesses a spin. That means it rotates about its axis. The angular momentum of a rotating object is a vector and the direction of 'the vector indicates the axis of the rotational motion' (2). The direction of the

spin angular momentum is denoted as the spin polarization axis. In general, the polarization axes pointing in all possible directions in space (Figure 1):

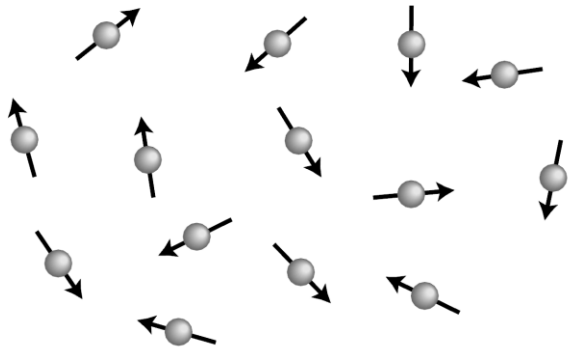

Figure 1: Randomly directed spin polarizations. Reprinted from Levitt M.H. (2) with permission of John Wiley & Son, Inc.

The proton has a magnetic moment and behaves like a small magnet, due to its positive electrical charge, the rotation and the spin. The direction of the magnetic moment of a proton is either the same direction as the spin polarization or the opposite direction. It depends on the gyromagnetic ratio γ, the ratio of the magnetic moment to the spin angular momentum. Different particle or systems of particle have different gyromagnetic ratios γ. In case of the hydrogen nucleus, the gyromagnetic ratio γ is 42.577 MHz/T (3). If γ is positive (as for the hydrogen nucleus), the magnetic moment points in the same direction as the angular momentum. If γ is negative, the magnetic moment points in the opposite direction.

Exposing the protons to an external magnetic field (B_0), the spins (i.e. the magnetic moment vectors) start to precess around the direction of the B_0 field (Figure 2).

The spins precess with a characteristic frequency, the so called Larmor frequency ω_0 (2):

$$\omega_0 = -\gamma B_0 \qquad \text{Eq. 1}$$

where γ is the gyromagnetic ratio and B_0 denotes the strength of the external magnetic field. As depicted in Eq. 1 the Larmor frequency ω_0 increases with increasing B_0 field strength.

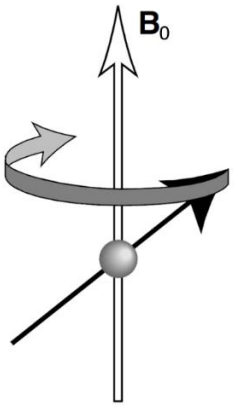

Figure 2: A proton spin precessing in an external magnetic field (B_0). Reprinted from Levitt M.H. (2) with permission of John Wiley & Son, Inc.

In an external magnetic field the magnetic moment vectors tend to align along the B_0 field. It is slightly more probable that the spins are driven towards an orientation with lower energy (parallel to B_0) than towards an orientation with higher energy (anti-parallel to B_0) (4). Thereby, an entire ensemble of spins gives rise to a small net magnetic moment along B_0. This state is called the thermal equilibrium (Figure 3).

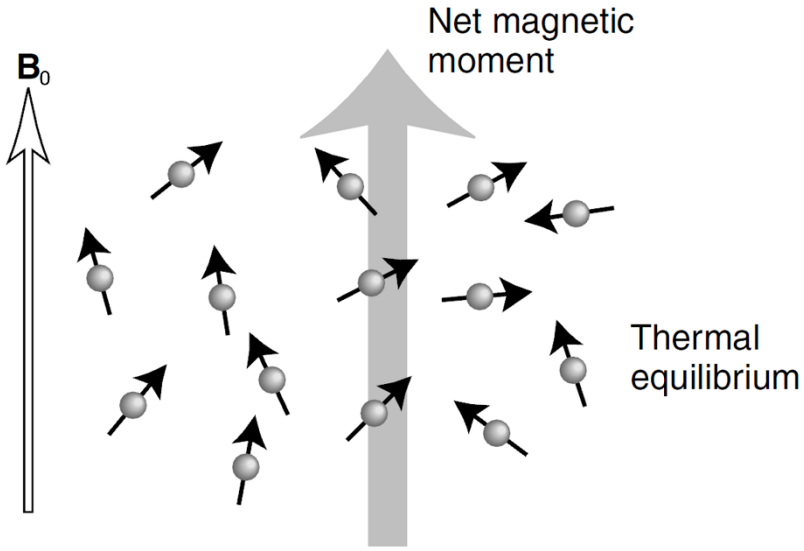

Figure 3: Thermal equilibrium. Reprinted from Levitt M.H. (2) with permission of John Wiley & Son, Inc.

The difference between the amount of spins (and their magnetic moments) aligned either parallel or anti-parallel to B_0 results in the useable net longitudinal magnetization. As the B_0 direction is often referred to as the z-axis, the net longitudinal magnetization is referred to as M_z.

Through application of a radiofrequency (RF) pulse (i.e. an electromagnetic wave of the same frequency as the Larmor frequency) the spins experience excitation. During this excitation process an entire spin ensemble absorb energy and become tipped away from the z-axis into the transverse xy-plane (i.e. the plane perpendicular to B_0 and the z-axis) (Figure 4). Thereby, the net longitudinal magnetization is also tipped into the transverse plane (Figure 4).

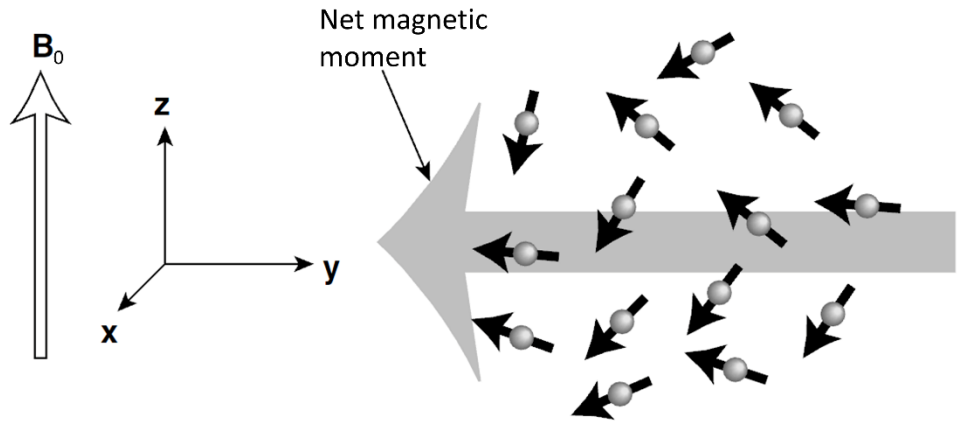

Figure 4: Polarization distribution after application of a RF pulse. Reprinted from Levitt M.H. (2) with permission of John Wiley & Son, Inc.

M_{xy} denotes the resulting net magnetization of the spin ensemble in the transverse plane. In the transverse plane, the spins (and through that the transverse magnetization) are rotating about the B_0-axis, thereby inducing an alternating voltage in a RF receiver coil (4). Acquiring and processing this signal, finally results in the MR image.

Theoretically, RF pulses can be designed to tip the spins with any desired flip angle between 0 and 180° (from the z-axis). A tip angle of 90° results in a M_z magnetization of 0.

To investigate the influence of a RF pulse on the magnetization of a spin system, the Bloch equations need to be considered. The Bloch equations are a set of macroscopic equations, describing the behavior of the nuclear magnetization as a function of time involving a RF pulse. The equations and how they were utilized in this work, can be seen in section 1.4.

By means of the 'Boltzmann-statistics' (1), the crucial advantage of MRI at UHF can be derived: With an increased B_0 field strength, the fraction of spins aligning parallel to the B_0 field is increased due to the higher energy gap between the spin states.

Therefore, the net longitudinal magnetization M_z is incremented. Consequently, the transverse magnetization is also incremented (after excitation) and a higher signal is induced in the receiver coil.

As visible in Figure 5, this effect causes an increased signal-to-noise ratio (SNR) (5,6) at higher B_0 field strengths.

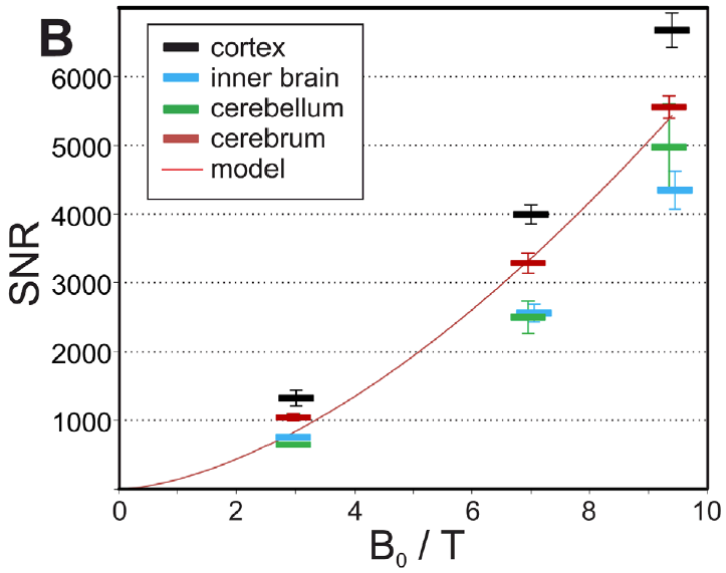

Figure 5: Intrinsic SNR_0 values in four different brain compartments. The red line represents fitting results on the SNR over the entire cerebrum as $SNR_0 = B_0^{1.65}$. Reprinted from Pohmann et al. (6) with permission of John Wiley & Son, Inc.

SNR increases superlinearly with the B_0 field strength (6,7) (Figure 5) and is consequently higher at UHF compared to lower fields. Additionally, SNR is directly proportional to the measured voxel size (8) of a MR acquisition. As a result, UHF enables the measurement of smaller voxel sizes, thereby increasing the spatial resolution of the anatomical images. In consequence, MR images acquired at UHF might reveal anatomical structures, which are not detectable at lower field strength.

The literature provides several studies, which compare 7T acquisitions of the human brain or the spinal cord (SC) with corresponding measurements at 3T (9,10,11). All previous work shows an excellent improvement of the image quality and diagnostic power of the 7T versus the 3T results. As an example, Figure 6 compares SC acquisitions at 3T and 7T. The improvement in the image quality from 3T to 7T for an in-plane resolution of 0.5x0.5mm^2 is clearly visible. Additionally, the increased SNR at 7T allows a higher resolution of 0.3x0.3mm^2 to further improve the image quality and potential diagnostic power.

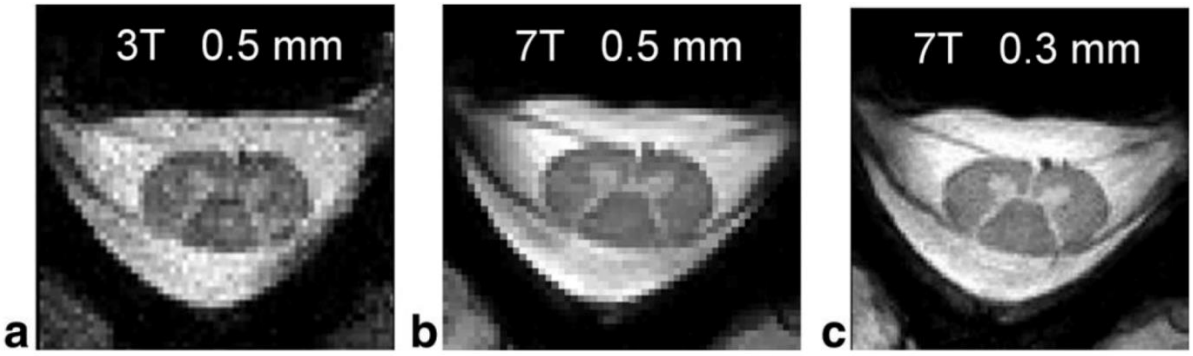

Figure 6: Comparison of transversal GRE images acquired at different B_0 field strengths and spatial resolutions. a: 3T, Res.: 0.5x0.5x3mm³. b: 7T, Res.: 0.5x0.5x3mm³. c: 7T, Res.: 0.3x0.3x3mm³. Reprinted from Zhao et al. (12) with permission of John Wiley & Son, Inc.

In some cases higher B_0 field strength can also result in an improved contrast-to-noise ratio between different tissue types (13). The contrast itself arise from different spin relaxation times for different tissue types. As PUBLICATION 1 quantified T_2^* times in the SC, the process of relaxation will be explained briefly.

Longitudinal (or T_1) relaxation (Figure 7) describes the process of the gradual realignment of the net magnetization with the outer magnetic field (z-axis along the scanner bore) after the RF pulse was applied. The parameter T_1 is the longitudinal relaxation time constant. T_1 increases with increasing B_0 field strength (6).

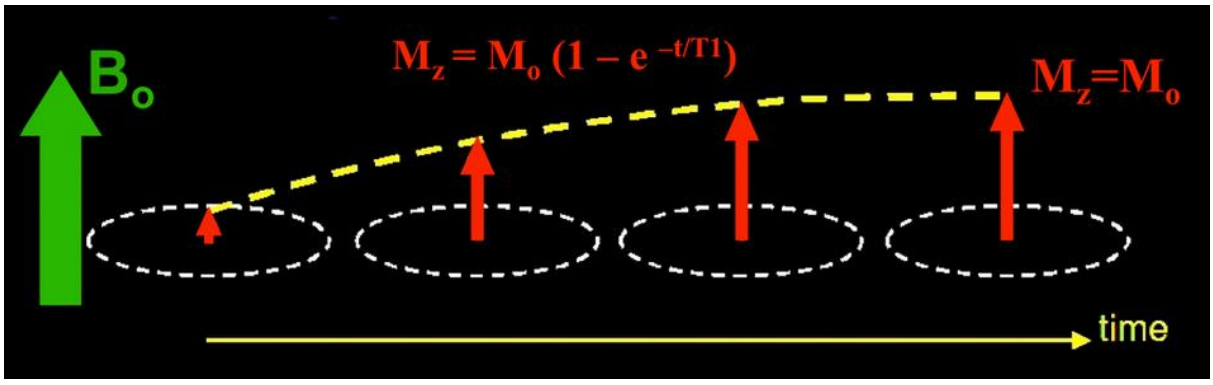

Figure 7: A symbolic depiction of T_1 relaxation, the process by which the net longitudinal magnetization (M_z) returns to its initial maximum value (M_0) after a RF pulse tipped the spins into the transversal plane. Courtesy of Allen D. Elster, MRIquestions.com.

Furthermore, directly after the application of a RF pulse the transverse magnetization is at its maximum because all spins have a coherent phase. Afterwards the spins start to dephase (i.e. the spins lose phase coherence) because of spin interactions. The transverse magnetization decays. This is the process of transverse (or T_2) relaxation

(Figure 8). The time constant T_2 characterizes the transverse relaxation and can be measured by spin echo series. It decreases with increasing B_0 field strength (6).

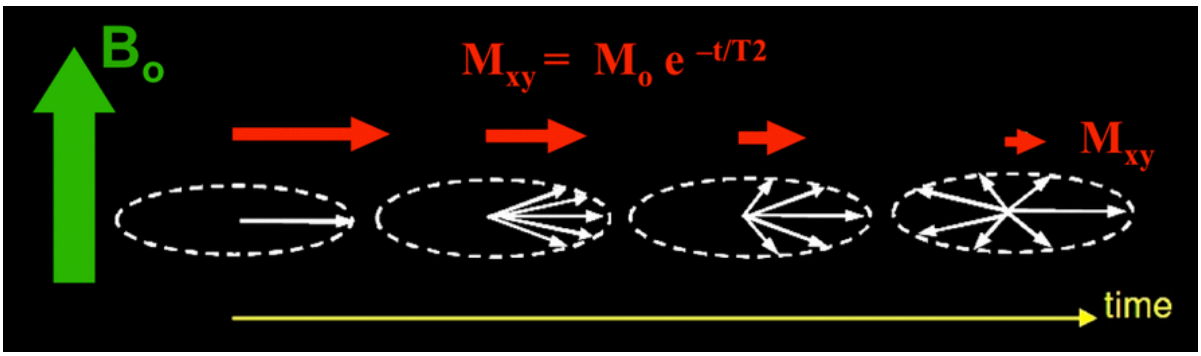

Figure 8: A symbolic depiction of T_2 relaxation, the process where the transversal magnetization (M_{xy}) decreases when the spins start to dephase after a RF pulse tipped the spins into the transversal plane. Courtesy of Allen D. Elster, MRIquestions.com.

Alternatively, the time constant T_2^* is often considered. This constant characterizes the signal decay after a single excitation pulse and is dominated by macroscopic and microscopic magnetic field inhomogeneity, which causes spin dephasing that can be refocused by spin echo pulses.T_2^* is always smaller than or equal to T_2 and decreases with field strength.

The mentioned advantages of UHF are accompanied with a set of technical hurdles. The following sections focus on these hurdles, as well as on a possible solution.

1.2. Technical challenges at UHF & parallel transmission principle

As described in section 1.1. RF pulses excite the spins and flips the respective magnetization vector away from the z-axis. At UHF certain technical challenges occur when the RF pulses are applied. The following section explain why these challenges arise and how they can be addressed.

Let B_1^+ denote the complex radiofrequency (RF) magnetic field created by a RF coil with N_T RF transmit elements. As Eq. 1 shows, the net B_1^+ field produced inside a sample is the superposition of the fields $B_{1,r}^+$ produced by each transmit element r, with $r = 1, \dots, N_T$ (14).

$$B_1^+(\boldsymbol{x},t) = \sum_{r=1}^{N_T} B_{1,r}^+(\boldsymbol{x},t) \qquad \text{Eq. 2}$$

where $\boldsymbol{x}$ is the spatial position of a voxel and t the time.

$B_{1,r}^+(\boldsymbol{x},t)$ can be separated as follows:

$$B_{1,r}^+(\boldsymbol{x},t) = p_r(t)S_r(\boldsymbol{x}) \qquad \text{Eq. 3}$$

where $p_r(t)$ is the RF pulse applied through transmit element r and $S_r(\boldsymbol{x})$ is the RF sensitivity of transmit channel r.

In a conventional 'single channel' system, all transmit elements of the RF coil are driven by the same transmit channel or amplifier (i.e. every transmit element applies the same pulse shape $p_r(t)$ with same amplitude). For single channel applications, the most frequently used transmit mode is the 'circularly polarized (CP) mode'. Herein, the same RF pulse is applied for each transmit element, with $360°/N_T$ phase shifts between adjacent channels. The phase shifts are achieved by utilizing RF cables of corresponding different lengths.

At lower fields, fixed transmit modes produce good MR images. However, at UHF the following problem occurs: Shorter electromagnetic wavelengths are necessary to excite spins precessing at higher Larmor frequencies. Thereby, wave interference effects (15,16) becoming more pronounced at UHF compared to lower field strengths. The consequence is severe inhomogeneity in the transmit sensitivities S_r. Figure 9 shows combined transmit sensitivity maps (often referred to as B_1^+ maps) acquired at 3T, 7T and 9.4T in the CP mode. While the 3T map is relatively homogeneous along the whole brain (except of at the periphery), the 9.4T map is immensely inhomogeneous with spatially varying sensitivities along the whole brain.

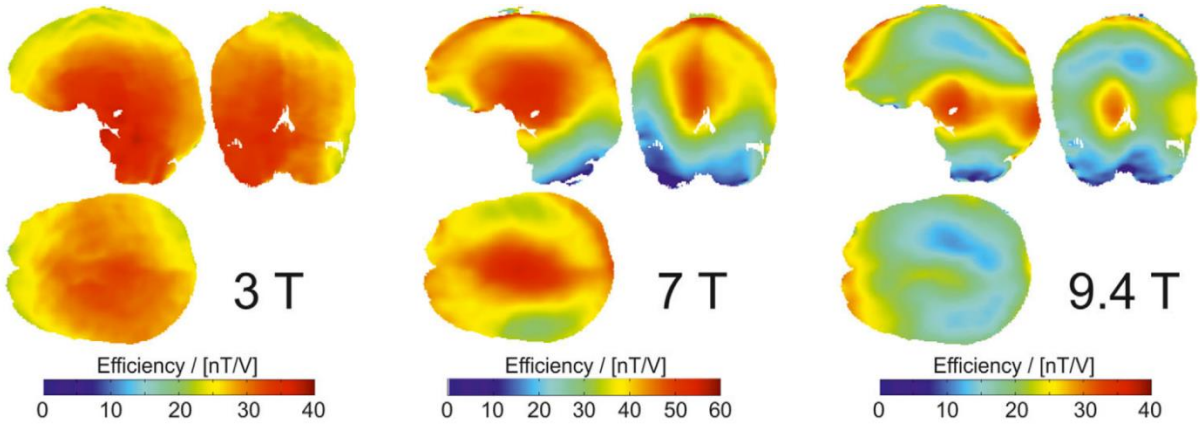

Figure 9: Transmit efficiencies of the coils used at 3T, 7T, and 9.4T. Different color scales were used to emphasize the B_1^+ homogeneity changes. Reprinted from Pohmann et al. (6) with permission of John Wiley & Son, Inc.

Due to the inhomogeneous transmit sensitivity maps at UHF, fixed modes such as the CP mode often produce spatially varying flip angles (FAs) in the scanned object. This results in spatial variations of the signal and tissue contrast in the final MR image as visible in Figure 10.

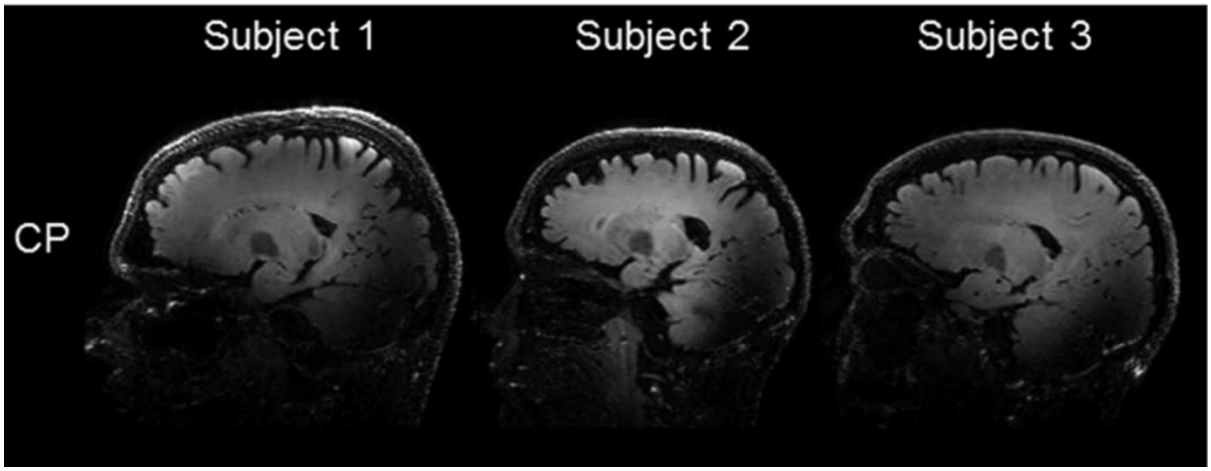

Figure 10: Sagittal image of a FLAIR-SPACE sequence acquired in CP mode at 7T. Reprinted from Gras et al. (17) with permission of John Wiley & Son, Inc.

The most promising approach to overcome this problem is the concept of 'parallel Transmission' (pTx) (18,19). Herein, each transmit element of the RF coil is driven by its own transmit channel, independently with 'full control over amplitude and phase modulation with microsecond temporal resolution' (14). This is achieved by individual RF pulse synthesizers and amplifiers for each transmit element, respectively. In contrast to the CP mode, each RF pulse $p_r(t)$ can have a completely different shape for each transmit element (Figure 11).

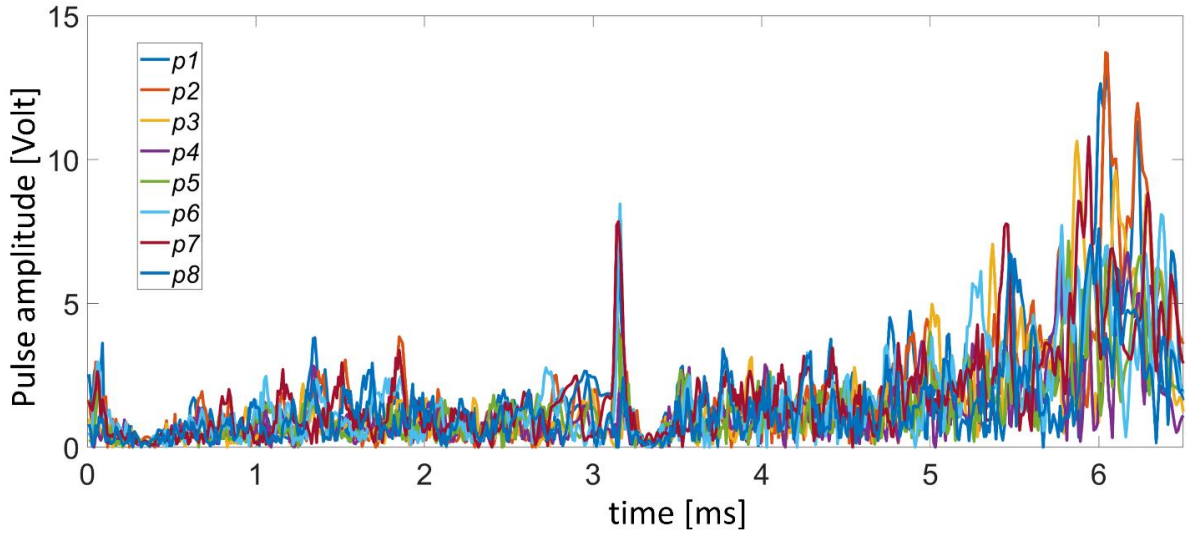

Figure 11: Amplitude of example RF pulses for $N_T = 8$ transmit elements each driven by its own transmit channel.

Because of these additional degrees of freedom in the pulse design (compared to a fixed transmit mode), pTx pulses enable improved performance for homogenous whole brain excitation or simultaneous multislice excitation (20). In addition, the pulse duration can often be reduced (18,19) through the application of multiple transmit channels.

By setting a corresponding target excitation pattern for the pulse design, pTx allows not only for whole brain, but also for 'local excitation' (LEx) (or inner volume) applications (21). LEx enables to reduce the field of view (FOV) by masking the tissues outside the FOV, which would otherwise fold into the image (22) (exploited in PUBLICATION 2). Consequently, LEx can reduce the total signal acquisition time and/or increase the spatial resolution, which is important for a range of clinical brain and body applications (23). LEx pulses were applied within various MR sequences for human brain and body measurements in the literature (24,25,26).

During this work, a 'pTx pulse' is referred to as the entire set of RF pulses for all N_T transmit elements. As explained in the following two sections, a pTx pulse is commonly designed based on a given transmit gradient waveform.

1.3. Gradient fields in acquisition versus transmission

Next to the applied RF pulse, the transmit gradient waveform and the resulting transmit k-space trajectory (see Figure 12 for an example waveform and the corresponding k-space trajectory) has a crucial role for pTx pulse design. Gradient waveforms are produced by gradient coils, which are loops of wire or conductive sheets inside the MR scanner bore. Passing an electric current through these coils produces an additional magnetic field (i.e. the gradient field). For x-, y- and z-direction one set of gradient coils is utilized, respectively. Depending on the current, it is possible to create various gradient field waveforms, based on which the k-space trajectory can be calculated (see section 1.4.).

The following section describes how gradient fields (and waveforms) are utilized in MRI in general and explains the difference between the acquisition and the transmission case.

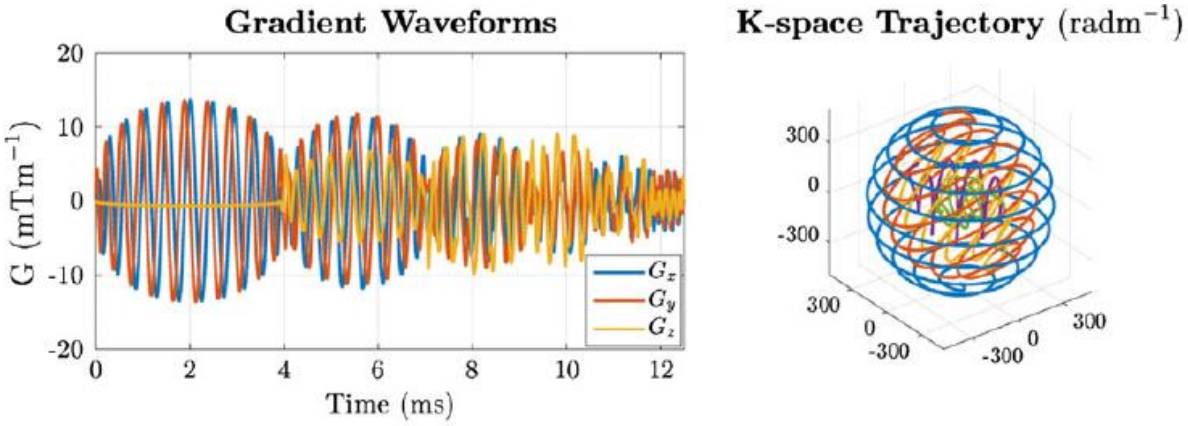

Figure 12: The gradient waveforms (left) result in a 3D shells excitation k-space trajectory (right) consisting of multiple nested shells. Figure reprinted with permission from Padormo et al. (14) with permission of John Wiley & Son, Inc.

In comparison to other imaging techniques as x-ray imaging or ultrasound, the signal detecting device in MRI (i.e. the RF receiver coil) cannot assign the location from where the signal origins. The signal the receiver coil detects origins from all voxels within the scanned sample. For that reason, a spatial encoding scheme is needed to form the MR image. Therefore, the B_0 field will be mildly 'distorted in a precise manner through the application of time-dependent magnetic field gradients' (27). There is one gradient coil that produces the linear field gradients along the x-, y- and z-direction,

respectively. The current in each gradient coil can be modulated independently yielding a specific maximum magnetic field gradient strength and slew rate. Through the application of these gradient fields the spins frequencies and phases in different voxel locations change in a predictable manner. Exploiting the processes of frequency and phase encoding in combination with Fourier transformation enables to assign a signal strength to each image voxel. Thereby, an anatomical image can be formed.

Next to their application in image acquisition, gradient fields can also be utilized in the transmission case for spatially selective excitation of certain spins inside the whole sample. Herein, varying gradient fields are combined with a simultaneously applied RF pulse that is specifically designed for a certain gradient waveform. Again, magnetic field gradients along all three spatial dimensions change the Larmor frequencies of the spins across the sample in a spatially dependent manner. If at the same time a specifically designed RF pulse is applied that only excites certain frequency bands, only spins in certain voxels across the whole volume become excited, while other may fall into stop bands of the pulse and thus experience no excitation. Only the spins that resonate with a frequency inside the pass band of the RF pulse experience excitation. The spins resonating with a frequency unequal to the frequency of the RF pulse experience no excitation.

In theory, transmit gradient fields could be combined with design of a single RF pulse (i.e. only one transmit channel). However, in general, transmit gradient fields are combined with pTx pulses as it increases the degrees of freedom through the application of multiple transmit channels simultaneously (18,19).

The consecutively altered gradient fields form a trajectory through the k-space. The k-space is a formalism representing the spatial frequency information of an object. For the transmit case it is referred to as transmit k-space. Accordingly, for the acquisition case it is denoted as acquisition k-space. The calculation of a transmit k-space trajectory out of a transmit gradient waveform will be explained in section 1.4. Furthermore, section 1.4. describes how a pTx RF pulse can be designed for a given target excitation flip angle pattern, based on a certain transmit gradient waveform and specific sensitivity maps.

1.4. Conventional pTx pulse design

The strategy exploited within the majority of pTx pulse design algorithms (14) is the ‘small tip angle’ (STA) approximation from Pauly et al. (28). A frequently used design algorithm constitutes the ‘spatial domain method’ from Grissom at al. (29).

At this point, the ‘spatial domain method’ will be explained briefly. It should provide the reader with a general insight into the Bloch equations and pTx pulse design. The ‘spatial domain method’ played a key role in PUBLICATION 2 and 3.

As already announced in section 1.1. the Bloch equations describe the nuclear magnetization as a function of time under the influence of a RF pulse. In the rotating frame of reference (i.e. a transformed coordinate system assuming the observer is rotating with the spins at the Larmor frequency) the Bloch equations are as follows (28):

$$\frac{d}{dt}\begin{pmatrix} M_x(\boldsymbol{x},t) \\ M_y(\boldsymbol{x},t) \\ M_z(\boldsymbol{x},t) \end{pmatrix} = \gamma \begin{pmatrix} 0 & \boldsymbol{G}(t)\boldsymbol{x} & -B_{1,y}^{+}(\boldsymbol{x},t) \\ -\boldsymbol{G}(t)\boldsymbol{x} & 0 & B_{1,x}^{+}(\boldsymbol{x},t) \\ B_{1,y}^{+}(\boldsymbol{x},t) & -B_{1,x}^{+}(\boldsymbol{x},t) & 0 \end{pmatrix} \begin{pmatrix} M_x(\boldsymbol{x},t) \\ M_y(\boldsymbol{x},t) \\ M_z(\boldsymbol{x},t) \end{pmatrix} \qquad \text{Eq. 4}$$

where $\boldsymbol{x}$ is the spatial position of a voxel and t denotes the time. $M_x(\boldsymbol{x},t)$ describes the x component of the magnetization and analog for y and z. $\boldsymbol{G}(t)$ is the transmit gradient waveform and $B_{1,x}^{+}(\boldsymbol{x},t)$ and $B_{1,y}^{+}(\boldsymbol{x},t)$ are the real and imaginary component of the complex RF magnetic field $B_1^{+}(\boldsymbol{x},t)$ from Eq. 2 in section 1.2. The RF pulse is incorporated in $B_1^{+}(\boldsymbol{x},t)$ (see Eq. 3 from section 1.2.).

Notably, in the full Bloch equations spin relaxation effects (longitudinal and transverse relaxation) are incorporated. For the sake of simplicity they are neglected herein.

Assuming a RF pulse is tipping the spins with only a small tip angle away from the z-axis, Pauly et al. (28) presented that the Bloch equations can be approximated by the following term (the so called small tip angle approximation):

$$m(\boldsymbol{x},T) = i\gamma m_0 \int_0^T B_1^{+}(\boldsymbol{x},t) e^{i\gamma \Delta B_0(\boldsymbol{x})(t-T)} e^{i\boldsymbol{x}\cdot\boldsymbol{k}(t)} dt \qquad \text{Eq. 5}$$

where $m(\boldsymbol{x},T) = M_x(\boldsymbol{x},T) + i\, M_y(\boldsymbol{x},T)$ is the final transverse magnetization in the voxel at the spatial position $\boldsymbol{x}$ after the pulse of length T was applied**,** γ is the

gyromagnetic ratio, m_0 is the equilibrium magnetization magnitude and ΔB_0 is the main magnetic field map (in short: B_0 map). A central part of Eq. 3 is the transmit k-space trajectory $\boldsymbol{k}(t)$:

$$\boldsymbol{k}(t) = -i\gamma \int_t^T \boldsymbol{G}(s)ds \qquad \text{Eq. 6}$$

where $\boldsymbol{G}$ is the already mentioned transmit gradient waveform.

Pauly et al. are referring to a tip angle as small if it is up to 30°. However, they also state that the concept can 'still work well for tip angles on the order of 90°' (28).

According to Grissom's 'spatial domain method' (29) utilizing Eq. 2 and Eq. 3 from section 1.2. Eq. 5 modifies to:

$$m(\boldsymbol{x},T) = i\gamma m_0 \sum_{r=1}^{N_T} S_r(\boldsymbol{x}) \int_0^T p_r(t) e^{i\gamma \Delta B_0(\boldsymbol{x})(t-T)} e^{i\boldsymbol{x}\cdot\boldsymbol{k}(t)}\, dt \qquad \text{Eq. 7}$$

where N_T constitutes the number of transmit channels, each with a unique sensitivity map $S_r(\boldsymbol{x})$ (often called B_1^+ map) and RF pulse $p_r(t)$.

Through discretizing space and time and restructuring Eq. 7 further, it can be expressed as matrix multiplication:

$$\boldsymbol{m} = \boldsymbol{A}\boldsymbol{p} \qquad \text{Eq. 8}$$

where $\boldsymbol{m}$ is the vector of the transverse magnetization for each voxel, $\boldsymbol{A}$ is the system information matrix, containing all information on S_r, ΔB_0 and $\boldsymbol{k}(t)$ and $\boldsymbol{p}$ is a concatenation of RF pulses $p_r(t)$ from each transmit element.

By specifying a target magnetization pattern $\boldsymbol{m}_{tar}$, Eq. 8 can be exploited to create the following optimization problem:

$$\boldsymbol{p}^* = \arg\min_{\boldsymbol{p}} \{\| \boldsymbol{A}\boldsymbol{p} - \boldsymbol{m}_{tar} \|^2\} \qquad \text{Eq. 9}$$

Solving this problem designs the final pTx RF pulse $\boldsymbol{p}^*$.

This approach is capable to produce well-performing pTx pulses. However, there is one striking disadvantage: For each pulse, the sensitivity maps S_r and B_0 map needs to be measured for each subject. Only afterwards, the pulse calculation can start. This time-consuming process of acquisition and RF pulse calculation takes usually between

10 and 15 minutes (30) and needs to be executed while the subject is already positioned inside the scanner. That hinders the pTx technique from being widely used in the clinics.

1.5. Universal pulse concept

2017, Gras et al. (31) introduced the concept of 'Universal pTx pulses' (UPs). As UPs were investigated in PUBLICATION 2 and 3, the general idea of this concept will be discussed briefly.

The motivation for the UP concept consists in the circumvention of the subject specific calibration (i.e. measuring the sensitivity maps S_r and B_0 map) and pulse calculation procedure. First, a set of B_0 and sensitivity maps from a representative subject cohort is measured in order to build up a database for the pulse design. Based on this database a pTx pulse is calculated that works robustly on all of the subjects contained in the design database. Due to the similarity of these maps for most human subjects (see Figure 13), the calculated pulses (i.e. the UPs) then also perform well on subjects, which were not contained in the design database (31).

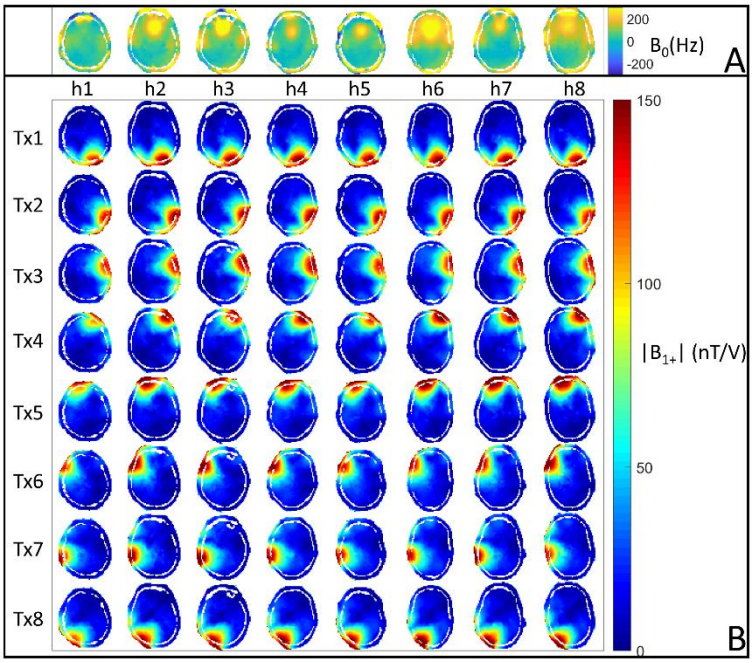

Figure 13: A: Measured B_0 map of the central transversal slice of heads from eight different subjects in Herz. B: Measured sensitivity (B_1^+) map from each transmit

channel of the central transversal slice of heads from eight different subjects in nano Tesla per Volt.

Notably, the UPs can be applied on non-database subjects without further measurements or pulse optimizations. The performance of the UPs is just slightly worse compared to subject specific tailored pulses (see Figure 14).

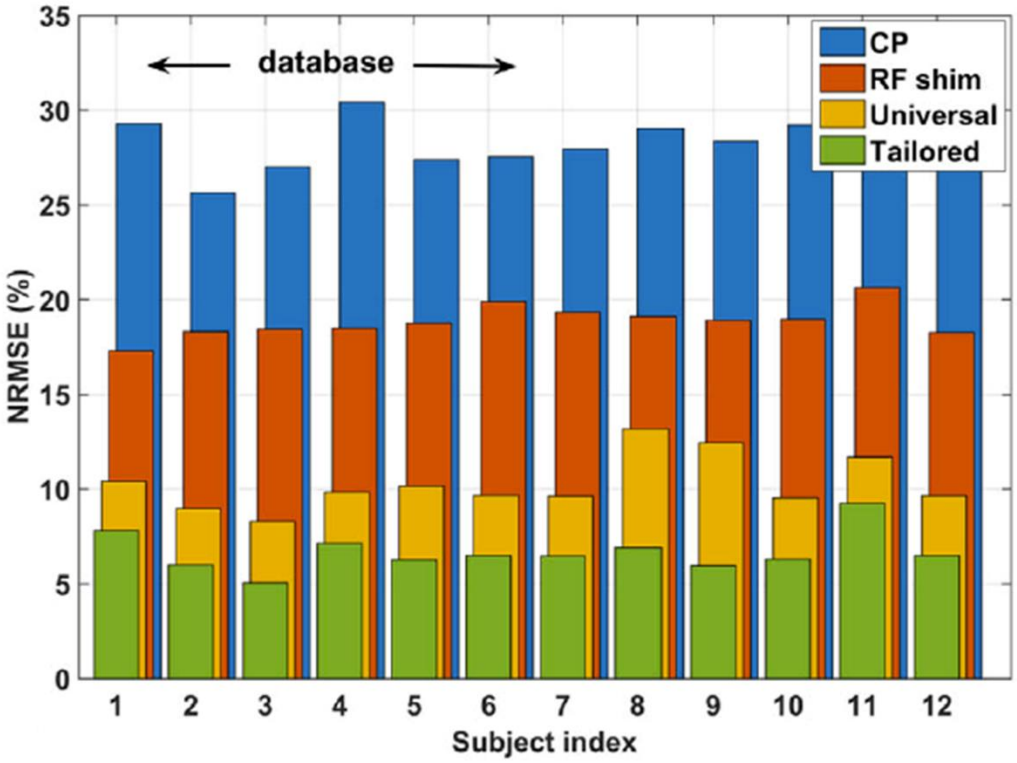

Figure 14: Comparison of normalized root mean squared error values for whole brain excitation pulses on heads of 12 different subjects at 7T (blue: CP-mode, orange: RF shim, yellow: universal pulse calculated based on subjects 1-6, green: subject specific tailored pulses). Reprinted from Gras et al. (31) with permission of John Wiley & Son, Inc.

For nonselective (i.e. whole brain) and slice selective pulses the benefit and reliability of this concept has been proven extensively (17,32,33,34). As an example, Figure 15 displays acquisitions with the same sequence and subjects as in Figure 10, but herein an UP was applied instead of the CP mode. These three subjects were not contained in the design-database for that UP. However, the UP enables a more uniform excitation of the entire brain, respectively, compared to the CP mode (Figure 10).

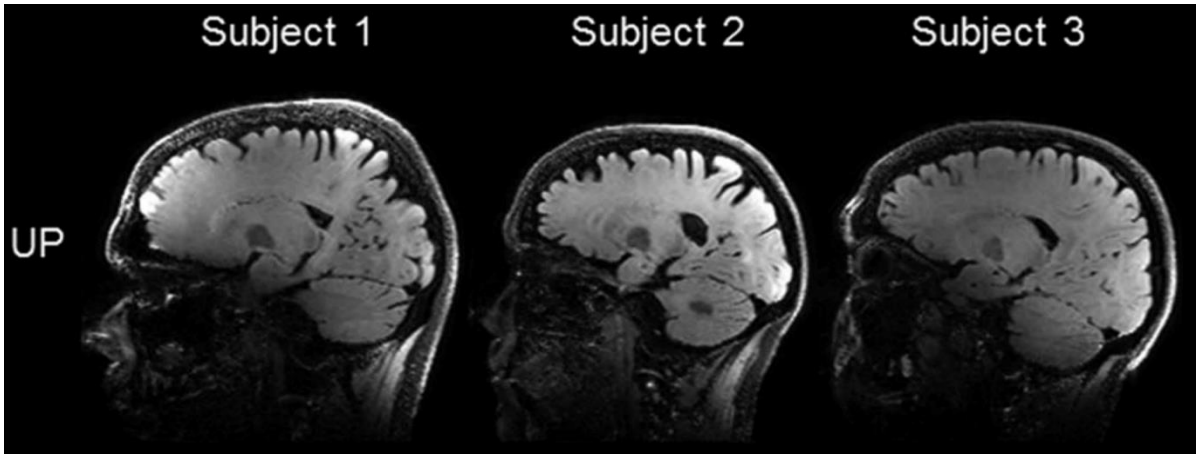

Figure 15: Sagittal image of a FLAIR-SPACE sequence acquired with an UP at 7T. The presented subjects were not contained in the design database of that UP. Reprinted from Gras et al. (17) with permission of John Wiley & Son, Inc.

1.6. Research Objectives

The thesis focused on exploiting the advantages of MRI at UHF (PUBLICATION 1), as well as on addressing the accompanied technical hurdles of UHF by utilizing the pTx technique with UPs (PUBLICATION 2 and 3).

In the first project (PUBLICATION 1) the first human spinal cord (SC) in vivo acquisitions at the B_0 field strength of 9.4T were presented. The goal of this study was to image the cervical SC in an ultrahigh spatial in-plane resolution of 0.15x0.15mm^2. Furthermore, different B_0 shimming routines were compared and T_2^* relaxation time maps of the spinal cord at 9.4T were calculated. Algorithmic SC segmentation was tested. Imaging the SC at UHF was of high practical relevance, because tiny anatomical structures were visible herein. Moreover, at 9.4T structures as the anterior median fissure and posterior median septum were recognizable. These structures were only hardly detectable at 7T and were not detectable at lower field strengths.

In the second and third project (PUBLICATION 2 and 3) it was investigated with ‘universal pTx pulses’ in order to circumvent the lengthy subject specific calibration and pulse calculation procedure which is inherent to conventional pTx applications. Both projects contributed to complement and extend the general concept of UPs and to facilitate the wider adoption of the pTx-technique in clinical practice.

The objective of the second project (PUBLICATION 2) was to show the feasibility of using the UP-concept for local excitation applications in the human brain. Recent studies proved the concept only for whole brain or slice-selective excitation. However, in PUBLICATION 2 UPs were calculated, that locally excited the visual cortex area in the human brain, while the surrounding tissues experienced only minor excitation. These pulses were especially useful because they allowed reduced field-of-view applications on non-database subjects. With a reduced field-of-view it was possible to save scan time or to keep the scan time constant while imaging the region of interest at an improved spatial resolution.

In the third project (PUBLICATION 3) the transmit k-space trajectories for UPs were optimized in dependence of the specific excitation target.

The resulting UPs from PUBLICATION 2 and 3 were applied in vivo at 9.4T on non-database subjects. In order to show their reliability, the UP acquisitions were compared with images, acquired with subject specific tailored pulses.

Finally, an open source software package (called OTUP) integrated the algorithmic advances of PUBLICATION 2 and 3.

2. Publication summaries

This PhD thesis is written as integrated accumulation of publications. This chapter summarizes the three publications. Notably, while in PUBLICATION 2 and 3 the pTx technique was used, in PUBLICATION 1 each measurement was performed utilizing the CP mode (i.e. in the single channel mode). The full articles are appended in chapter 7. All in vivo measurements shown and utilized in the three publications were acquired at a 9.4T whole-body human MR scanner ('Magnetom 9.4T', Siemens Healthcare, Erlangen, Germany).

2.1. Ultrahigh-resolution quantitative spinal cord MRI at 9.4T

This section summarizes PUBLICATION 1.

Introduction

Due to its excellent soft tissue contrast, MRI is the diagnostic imaging technique of choice for spinal cord (SC) related diseases, such as multiple scleroses (35,36), amyotrophic lateral sclerosis (37) or SC injury (38). Operating at UHF (≥7T) is crucial for SC imaging because of the already mentioned advantages of UHF MRI for SNR and measured voxel size (see introduction chapter, section 1.1.). The small diameter of the cord (~1cm) (39) necessitates high spatial resolution in the millimeter and submillimeter range to make the small structures within the cord (gray matter, white matter, nerve roots,..) visible and distinguishable.

The literature provides several examples, which show the improved SC image quality at 7T compared to images acquired at lower fields (10,11,12) (see Figure 6 in the introduction chapter).

To take it a step further, this publication presented the first in vivo human SC MR images at 9.4T. In this work, T_2^* weighted gradient-echo (GRE) images with an improved spatial

resolution compared to the 7T acquisitions from the literature (10,40,41) were acquired. The echo time of a GRE sequence was optimized in order to maximize the contrast between gray and white matter within the SC. B_0 shimming methods were compared for SC imaging. Algorithmic SC segmentation was tested and T_2^* times of gray and white matter in the cervical SC at 9.4T were calculated.

Methods

All measurements were performed with an in house built 16-channel tight-fit array coil (42). It consisted of eight transceiver surface loops and eight receive only loops perpendicular to the surface loops.

This coil, originally constructed for human brain scans, provided enhanced SNR in deep brain structures, what was the motivation for using this coil also for imaging the cervical SC. Additionally, this coil had a cylindrical geometry with openings at top and bottom. Thereby, it was possible to place the subject further inside the coil than originally intended and to position the cervical SC in the array center.

During RF transmission, the coil was driven in CP mode. Ten healthy volunteers were measured.

Anatomical images were acquired with an axial T_2^* weighted GRE sequence. Various SC images with different settings and sequence parameters were acquired for the following purposes:

- B_0 shimming comparison:
  Along the SC the B_0 field varies dramatically because of the transitions between bone and intervertebral discs (43). For that reason, four different shimming algorithms (or settings) were performed to compare their influence on the SC image quality. The shimming routines were: the vendor implemented image-based shim routine, FASTESTMAP (44), ConsTru (45) and the TuneUp shim.
- Calculation of the intrinsic signal-to-noise ratio:
  To create intrinsic SNR maps (‘the SNR that would be obtained with a homogeneous FA of 90°, an infinite repetition time and an echo time of zero’ (6)) signal and noise measurements were performed consecutively. SNR was computed with the phased array root-sum-of-squares magnitude image combination (46).

- Sequence parameter optimization and high-resolution anatomical images:
  Various echo times (TEs) were applied in order to optimize this sequence parameter. The acquisitions from different TEs were combined to MEDIC (multi echo data image combination) (47) images. Ultrahigh resolution SC images (0.15x0.15mm^2 in-plane) were acquired.
- Segmentation:
  Algorithmic SC detection, as well as GM/WM segmentation, was tested.
- T_2^*-time calculation for gray matter and white matter:
  By means of the SC acquisitions with different TEs, T_2^* maps were calculated. The T_2^* times from GM and WM were averaged.

Results

High resolution anatomical SC images could be obtained at 9.4T. The individual investigations revealed the following results:

- B_0 shimming comparison:
  The vendor implemented shim routine offered the images with best quality.
- Calculation of the intrinsic signal-to-noise ratio:
  The SNR values in the SC were mostly between 6600 and 8060.
- Sequence parameter optimization and high-resolution anatomical images:
  Figure 16 depicts enlargements from the spinal cord acquisitions at different TEs and the MEDIC images. TEs between 9 and 13.8ms provided a good compromise between tissue contrast and minimal magnetic susceptibility effects. The MEDIC images delivered the highest contrast between gray and white matter. The high resolution images Figure 17) showed the SC in excellent quality and allowed for a clear distinction of gray and white matter. Tiny structures including nerve roots, blood vessels, anterior median fissure, posterior median septum were also recognizable.

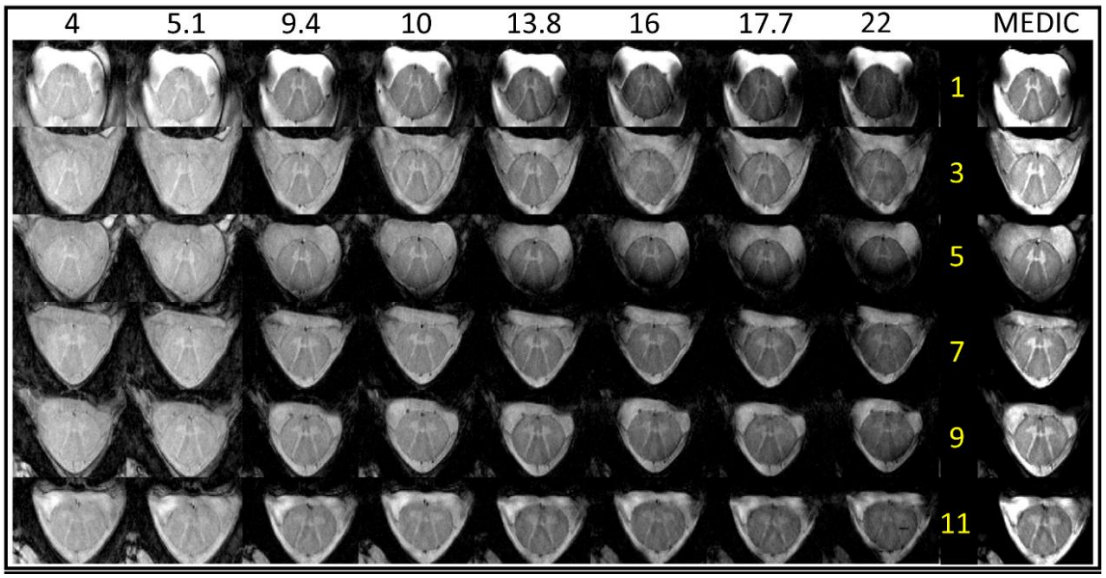

Figure 16: Enlargements of the spinal cord. Each column presents the measurements from different slices (slice number displayed by yellow numbers, every second slice is skipped) at a certain TE (depicted at the header in ms). Each row presents measurements from the same slice position, but at a different TE. The very right column of images show scaled multiecho data image combination (MEDIC) images calculated as the sum of squares from the eight measurements from the table of images. Reprinted from Geldschläger et al. (48) (PUBLICATION 1) with permission of John Wiley & Son, Inc.

- Segmentation:

  Algorithmic SC detection and GM/WM segmentation worked reliably.

- T_2^*-time calculation for gray matter and white matter:

  The resulted, averaged T_2^* values for GM (WM) in the cervical SC at 9.4T were 24.88ms ± 6.68ms (19.37ms ± 8.66ms). Figure 18 depicts an example slice from a T_2^* map.

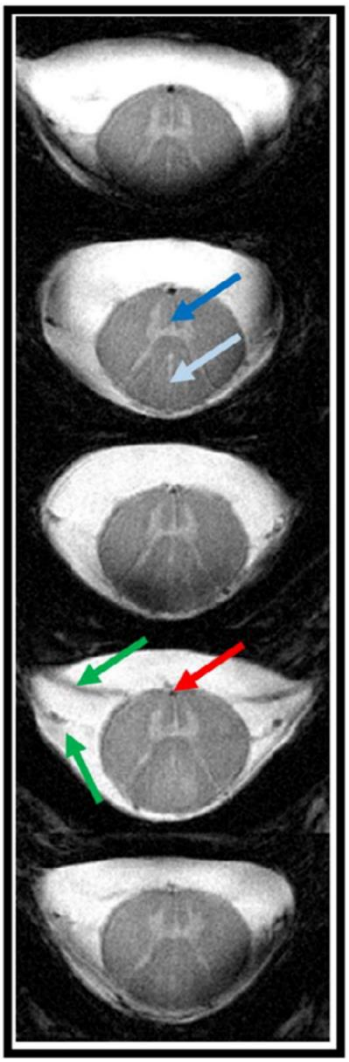

Figure 17: 9.4T spinal cord images acquired with a GRE sequence (in-plane resolution: 0.15×0.15 mm²). Nerve roots (green arrows), blood vessels (red arrow), the anterior median fissure (dark blue arrow) and the posterior median septum (sky blue arrow) are marked. Reprinted from Geldschläger et al. (48) (PUBLICATION 1) with permission of John Wiley & Son, Inc.

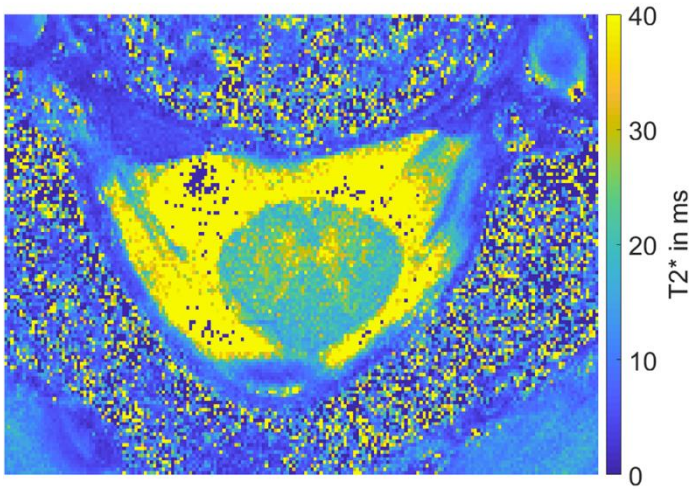

Figure 18: Enlargement at the spinal cord position of an example slice from a T_2^* map. Reprinted from Geldschläger et al. (48) (PUBLICATION 1) with permission of John Wiley & Son, Inc.

Discussion

The first in vivo MR images of the human SC acquired at 9.4T were presented. The highest in-plane resolution of 0.15x0.15mm^2 outperformed the recent 7T acquisitions (0.18x0.18mm^2). Visibility of nerve roots was improved compared to 7T results. Anterior median fissure and the posterior median septum were visible at 9.4T, while only hardly detectable at 7T.

The calculated SC T_2^*-times were (as expected) slightly lower compared to 7T and similar to T_2^*-times in the brain at 9.4T.

Although the proposed RF coil was originally intended for human brain applications, it produced excellent images from the human cervical SC. In consequence, there is no costly development of a SC dedicated coil needed to image the cervical SC.

The resulted intrinsic SNR values in the SC are slightly below comparable values in the human brain. However, this may be explainable with the suboptimal coil loading due to the subject repositioning for SC measurements.

Conclusion

The first step into human SC research using 9.4T MRI was performed. It was possible to generate excellent ultrahigh resolution images with an actual brain coil. UHF imaging of the human SC might open new possibilities in SC research and clinical patient care.

2.2. Local excitation universal parallel transmit pulses at 9.4T

This section summarizes PUBLICATION 2.

Introduction

The advantages and accompanied technical hurdles of operating at UHF MRI were already discussed in the introduction chapter of his thesis (section 1.1. and 1.2.). The most promising approach to address these hurdles is pTx. To circumvent the lengthy calibration process usually needed for pTx scan sessions, the UP concept was introduced (31). All previous studies investigating UPs have in common, that they present UPs for whole brain or slice selective excitation, based on 'spokes' (49) or 'kT-points' (50) as the underlying transmit k-space trajectory.

The goal of PUBLICATION 2 was to investigate the concept of UPs for LEx at 9.4T. The utilized transmit k-space trajectory were 'spiral' (51) and 'stack-of-spirals' (52) trajectories. The advantages of LEx were already discussed in the introduction of this thesis (section 1.2.).

Methods

To design UPs, an extension of the 'spatial domain method' (29) explained in the introduction of this thesis, was utilized. Instead of incorporating transmit sensitivity maps (i.e. B_1^+ maps) and B_0 maps only from one subject in the pulse design as usually done for the 'spatial domain method', the maps from all database subjects were included. Analog to Eq. 9 from section 1.4., the optimization problem was extended as follows:

$$\boldsymbol{p}_{UP}^{*} = \arg\min_{\boldsymbol{p}} \left\{ \left\| \left| \begin{bmatrix} \boldsymbol{A}_{full,1} \\ \vdots \\ \boldsymbol{A}_{full,N_{DB}} \end{bmatrix} \boldsymbol{p} \right| - \begin{bmatrix} \boldsymbol{m}_{tar} \\ \vdots \\ \boldsymbol{m}_{tar} \end{bmatrix} \right\|^2 \right\} \qquad \text{Eq. 10}$$

where $\boldsymbol{p}_{UP}^{*}$ is the final UP, $\boldsymbol{A}_{full,i}$ is the system information matrix from subject i from the database, N_{DB} is the number of subjects in the database and $\boldsymbol{m}_{tar}$ is the desired target excitation pattern which is aimed to create on each subject.

The optimization problem in Eq. 10 was solved performing two steps. First, the least-squares optimization (53) was applied (as in the spatial domain method (29)). Notably, with the least-squares method, it is not possible to exclude the phase of the resulting excitation profile from the optimization, however, the profiles phase was of no interest during this study. For that reason, in the second step, the least squares result was used as an initial guess for the active-set algorithm implemented in Matlabs (MathWorks, Natick, MA) *fmincon*-function. Within the cost function for the active-set algorithm, only the magnitude of the profiles was considered (Eq. 10). By means of the active-set algorithm, the solution was constrained to a maximum voltage of 130.

Two different UPs were designed. UP2D aimed to excite the visual cortex region in the central transversal slice of a head (by means of a 2D target pattern) with a target flip angle (FA) of 90 degree (FA90). The remaining areas within the target slice should not be excited. UP2D was non-slice-selective and had a fixed duration of 7.96ms using a 2D spiral-in k-space trajectory (54,51).

Analogously, UP3D aimed to excite the visual cortex area with FA90, but by means of a 3D target pattern (i.e. incorporating the entire head) and based on a 3D stack-of-spiral-in trajectory (52) (pulse duration 8.18ms).

In order to create UPs for small tip angles, the resulting UPs for FA90 were scaled down proportionally to generate pulses with a FA of 7° (FA7).

The UP performances were compared with subject specific tailored pTx pulse (TP) performances on non-database heads. The TPs were calculated using the conventional ‘spatial domain method’ (i.e. the profiles phase was incorporated herein).

All pulses were tested in simulations and in vivo in the human brain at 9.4T. The FA7 pulses were applied in a T_2^* weighted GRE sequence. The FA90 pulses were applied in a presaturated TurboFLASH sequence. UP3D for FA7 was applied within GRE sequence with a reduced FOV.

The pulse design database contained B_1^+/B_0 maps from eight different subjects.

Results

UP2D

As Figure 19 displays, simulations and in vivo results were similar for UP2D and the respective 2D TPs. Both excited the visual cortex area, while the remaining areas experienced only minor excitation. The respective 2D TPs delivered only a slightly better performance compared to the UP2D performance. The mean normalized root mean squared error (NRMSE) of UP2D on three non-database heads (FA7 and FA90) was ~0.069 for UP2D and ~0.034 for the TPs.

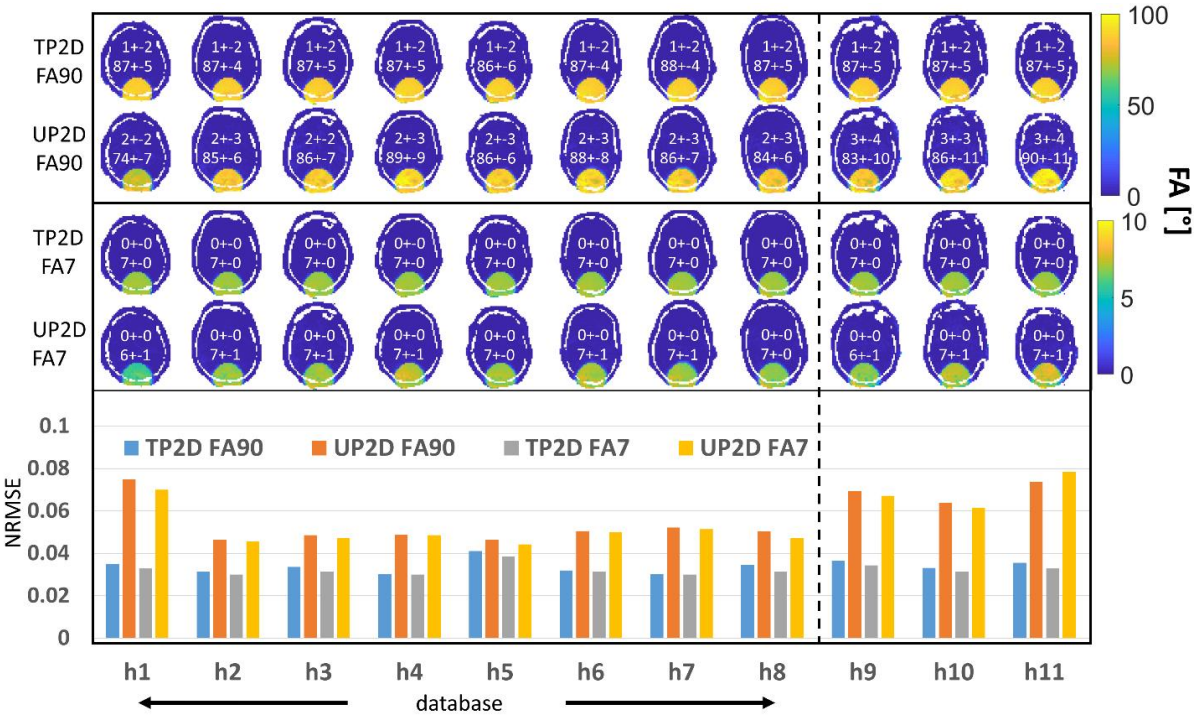

Figure 19: Bloch simulated flip angle profiles of the TPs for FA90 (first row of profiles), UP2D for FA90 (second row of profiles), the TPs for FA7 (third row), and UP2D for FA7 (fourth row). The eight columns on the left present the database heads. The three columns on the right present the non-database heads. The upper numbers within each profile depict the mean FA and the corresponding standard deviation in the non-excitation region. The lower numbers within each profile depict the mean FA and the corresponding standard deviation in the excitation region. The bar plot below the profiles illustrates the NRMSEs between the target pattern and resulting profile for each pulse and head. Reprinted from Geldschläger et al. (55) (PUBLICATION 2) with permission of John Wiley & Son, Inc.

UP3D

In simulations, both UP3D and the respective 3D TPs performances had some lack of homogeneity in the excited areas and achieved FAs below the desired FA90 or FA7. UP3D for FA90 (FA7) created a mean FA in the target excitation areas of ~70° (~6°), while the corresponding 3D TPs for FA90 (FA7) on the non-database heads only achieved a mean FA of ~49° (~4°). For non-database heads, UP3D performed with a mean NRMSE of 0.114 for FA90 and 0.115 for FA7. The mean TP performance for those heads was 0.129 for FA90 and 0.128 for FA7.

In vivo, UP3D and the respective 3D TPs performed similarly well. Both excited the visual cortex area while only very little signal of the surrounding tissues arose (Figure 20).

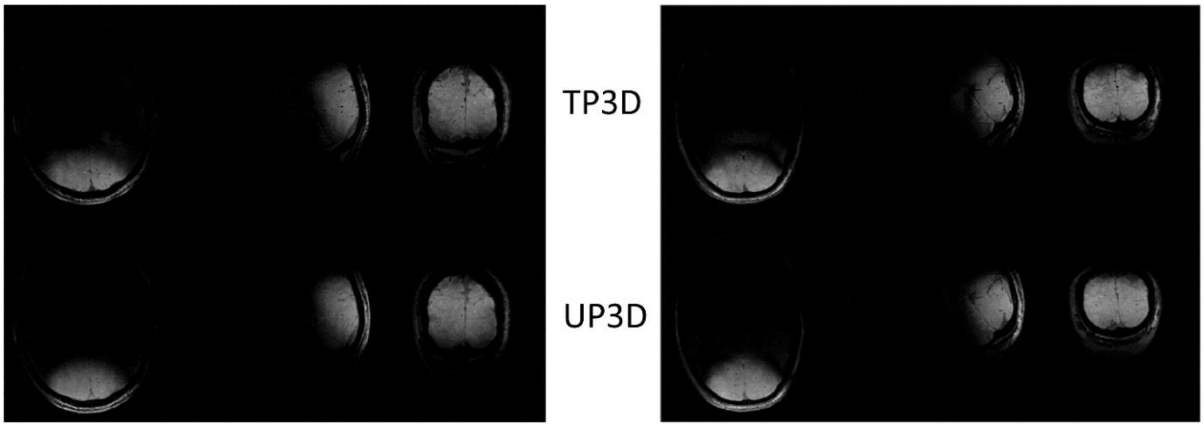

Figure 20: GRE images (one representative slice per orientation) from two non-database heads (for UP3D). The first row of images depicts images acquired with the corresponding TPs. The second row of images depicts images acquired with UP3D (FA7). Reprinted from Geldschläger et al. (55) (PUBLICATION 2) with permission of John Wiley & Son, Inc.

For the reduced FOV sequence, UP3D for FA7 was applied. As Figure 21 shows, only minor folding artifacts from outside the FOV occurred.

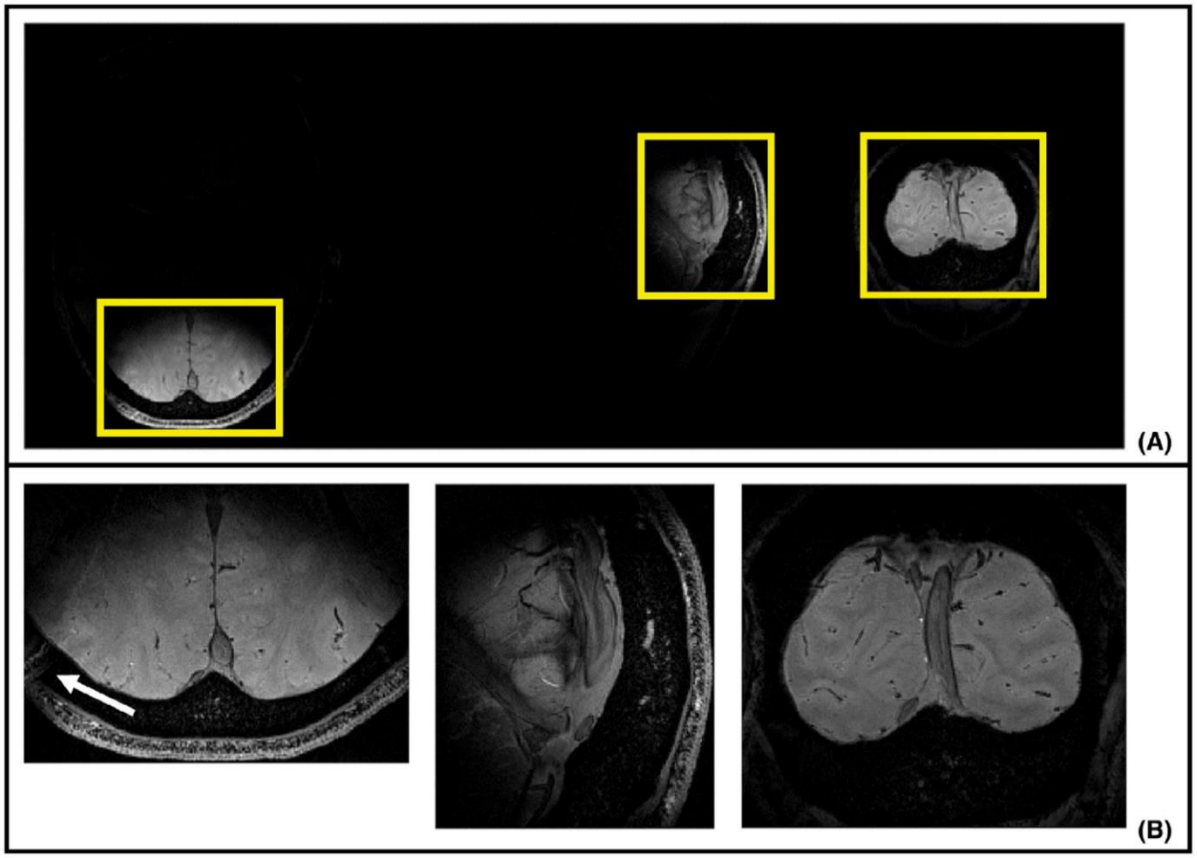

Figure 21: A: In vivo GRE images from one non-database head acquired with UP3D (FA7) with full FOV (voxel size: 0.8x0.8x0.8mm^3, matrix size: 224x280x280, scan duration (utilizing GRAPPA (56) acceleration): 9:24 min:sec). Utilizing the same voxel size as in the reduced FOV images in B and no GRAPPA, would have result in a scan duration of 75:16 min:sec. The yellow boxes in A mark the positioning of the reduced FOV applied in B. B: GRE image analog to A, but acquired with a reduced FOV (voxel size: 0.4x0.4x0.4mm^3, matrix size: 224x162x200, scan duration (without GRAPPA acceleration): 10:53 min:sec). The white arrow depicts a slight folding artifact. Reprinted from Geldschläger et al. (55) (PUBLICATION 2) with permission of John Wiley & Son, Inc.

Discussion

PUBLICATION 2 demonstrated that the concept of UPs is applicable for LEx in the human brain. For a 2D and a 3D target pattern, UPs based on eight database heads were designed. The UPs delivered a good performance in simulations and in vivo experiments at 9.4T on database heads and non-database heads for small and large FAs.

The pulses in this study were designed based on a modification of the ‘spatial domain method’. This method relies on the small tip angle approximation of the Bloch

equations. Nevertheless, it was also possible to design large FA LEx pulses (FA90) with this method.

On non-database heads, the respective 2D TPs performed slightly better compared to UP2D. Interestingly, UP3D outperformed the corresponding 3D TPs. That is most likely due to the fact that UP3D was calculated with the active-set algorithm without incorporating the excitation phase in the optimization (Eq. 10). For the TP calculation it was included (Eq. 9 from section 1.4.), as the phase cannot be excluded in the least-squares optimization (53) in the ‘spatial domain method’ (29).

Both, UP3D and corresponding 3D TPs, exhibited some deviation in terms of excitation uniformity in the excitation areas in FA profiles in simulations. However, that could be deemed acceptable as ‘most neuroimaging applications exhibit some resilience against moderate FA variations’ (57). Addressing this offset for 3D target patterns should be part of future investigations.

In general, the NRMSE values from this study were in agreement with the works on whole brain excitation using kT-points. However, these values are only partially comparable because in this study more complicated LEx pulses based on spiral trajectories were designed.

Conclusion

The UP concept for LEx pulses was demonstrated. The visual cortex region in the human brain was locally excited with UPs in vivo at 9.4T. Reduced FOV imaging was possible without significant folding artifacts from outside the FOV.

2.3. OTUP-workflow: Target specific optimization of the transmit k-space trajectory for flexible universal parallel transmit RF pulse design

This section summarizes PUBLICATION 3.

Introduction

The advantages and disadvantages of UHF and pTx were discussed in the introduction chapter of this thesis (sections 1.1. and 1.2.). As a possible solution for the lengthy calibration procedure typical for pTx, UPs were introduced.

As the literature states, for a given target excitation pattern ‘the choice of a suitable transmit k-space trajectory is crucial’ (21) for a reasonable RF pulse performance. For that reason, in the first part of PUBLICATION 3, stack-of-spiral (52,58) and SPINS (spiral nonselective (59)) trajectories were optimized for RF pTx pulse design to match the specific target excitation pattern.

In the second part of this study, UPs were designed based on the optimized transmit k-space trajectories.

The entire workflow (called OTUP) was tested on three different target excitation patterns (two LEx- , one ‘whole brain like’ homogeneous excitation target pattern). For one target the resulting RF pulses and transmit trajectories were applied in vivo at 9.4T. The OTUP workflow implementation was made available as open source (https://github.com/ole1965/workflow_OTUP.git).

Methods

Three target excitation pattern were created in order to test the OTUP workflow. The first one was ‘targetNuclei’. Herein, only a small central region encompassing the red nuclei on eight consecutive transversal slices, should experience excitation. The second test target was ‘targetM’, a ‘proof of concept’ pattern in which an area shaped like the letter ‘M’ should be excited on one central slice. The third target pattern was ‘targetWB’, a homogeneous excitation whole brain like pattern, in which all brain voxels on 16 consecutive transversal slices should be excited (i.e. there are no voxels which were not allowed to experience excitation).

All excitation areas should be excited with a desired flip angle of 7°.

For each test target excitation pattern, four different basis transmit k-space trajectories were optimized: A single variable density spiral-in trajectory (51,54) (1SOS), a two stack of variable density spiral-in trajectory (2SOS) (52,58), a three stack of variable density spiral-in trajectory (3SOS) and a spiral nonselective trajectory (SPINS) (59).

For each of the basis trajectories, the corresponding analytic equations were considered. The equation parameters of each trajectory were optimized using the 'Particle swarm optimization' (60) algorithm implemented in Matlab (MathWorks, Natick, MA). From the four optimized gradient trajectories, the one that enabled the lowest root mean squared error (RMSE) or provided another good argument (for instance considerably shorter duration with similar RMSE) was utilized for UP calculation.

For each test target pattern and optimized transmit k-space trajectory, the final UPs were calculated with a combination of the 'magnitude least squares' (61) (MLS) optimization and the active-set algorithm implemented in Matlabs *fmincon*-function (i.e. Eq. 10 from section 2.2. (PUBLICATION 2) was solved). The solution of the MLS optimization was used as initial guess for the active-set algorithm. In contrast to the design procedure from PUBLICATION 2 the MLS optimization provided an initial guess that considers only the resulting magnetization profile's magnitude in the optimization process and not the profile's phase. The least-squares optimization (53) used for initial guess creation in PUBLICATION 2 included the profile's phase and magnitude in the optimization. However, during both works, the profile's phase was of no interest.

Furthermore, in the present study within the cost function to be optimized with the active-set algorithm the flip angle profiles were simulated using the Bloch equations. In contrast, in PUBLICATION 2 the cost function to be optimized only exploited the matrix multiplication (Eq. 8 from section 1.4.) resulted from the small tip angle approximation in order to simulate the flip angle profiles.

The UP design database consisted of the B_0/B_1^+ maps from 11 different subjects. The final UPs were simulated on 7 non-database heads using Bloch-equations. The final UP for targetNuclei was applied in vivo at 9.4T for proof of principle of the UP design algorithm. The utilized sequence was a T_2^* weighted gradient-echo sequence.

For comparison, subject specific TPs were calculated for each non-database head by means of the ‘magnitude least squares’ (61) (MLS) optimization.

Results

Figure 22 shows the optimized transmit k-space trajectories for each test target. Depending on the complexity of the target the extent of the trajectories on the k_x and k_y axis differs. For the most complex pattern, targetM, the extent was the largest. For the least complex pattern, targetWB, the extent was the lowest. While all SOS trajectories were located close to the center of the k_z axis, the SPINS results for targetNuclei and targetM had a large extent on the k_z axis.

Some of the spirals of the 2SOS or 3SOS results reduced to arcs, instead of a full spiral. For targetM all trajectories enabled similar performance and exploited the maximum allowed duration of 10ms. For targetNuclei and targetWB there were differences in the RMSE performance and/or the duration visible between the four optimized trajectories, respectively.

Figure 23 depicts that for each target pattern the associated optimal transmit trajectory enabled the best performing tailored RF pulse. However, if the underlying trajectory was not designed for the target pattern, the RF pulse performance could be diminished.

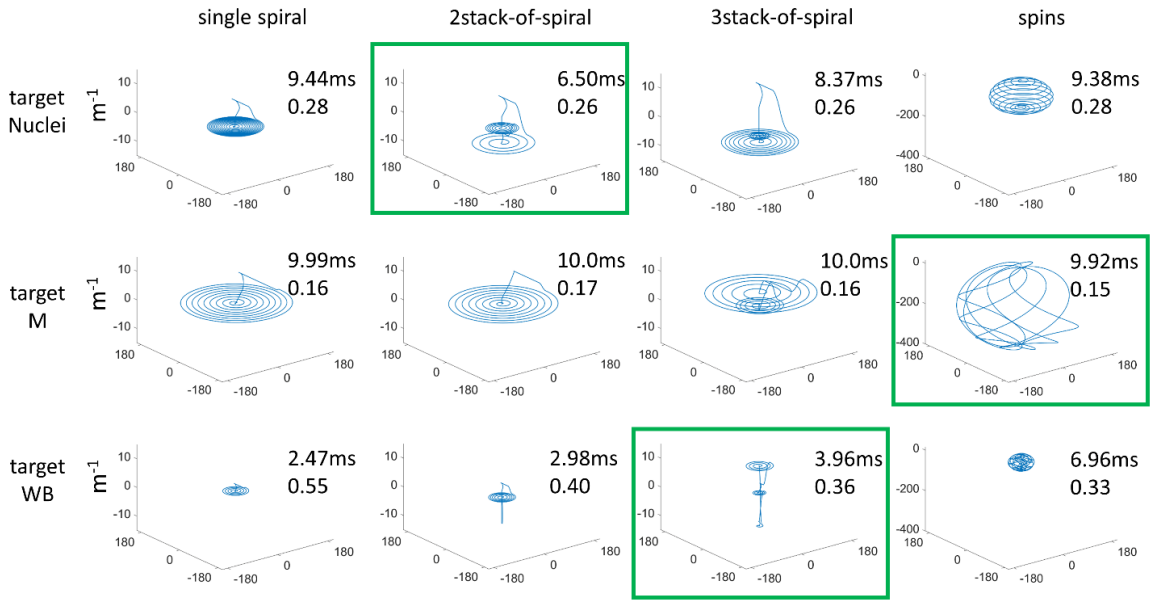

Figure 22: Optimized transmit trajectories. In each column, the same basis trajectory (1SOS, 2SOS, 3SOS or SPINS) was utilized, respectively. Each row presents the results for one of the three test target patterns, respectively. For each optimized trajectory the duration of the trajectory (in ms) and the RMSE (in degree) that the trajectories enables, is displayed. The green boxes indicate the trajectories that were chosen for UP design.

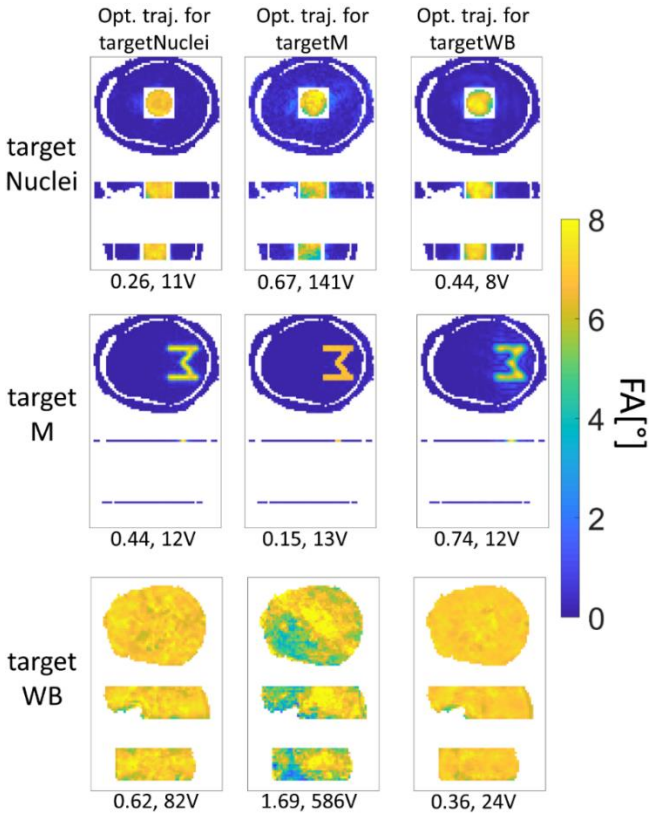

Figure 23: Bloch simulated FA profiles of RF pulses designed for different target patterns and different transmit trajectories. In the first row subject specific TPs aiming at excitation of targetNuclei were applied. Each pulse was designed based on another trajectory (depicted in the column header). In the first column, the underlying trajectory was the optimized trajectory for targetNuclei. In the second (third) column, the underlying trajectory was the optimized trajectory for targetM (targetWB). Analog, in row two and three TPs were applied aiming at excitation of targetM and target WB, respectively. Below each profile, the corresponding RMSE and the maximum amplitude of each TP is displayed.

From the three calculated UPs, the UP for targetNuclei provided the lowest difference between the mean RMSE of the TPs (0.25) and the mean RMSE performance of the UP on 7 non-database heads (0.52). The UP performance was satisfactory on all non-database heads.

The UP for targetM was not able to create the sharp transition between excitation and non-excitation voxels on all non-database subjects. The mean RMSE performance of the UP (TP) was 0.53 (0.14).

The targetWB UP was not capable of producing a similarly homogenous excitation on all non-database subjects. On certain heads, the TP and UP performance differed substantially for targetWB.

As the targetNuclei UP provided the best performance among the tested targets it was tested in vivo at 9.4T for demonstration purpose. For both subjects depicted in Figure 24, UP and TPs images appeared almost identical. The central voxels containing the nuclei were excited relatively uniform, while excitation in the surrounding tissues (in the slices of interest) was visible, but drastically lower compared to the desired excitation area. The mean excitation values and standard deviation again were highly similar.

Discussion

This work presented the OTUP workflow to optimize the underlying transmit k-space trajectory for pTx UPs and through that further improve and exploit the advantages of the UP concept.

With increasing complexity of the target excitation pattern the extent of the optimized trajectories in k_x and k_y direction in k-space increased. For targetM (i.e. the most complex target pattern exciting only the voxels along an area shaped like the letter ‘M’) very sharp transitions between excitation and non-excitation between adjacent voxels needed to be achieved. For that reason high frequencies were covered by the optimized trajectories. Only low frequencies needed to be covered for targetWB, as that was the least complex target pattern. The optimized trajectory ran close to the k-space center. For targetNuclei, where no sharp transitions between excitation and non-excitation voxels were necessary (because the voxels directly adjacent to the desired excitation voxels were masked out) the trajectories extent on the k_x and k_y axis

was between the extent of the targetM and the targetWB trajectories. Due to the differences in the frequencies covered by the respective optimized transmit k-space trajectories, unsuited trajectories can diminish the RF pulse performance and potentially lead to impractically high RF pulse voltages (Figure 23).

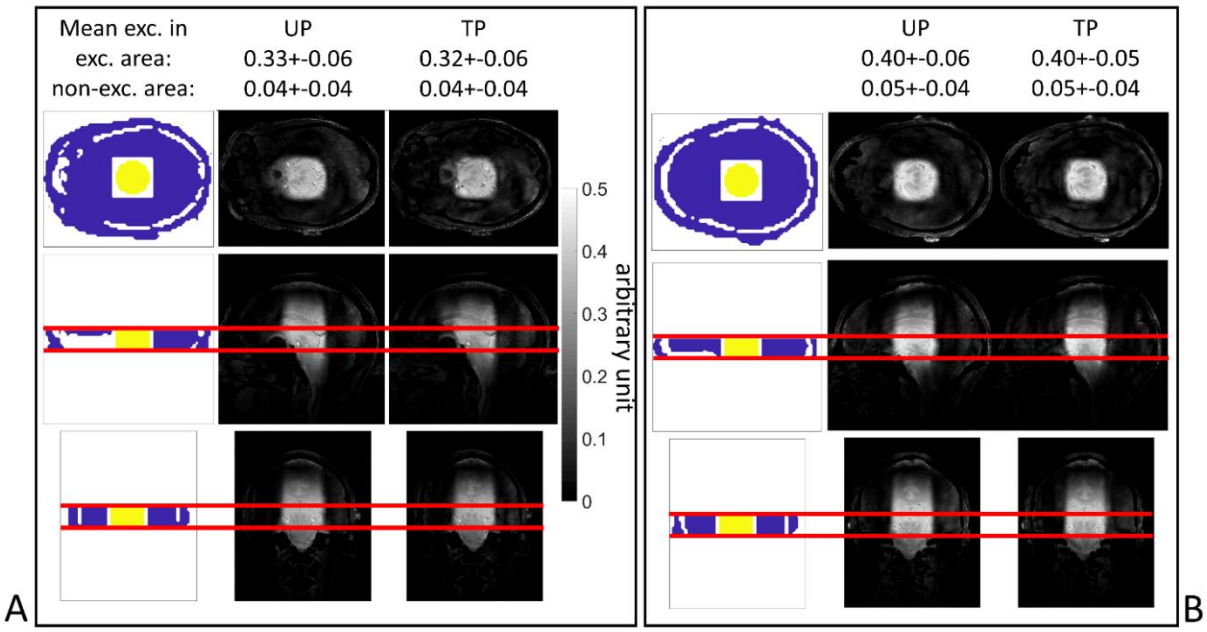

Figure 24: A and B present two different subjects. The structure is the same in both boxes. The images in the left column show the pulse design mask with the target excitation area (yellow) and non-excitation areas (blue) with a representative transversal, sagittal and coronal slice for targetNuclei. The black-white images are GRE acquisitions utilizing the UP and the respective TPs for targetNuclei on two non-database head. Only the voxels between the two red horizontal lines on the sagittal and coronal images were taken into account for the pulse design. The numbers above depict the mean signal and standard deviation in desired excitation and non-excitation regions, calculated by means of the masks on the left. The GRE images are expressed in normalized arbitrary unit, i.e. the values of each voxel was divided by the maximum signal values in the whole acquisitions.

For all test target pattern there were no transitions between excitation and non-excitation voxels along the head-to-foot direction necessary (i.e. for each target, the transversal slices were identical, respectively). For that reason, all spirals of the SOS results were located close to the center of the k_z axis. Only the SPINS trajectories for targetM and targetNuclei had a large extent on the k_z axis, because the k_x and k_y extent was large. Due to the radial extent k_{max} of a SPINS trajectory (59), these trajectories have a similar extent along all three directions in k-space, respectively.

The OTUP workflow yielded optimized transmit trajectories and TPs that produces similar or improved performances compared to the approaches in the literature

(59,58,62). Only for whole brain excitation, optimized kT-points trajectories (31) seems to have advantages in terms of the pulse duration.

The GRE acquisitions in Figure 24 demonstrated the power of the UP-concept impressively: Although the depicted subjects were non-database subjects, the UP for targetNuclei had a highly similar in vivo performance at 9.4T as the subject specific TPs.

The performance of the UP for targetWB was not satisfactory on all tested non-database heads. Especially on a head with conspicuously different head size and shape, compared to the other heads, the performance was insufficient. In order to avoid such suboptimal performances in the future, different UPs for different head sizes and shapes should be designed.

In PUBLICATION 2 UPs for LEx of the visual cortex in the human brain, based on non-optimized transmit trajectories (duration: 8.18ms), were presented. These UPs performed with a mean NRMSE of 11.4% on non-database heads. This visual cortex target from PUBLICATION 2 is comparable to targetNuclei from PUBLICATION 3. With optimized transmit trajectories it was possible to outperform the UPs from PUBLICATION 2, as in PUBLICATION 3 a mean UP NRMSE (RMSE divided by 7) for targetNuclei of 7.4% and a pulse duration of 6.5ms was achieved.

Conclusion

The OTUP workflow to optimize the transmit k-space trajectory (SOS and SPINS) and to calculate UPs and subject specific TPs based on the trajectory was presented. The workflow was demonstrated for three different target excitation patterns. The importance of utilizing an optimized transmit k-space trajectory that matches the target excitation pattern was emphasized.

TPs and UPs produced highly similar GRE images in vivo at 9.4T, proofing the power of the UP concept.

The workflow code and the B_0/B_1^+ map data from 18 subjects measured at 9.4T are available online as open source.

3. Conclusion and Outlook

The strength of the main magnetic (B_0) field is crucial to obtain ultrahigh resolution magnetic resonance images from the human body. The first part of this thesis exploited the advantages of the ultrahigh B_0 field strength of 9.4T for spinal cord imaging. While numerous studies showed the improvements in the image quality and diagnostic power for imaging the spinal cord at 7T compared to 1.5T or 3T, this thesis presented the first spinal cord MR images at 9.4T. The ultrahigh resolution images (in-plane resolution of 0.15x0.15mm^2) were acquired with a brain coil. T_2^* relaxation times of gray and white matter in the human SC at 9.4T were calculated. The work performed the first step into spinal cord research at a field strength higher than 7T and might open new possibilities in clinical patient care in the future. Knowing the T_2^* times allows optimization of imaging parameters and potentially enables improvements in sensitivity and contrast.

The second part of this thesis investigated with parallel transmission, a powerful technique to address the UHF inherent issue of inhomogeneous RF transmit sensitivities. In order to circumvent the lengthy calibration procedure typical for parallel transmission applications, the ‘universal parallel transmit pulses’ were introduced. After the literature provided several examples of universal pulses for whole brain or slice selective excitation, in this thesis a ‘proof of concept’ study was performed, that showed the feasibility of universal pulses for a local excitation application. It was possible to design universal pulses that excited the visual cortex region locally on non-database heads.

Furthermore, this thesis proposed an universal pulse design workflow that optimized the underlying transmit k-space trajectory to match the excitation target in the best possible way, before the actual universal pulse design started. Notably, in contrast to the literature, where universal pulse design was performed based on ‘kT-points’ or ‘spokes’ trajectories, in this thesis the transmit k-space trajectory optimized were ‘spirals’ and ‘SPINS’ trajectories. The entire workflow was applied for different excitation targets, including local excitation targets and whole brain excitation. Designing universal pulses based on optimized transmit k-space trajectories improved the pulse performance compared to the

performance of universal pulses based on non-optimized trajectories. The entire trajectory optimization and UP design code was provided as ‘open source’ software to the community.

This thesis extended the general concept of universal pulses. Providing these pulses, not only for whole brain, but also for local excitation applications, prospectively abandons the need for time-consuming subject specific B_1^+ and B_0 calibration measurements and parallel transmission-pulse calculation during the scan session. Thus, with this thesis the next step towards utilizing parallel transmission-techniques more widely in the clinics was done.

As a possible next goal in the future, the universal pulse concept may be utilized for applications in other body parts as the head. As an example, universal pulse design could be tested for local excitation of the human spinal cord. However, this problem seems to be more challenging as universal pulses for the head, due to higher inter-subject variability in human necks compared to heads. Further, the increased main magnetic field inhomogeneity in the neck compared to the head, may make the pulse optimization more difficult.

4. References

1. Haacke E, Brown R, Thompson M, Venkatesan R. Magnetic Resonance Imaging: Physical Principles and Sequence Design: John Wiley & Sons, Inc.; 1999.

2. Levitt MH. Spin Dynamics: Basics of Nuclear Magnetic Resonance, 2nd Edition: John Wiley & Sons, Ltd.; 2008.

3. The NIST Reference on Constants, Units, and Uncertainty. [Online]. [cited 2021 September 19. Available from: https://physics.nist.gov/cgi-bin/cuu/Value?gammapbar.

4. Weishaupt D, Köchli V, Marincek B. How does MRI work?: An Introduction to the Physics and Function of Magnetic Resonance : Springer; 2006.

5. Hoult DI, Richards RE. The signal-to-noise ratio of the nuclear magnetic resonance experiment. Journal of Magnetic Resonance (1969). 1976 Oct; 24: 71–85.

6. Pohmann R, Speck O, Scheffler K. Signal-to-noise ratio and MR tissue parameters in human brain imaging at 3, 7, and 9.4 tesla using current receive coil arrays. Magnetic Resonance in Medicine. 2015 Mar; 75: 801–809.

7. Pfrommer A, Henning A. The ultimate intrinsic signal-to-noise ratio of loop- and dipole-like current patterns in a realistic human head model. Magnetic Resonance in Medicine. 2018 Mar; 80: 2122–2138.

8. Hendrick ER. Breast MRI: Fundamentals and Technical Aspects New York: Springer Science and Business Media; 2008.

9. Springer E, Dymerska B, Cardoso PL, Robinson SD, Weisstanner C, Wiest R, et al. Comparison of Routine Brain Imaging at 3 T and 7 T. Investigative Radiology. 2016 Aug; 51: 469–482.

10. Sigmund EE, Suero GA, Hu C, McGorty K, Sodickson DK, Wiggins GC, et al. High-resolution human cervical spinal cord imaging at 7

11. Dula AN, Pawate S, Dortch RD, Barry RL, George-Durrett KM, Lyttle BD, et al. Magnetic resonance imaging of the cervical spinal cord in multiple sclerosis at 7T. Multiple Sclerosis Journal. 2015 Jul; 22: 320–328.

12. Zhao W, Cohen-Adad J, Polimeni JR, Keil B, Guerin B, Setsompop K, et al. Nineteen-channel receive array and four-channel transmit array coil for cervical spinal cord imaging at 7T. Magnetic Resonance in Medicine. 2013 Aug; 72: 291–300.

13. Sclocco R, Beissner F, Bianciardi M, Polimeni JR, Napadow V. Challenges and opportunities for brainstem neuroimaging with ultrahigh field MRI. NeuroImage. 2018 Mar; 168: 412–426.

14. Padormo F, Beqiri A, Hajnal JV, Malik SJ. Parallel transmission for ultrahigh-field imaging. NMR in Biomedicine. 2015 May; 29: 1145–1161.

15. Röschmann P. Radiofrequency penetration and absorption in the human body: Limitations to high-field whole-body nuclear magnetic resonance imaging. Medical Physics. 1987 Nov; 14: 922–931.

16. Ibrahim TS, Lee R, Abduljalil AM, Baertlein BA, Robitaille PML. Dielectric resonances and B 1 field inhomogeneity in UHFMRI: computational analysis and experimental findings. Magnetic Resonance Imaging. 2001 Feb; 19: 219–226.

17. Gras V, Mauconduit F, Vignaud A, Amadon A, Bihan DL, Stöcker T, et al. Design of universal parallel-transmit refocusing kT -point pulses and application to 3D T2 -weighted imaging at 7T. Magnetic Resonance in Medicine. 2017 Nov; 80: 53–65.

18. Katscher U, Börnert P, Leussler C, van den Brink JS. Transmit SENSE. Magnetic Resonance in Medicine. 2002 Dec; 49: 144–150.

19. Zhu Y. Parallel excitation with an array of transmit coils. Magnetic Resonance in Medicine. 2004; 51: 775–784.

20. Poser BA, Anderson RJ, Guérin B, Setsompop K, Deng W, Mareyam A, et al. Simultaneous multislice excitation by parallel transmission. Magnetic Resonance in Medicine. 2013 May; 71: 1416–1427.

21. Schneider JT, Kalayciyan R, Haas M, Herrmann SR, Ruhm W, Hennig J, et al. Inner-volume imaging in vivo using three-dimensional parallel spatially selective excitation. Magnetic Resonance in Medicine. 2012 Jun; 69: 1367–1378.

22. Stadler A, Schima W, Ba-Ssalamah A, Kettenbach J, Eisenhuber E. Artifacts in body MR imaging: their appearance and how to eliminate them. European Radiology. 2006 Dec; 17: 1242–1255.

23. Schneider J, Haas M, Hennig J, Junge S, Ruhm W, Ullmann P. Enhanced Image Resolution and Reduced Measurement Time Using Inner Volume Imaging and Parallel Excitation. In Proceedings of the International Society for Magnetic Resonance in Medicine Meeting 2009 (Honolulu).

24. Malik SJ, Hajnal JV. Phase relaxed localized excitation pulses for inner volume fast spin echo imaging. Magnetic Resonance in Medicine. 2015 Oct; 76: 848–861.

25. Rosenkrantz AB, Chandarana H, Pfeuffer J, Triolo MJ, Shaikh MB, Mossa DJ, et al. Zoomed echo-planar imaging using parallel transmission: impact on image quality of diffusion-weighted imaging of the prostate at 3T. Abdominal Imaging. 2014 Jun; 40: 120–126.

26. Thierfelder KM, Sommer WH, Dietrich O, Meinel FG, Theisen D, Paprottka PM, et al. Parallel-transmit-accelerated spatially-selective excitation mri for reduced-fov diffusion-weighted-imaging of the pancreas. European Journal of Radiology. 2014 Oct; 83: 1709–1714.

27. Plewes DB, Kucharczyk W. Physics of MRI: A primer. Journal of Magnetic Resonance Imaging. 2012 Apr; 35: 1038–1054.

28. Pauly J, Nishimura D, Macovski A. A k-space analysis of small-tip-angle excitation. Journal of Magnetic Resonance. 1989 Jan; 81: 43–56.

29. Grissom W, Yip Cy, Zhang Z, Stenger VA, Fessler JA, Noll DC. Spatial domain method for the design of RF pulses in multicoil parallel excitation. Magnetic Resonance in Medicine. 2006; 56: 620–629.

30. Deniz CM. Parallel Transmission for Ultrahigh Field MRI. Topics in Magnetic Resonance Imaging. 2019 Jun; 28: 159–171.

31. Gras V, Vignaud A, Amadon A, Bihan DL, Boulant N. Universal pulses: A new concept for calibration-free parallel transmission. Magnetic Resonance in Medicine. 2016 Feb; 77: 635–643.

32. Gras V, Pracht ED, Mauconduit F, Bihan DL, Stöcker T, Boulant N. Robust nonadiabatic T2 preparation using universal parallel-transmit kT -point pulses for 3D FLAIR imaging at 7 T. Magnetic Resonance in Medicine. 2019 Jan; 81: 3202–3208.

33. Gras V, Boland M, Vignaud A, Ferrand G, Amadon A, Mauconduit F, et al. Homogeneous non-selective and slice-selective parallel-transmit excitations at 7 Tesla with universal pulses: A validation study on two commercial RF coils. PLOS ONE. 2017 Aug; 12: e0183562.

34. Gras V, Vignaud A, Rabrait-Lerman C, Le Bihan D, Stoecker T, Stirnberg R, et al. Gain of temporal signal-to-noise ratio with pTx universal pulses and the whole-brain fMRI 3D-GE EPI sequence at 7T. In Proceedings of the International Society for Magnetic Resonance in Medicine Meeting 2018 (Paris), 5440.

35. Ciccarelli O, Werring DJ, Barker GJ, Griffin CM, Wheeler-Kingshott CAM, Miller DH, et al. A study of the mechanisms of normal-appearing white matter damage in multiple sclerosis using diffusion tensor imaging. Journal of Neurology. 2003 Mar; 250: 287–292.

36. Ciccarelli O, Wheeler-Kingshott CA, McLean MA, Cercignani M, Wimpey K, Miller DH, et al. Spinal cord spectroscopy and diffusion-based tractography to assess acute disability in multiple sclerosis. Brain. 2007 Aug; 130: 2220–2231.

37. Sach M. Diffusion tensor MRI of early upper motor neuron involvement in amyotrophic lateral sclerosis. Brain. 2004 Feb; 127: 340–350.

38. Demir A, Ries M, Moonen CTW, Vital JM, Dehais J, Arne P, et al. Diffusion-weighted MR Imaging with Apparent Diffusion Coefficient and Apparent Diffusion Tensor Maps in Cervical Spondylotic Myelopathy. Radiology. 2003 Oct; 229: 37–43.

39. Barry RL, Vannesjo SJ, By S, Gore JC, Smith SA. Spinal cord MRI at 7T. NeuroImage. 2018 Mar; 168: 437–451.

40. Massire A, Taso M, Besson P, Guye M, Ranjeva JP, Callot V. High-resolution multi-parametric quantitative magnetic resonance imaging of the human cervical spinal cord at 7T. NeuroImage. 2016 Dec; 143: 58–69.

41. Massire A, Rasoanandrianina H, Guye M, Callot V. Anterior fissure, central canal, posterior septum and more: New insights into the cervical spinal cord gray and white matter regional organization using T1 mapping at 7T. NeuroImage. 2020 Jan; 205: 116275.

42. Avdievich NI, Giapitzakis IA, Pfrommer A, Borbath T, Henning A. Combination of surface and `vertical' loop elements improves receive performance of a human head transceiver array at 9.4 T. NMR in Biomedicine. 2017 Dec; 31: e3878.

43. Cooke FJ, Blamire AM, Manners DN, Styles P, Rajagopalan B. Quantitative proton magnetic resonance spectroscopy of the cervical spinal cord. Magnetic Resonance in Medicine. 2004; 51: 1122–1128.

44. Gruetter R, Tkác I. Field mapping without reference scan using asymmetric echo-planar techniques. Magnetic Resonance in Medicine. 2000 Feb; 43: 319–323.

45. Nassirpour S, Chang P, Fillmer A, Henning A. A comparison of optimization algorithms for localized in vivo B0 shimming. Magnetic Resonance in Medicine. 2017 May; 79: 1145–1156.

46. Roemer PB, Edelstein WA, Hayes CE, Souza SP, Mueller OM. The NMR phased array. Magnetic Resonance in Medicine. 1990 Nov; 16: 192–225.

47. Held P, Dorenbeck U, Seitz J, Fründ R, Albrich H. MRI of the abnormal cervical spinal cord using 2D spoiled gradient echo multiecho sequence (MEDIC) with magnetization transfer saturation pulse: A T2* weighted feasibility study. Journal of Neuroradiology. 2003; 30: 83-90.

48. Geldschläger O, Bosch D, Avdievich NI, Henning A. Ultrahigh-resolution quantitative spinal cord MRI at 9.4T. Magnetic Resonance in Medicine. 2020 Aug; 85: 1013–1027.

49. Zelinski AC, Wald LL, Setsompop K, Goyal VK, Adalsteinsson E. Sparsity-Enforced Slice-Selective MRI RF Excitation Pulse Design. IEEE Transactions on Medical Imaging. 2008 Sep; 27: 1213–1229.

50. Cloos MA, Boulant N, Luong M, Ferrand G, Giacomini E, Bihan DL, et al. kT-points: Short three-dimensional tailored RF pulses for flip-angle homogenization over an extended volume. Magnetic Resonance in Medicine. 2011 May; 67: 72–80.

51. Kim Dh, Adalsteinsson E, Spielman DM. Simple analytic variable density spiral design. Magnetic Resonance in Medicine. 2003 Jun; 50: 214–219.

52. Irarrazabal P, Nishimura DG. Fast Three Dimensional Magnetic Resonance Imaging. Magnetic Resonance in Medicine. 1995 May; 33: 656–662.

53. Paige CC, Saunders MA. LSQR: An Algorithm for Sparse Linear Equations and Sparse Least Squares. ACM Transactions on Mathematical Software. 1982 Mar; 8: 43–71.

54. Schröder C, Börnert P, Aldefeld B. Spatial excitation using variable-density spiral trajectories. Journal of Magnetic Resonance Imaging. 2003 Jun; 18: 136–141.

55. Geldschläger O, Bosch D, Glaser S, Henning A. Local excitation universal parallel transmit pulses at 9.4T. Magnetic Resonance in Medicine. 2021 Jun.

56. Griswold MA, Jakob PM, Heidemann RM, Nittka M, Jellus V, Wang J, et al. Generalized autocalibrating partially parallel acquisitions (GRAPPA). Magnetic Resonance in Medicine. 2002 Jun; 47: 1202–1210.

57. Wiggins C, Poser B, Mauconduit F, Boulant N, Gras V. Universal Pulses for MRI at 9.4 Tesla - a Feasibility Study. In 2019 International Conference on Electromagnetics in Advanced Applications (ICEAA); 2019 Sep: IEEE.

58. Shao T, Xia L, Tao G, Chi J, Liu F, Crozier S. Advanced Three-Dimensional Tailored RF Pulse Design in Volume Selective Parallel Excitation. IEEE Transactions on Medical Imaging. 2012 May; 31: 997–1007.

59. Malik SJ, Keihaninejad S, Hammers A, Hajnal JV. Tailored excitation in 3D with spiral nonselective (SPINS) RF pulses. Magnetic Resonance in Medicine. 2011 Aug; 67: 1303–1315.

60. Kennedy J, Eberhart R. Particle swarm optimization. In Proceedings of IEEE - International Conference on Neural Networks. Perth, Australia, 1995, pp. 1942-1945.

61. Setsompop K, Wald LL, Alagappan V, Gagoski BA, Adalsteinsson E. Magnitude least squares optimization for parallel radio frequency excitation design demonstrated at 7 Tesla with eight channels. Magnetic Resonance in Medicine. 2008; 59: 908–915.

62. Davids M, Schad LR, Wald LL, Guérin B. Fast three-dimensional inner volume excitations using parallel transmission and optimized k-space trajectories. Magnetic Resonance in Medicine. 2015 Nov; 76: 1170–1182.

5. Publication List

First-author articles, on which the thesis is based:

1. Geldschläger O, Bosch D, Avdievich NI, Henning A. Ultrahigh-resolution quantitative spinal cord MRI at 9.4T. Magnetic Resonance in Medicine. 2020 Aug; 85: 1013–1027.
   DOI: 10.1002/mrm.28455
2. Geldschläger O*, Bosch D*, Glaser S, Henning A. Local excitation universal parallel transmit pulses at 9.4T. Magnetic Resonance in Medicine. 2021 Jun.
   DOI: 10.1002/mrm.28905
3. Geldschläger O, Bosch D, Henning, A. OTUP-workflow: Target specific optimization of the transmit k-space trajectory for flexible universal parallel transmit RF pulse design (submitted to Magnetic Resonance in Medicine, under review).

* shared first-authorship

First-author conference proceedings, which resulted in an oral presentation

4. Geldschläger O, Manohar SM, Wright A, Avdievitch N, Henning A. First MRI of the human spinal cord at 9.4T. In Proceedings of the International Society for Magnetic Resonance in Medicine Ultrahigh Field Magnetic Resonance Meeting 2019 (Dubrovnik), p. 75.
5. Geldschläger O, Bosch D, Avdievitch NI, Scheffler K, Henning A. Spinal Cord Segmentation and T_2^*-relaxation times of GM and WM within the Spinal Cord at 9.4T. In Proceedings of the International Society for Magnetic Resonance in Medicine Meeting 2020 (Virtual conference), p. 1172.

First-author conference proceedings, which resulted in a poster presentation

6. Geldschläger O, Shao T, Henning A. Universal parallel transmit pulse design for local excitation. In Proceedings of the International Society for Magnetic Resonance in Medicine Meeting 2018 (Paris), p. 3395.

7. Geldschläger O, Shao T, Henning A. Universal parallel transmit pulse design for 3-dimensional local-excitation – a 9.4T simulation study. In Proceedings of the International Society for Magnetic Resonance in Medicine Ultrahigh Field Magnetic Resonance Meeting 2019 (Dubrovnik), p. 8.
8. Geldschläger O, Shao T, Henning A. Universal parallel transmit pulse design for 3-dimensional local-excitation – a 9.4T simulation study. In Proceedings of the International Society for Magnetic Resonance in Medicine 2019 Meeting (Montreal), p. 4639.
9. Geldschläger O, Manohar SM, Wright A, Avdievitch N, Henning A. First MRI of the human spinal cord at 9.4T. In Proceedings of the International Society for Magnetic Resonance in Medicine 2019 Meeting (Montreal), p. 1585.
10. Geldschläger O, Herrler J, Nagel A, Henning A. Universal parallel transmit pulse design for 3-D local-excitation based on different sized databases of B_0/B_1^+-maps - a 7T study. In Proceedings of the International Society for Magnetic Resonance in Medicine Meeting 2020 (Virtual conference), p. 3699.
11. Geldschläger O, Bosch D, Henning A. Universal parallel transmit pulses for a 2-dimensional local excitation pattern at 9.4T. In Proceedings of the International Society for Magnetic Resonance in Medicine Meeting 2021 (Virtual conference), p. 3963.

Other contributions to conference proceedings

12. Bosch D, Geldschläger O, Avdievitch NI, Schuppert M, Henning A, Scheffler K. Influence of TX coil impedance mismatch on parallel transmission applications at 9.4T. In Proceedings of the International Society for Magnetic Resonance in Medicine Ultrahigh Field Magnetic Resonance Meeting 2019 (Dubrovnik), p. 57.

6. Statement of Contributions

PUBLICATION 1

Geldschläger O, Bosch D, Avdievich NI, Henning A. Ultrahigh-resolution quantitative spinal cord MRI at 9.4T. Magnetic Resonance in Medicine. 2020 Aug; 85: 1013–1027.

O. Geldschläger	He had the idea to image the human spinal cord at 9.4T, especially doing ultrahigh resolution imaging. Furthermore, he created the approach to utilize a brain coil for spinal cord imaging. Compared different echo times, calculated T_2^* maps and performed the algorithm segmentation. Performed the measurements. Wrote the manuscript.
D. Bosch	He provided the idea and the theory to calculate the T_2^* maps. Assisted during every scan session. Gave advice on the general content of the work. Proofread the manuscript.
NI. Avdievich	He built the coil. Provided the k-factor parameter to satisfy the safety regulations.
A. Henning	She was the project supervisor and gave advice on the manuscript.

PUBLICATION 2

Geldschläger O*, Bosch D*, Glaser S, Henning A. Local excitation universal parallel transmit pulses at 9.4T. Magnetic Resonance in Medicine. 2021 Jun.

O. Geldschläger*	He had the idea to design universal pulses for local excitation. Developed and implemented the universal pulse design method. Calculated all the pulses. Performed the measurements. Wrote the majority of the manuscript.
D. Bosch*	He created the masking routine. Wrote and implemented all MR sequences and the general workflow at the scanner. Assisted

during every scan session. Co-developed the structure of the manuscript and partially wrote it.

S. Glaser — He provided parts of the code, on which the tailored pulse calculations were based on.

A. Henning — She was the project supervisor and gave advice on the manuscript.

* shared first-authorship

PUBLICATION 3

Geldschläger O, Bosch D, Henning A. OTUP-workflow: Target specific optimization of the transmit k-space trajectory for flexible universal parallel transmit RF pulse design (submitted to Magnetic Resonance in Medicine).

O. Geldschläger — He had the idea of the entire workflow: optimized the transmit trajectories, created the test target patterns. Implemented the workflow. Calculated every trajectory and RF pulse. Performed the measurements. Wrote the manuscript.

D. Bosch — He provided the masking routine. Wrote and implemented all MR sequences and the general workflow at the scanner. Assisted during every scan session. Gave advice on the general content of the work and the manuscript.

A. Henning — She was the project supervisor and gave advice on the manuscript.

7. Appended Publications

The following scientific articles are appended:

PUBLICATION 1: Geldschläger O, Bosch D, Avdievich NI, Henning A. Ultrahigh-resolution quantitative spinal cord MRI at 9.4T. Magnetic Resonance in Medicine. 2020 Aug; 85: 1013–1027.

DOI: 10.1002/mrm.28455

PUBLICATION 2: Geldschläger O*, Bosch D*, Glaser S, Henning A. Local excitation universal parallel transmit pulses at 9.4T. Magnetic Resonance in Medicine. 2021 Jun.

DOI: 10.1002/mrm.28905

PUBLICATION 3: Geldschläger O, Bosch D, Henning, A. OTUP-workflow: Target specific optimization of the transmit k-space trajectory for flexible universal parallel transmit RF pulse design (submitted to Magnetic Resonance in Medicine, under review).

* shared first-authorship

PUBLICATION 1

Ultrahigh-resolution quantitative spinal cord MRI at 9.4T.

Geldschläger O, Bosch D, Avdievich NI, Henning A.

Magnetic Resonance in Medicine. 2020 Aug; 85: 1013–1027.

DOI: 10.1002/mrm.28455

Received: 5 March 2020 | Revised: 6 July 2020 | Accepted: 10 July 2020

DOI: 10.1002/mrm.28455

FULL PAPER

Magnetic Resonance in Medicine

Ultrahigh-resolution quantitative spinal cord MRI at 9.4T

Ole Geldschläger[1] | **Dario Bosch**[1,2] | **Nikolai I. Avdievich**[1] | **Anke Henning**[1,3]

[1]High-Field Magnetic Resonance Center, Max Planck Institute for Biological Cybernetics, Tübingen, Germany

[2]Biomedical Magnetic Resonance, University Hospital Tübingen, Tübingen, Germany

[3]Advanced Imaging Research Center, University of Texas Southwestern Medical Center, Dallas, Texas, USA

Correspondence
Ole Geldschläger, High-Field Magnetic Resonance Center, Max Planck Institute for Biological Cybernetics, Max-Planck-Ring 11, 72076 Tübingen, Germany.
Email: ole.geldschlaeger@tuebingen.mpg.de

Funding information
This project was co-sponsored by the European Research Council/SYNAPLAST MR/Grant number: 679927 and the Cancer Prevention and Research Institute of Texas (CPRIT)/Grant number: RR180056

Purpose: To present the results of the first human spinal cord in vivo MRI scans at 9.4T.

Methods: A human brain coil was used to image the human spinal cord at 9.4T. All anatomical images were acquired with a T_2*-weighted gradient-echo sequence. A comparison of the influence of four different B_0 shimming routines on the image quality was performed. Intrinsic signal-to-noise-ratio maps were determined using a pseudo-multiple replica approach. Measurements with different echo times were compared and processed to one multiecho data image combination image. Based on the multiecho acquisitions, T_2*-relaxation time maps were calculated. Algorithmic spinal cord detection and gray matter/white matter segmentation were tested.

Results: An echo time between 9 and 13.8 ms compromised best between gray matter/white matter contrast and image quality. A maximum in-plane resolution of 0.15×0.15 mm^2 was achieved for anatomical images. These images offered excellent image quality and made small structures of the spinal cord visible. The scanner vendor implemented B_0 shimming routine performed best during this work. Intrinsic signal-to-noise-ratio values of between 6600 and 8060 at the upper cervical spinal cord were achieved. Detection and segmentation worked reliably. An average T_2*-time of 24.88 ms $\pm$ 6.68 ms for gray matter and 19.37 ms $\pm$ 8.66 ms for white matter was calculated.

Conclusion: The proposed human brain coil can be used to image the spinal cord. The maximum in-plane resolution in this work was higher compared with the 7T results from the literature. The 9.4T acquisitions made the small structures of the spinal cord clearly visible.

KEYWORDS

9.4 Tesla, high-field magnetic resonance imaging, relaxometry mapping, segmentation, spinal cord magnetic resonance imaging

1 | INTRODUCTION

Today MRI is an indispensable method for clinical diagnostic and research investigations of the human spinal cord (SC). For SC-related diseases such as multiple sclerosis,[1-3] amyotrophic lateral sclerosis,[4] spondylosis,[5] or SC injury[6] MRI is the technique of choice for primary diagnostics, patient stratification, and therapy monitoring. Furthermore, it has been reported that in patients with multiple sclerosis, gray matter (GM) lesions in the SC may be detectable more readily than GM lesions in the brain, which illustrates the importance of SC imaging investigations in general.[7]

Small structures within the SC are inherently challenging to image at lower B_0 field strengths; hence, field strength is of important relevance for SC measurements. Utilizing higher field strengths provides a higher signal-to-noise-ratio (SNR), facilitates higher spatial resolutions, and potentially improves diagnostic power. For example, it has been shown that the detection of small lesions in patients with multiple sclerosis at 3T MRI is improved versus 1.5T MRI.[8,9] Sigmund et al[10] and Zhao et al[11] have published comparisons of anatomical SC images, which display excellent improvement of the image quality at 7T versus 3T. Additionally, it has been shown that in patients with multiple sclerosis, on average 4.7 white matter (WM) lesions can be detected at 7T in the SC, whereas at 3T only 3.1 WM lesions can be found. This increase of 52% emphasizes the advantages of higher field strengths for SC MRI.[12]

Barry et al[13] gave an excellent review on the current state of "Spinal Cord MRI at 7T" included also the advantages of ultrahigh-field strength for different imaging modalities beyond anatomical MRI. To take it a step further, this study presents in vivo MR measurements of the SC at a field strength of 9.4T, which could theoretically offer about twice the SNR compared with MRI at 7T with similar radiofrequency (RF) coils and sequences.[14,15] To our knowledge, with the exception of our own preliminary work published in a conference abstract,[16] these are the first human in vivo SC MRI results obtained at this field strength. Previous work at 9.4T has focused on human postmortem samples,[17] injured SC in squirrel monkeys,[18,19] and SC in mice[20] and rats.[21]

A comprehensive overview on 7T SC coils[13] demonstrated that the majority of these designs had only posterior elements on a holder adapted to the neck and utilized only surface-loop receive elements.[10,11,12] In this work, a new approach to SC RF coil design is introduced that combines transceiver surface-loop elements with additional receive-only vertical loops and contains anterior as well as posterior coverage to increase the central SNR. This coil design[22] was originally suggested for improved central SNR in human brain scans. The increase in central SNR is also beneficial for imaging the cervical SC because of its central position in the head and neck.

Anatomical images of the cervical SC were measured with a T_2*-weighted GRadient-Echo (GRE) sequence.[23] To address the SC MRI inherent issue of periodic B_0 inhomogeneities caused by the intervertebral discs,[24,25] the literature provides solutions as "electrocardiogram-triggered, higher order, projection-based B_0 shimming"[26] or z-shim gradient pulses.[25] To minimize the influence of these B_0 inhomogeneities, four different B_0 shimming routines were tested and compared during this work. Intrinsic SNR maps were calculated and the impact of different echo times (TEs) on image quality and contrast was investigated to find optimal sequence parameters.

Recently, anatomical SC images with an in-plane resolution of 0.18×0.18 mm^2 have been published,[10,27] which is the highest resolution of in vivo human SC measurement in the literature. In this study, the resolution could be further improved and anatomical images with an in-plane resolution of 0.15×0.15 mm^2 are presented.

Additionally, algorithmic SC detection and GM/WM segmentation was performed, as well as calculation of T_2*-relaxation-time maps of the human SC at 9.4T.

2 | METHODS

2.1 | Radiofrequency coil

All measurements in this study were performed with an in-house-built 16-channel tight-fit array coil.[22] This array consists of eight transceiver surface loops and eight receive-only loops. The eight transceiver surface loops are placed on a cylindrical holder. Each of the eight vertical receive-only loops is positioned along the central axis of a transceiver loop, perpendicular to its surface. Figure 1A consists of a photograph of the coil and some of the transceiver and receive-only loops.

This coil was originally constructed for human brain scans with an emphasis to enhance the SNR in deep brain structures and high-transmission efficiency. The addition of the vertical loops has no measurable effect on the Tx efficiency of the array. However, the 16-channel set-up provides an improvement of the SNR in vivo of approximately 30% in the center of the brain, compared with the surface-loops-only set-up.

The central SNR improvement was the motivation for testing the coil for SC data acquisition. The coil array and its housing geometry is cylindrical, with openings at top and bottom. This geometry makes it possible to place the subject further inside the coil than originally intended and allow the cervical SC to be imaged. Figure 1B depicts the subject positioning for brain scans versus that for SC scans. For brain scans, the subject's brain is placed in the center of the loop array; however, for cervical SC measurements in this study each subject was positioned further into the coil until the shoulders contacted the coil housing. In that position, the upper cervical SC is located in the center of the loop array.

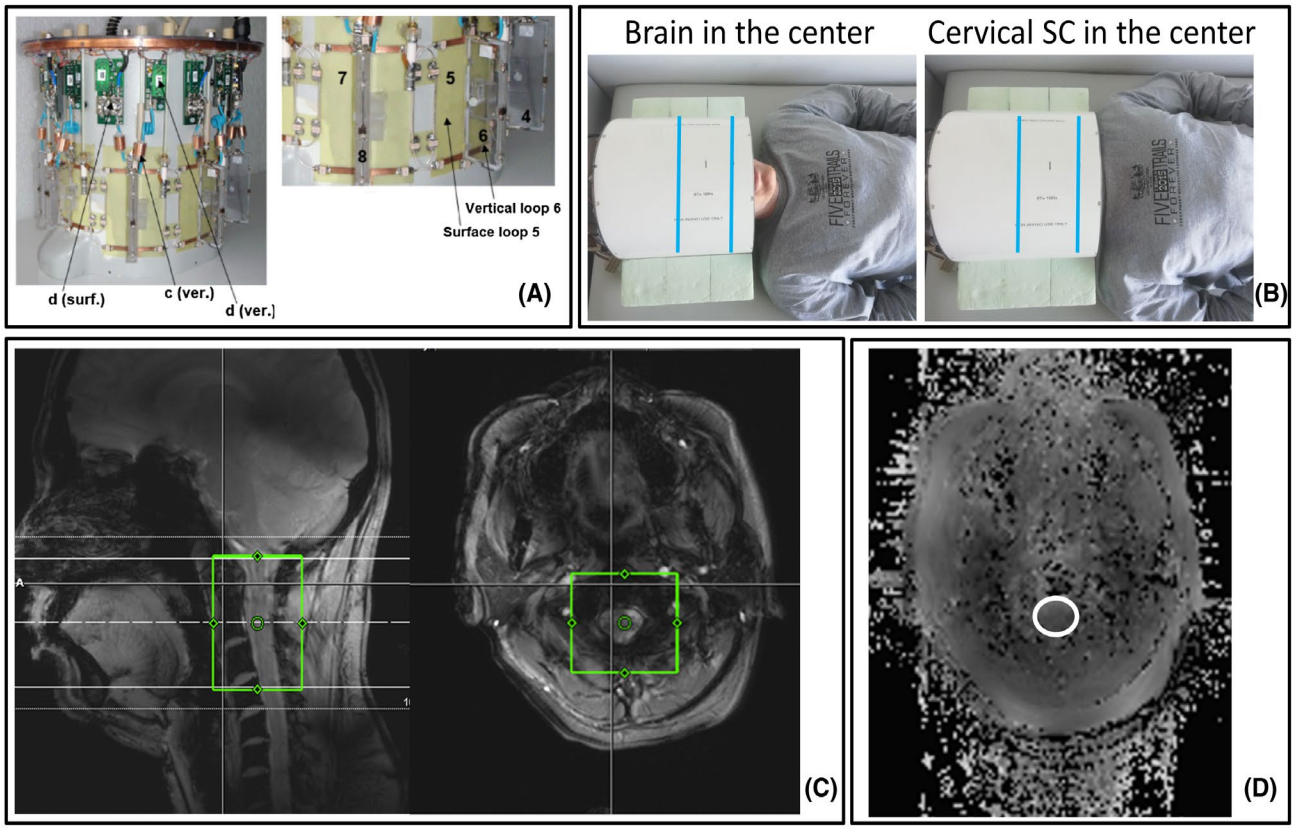

FIGURE 1 A: Photograph of the coil array (without cover) from Avdievich et al.[22] Right photograph: The numbers 4, 6, and 8 represent vertical receive-only loops; the numbers 5 und 7 represent transceiver surface loops. B: Subject positioning. Left photograph: Subject positioning for human brain scans. The brain lays in the center of the loop array. Right photograph: Subject positioning for human cervical spinal cord (SC) scans. The upper cervical SC lays in the center of the loop array. The blue lines mark the beginning and end of the loops. C: Three-dimensional shimming volume (green box) shown on the localizer in a sagittal (left) and transversal (right) slice. From head to feet direction, the volume starts at the transition from the cerebellum to the SC and ends at vertebra C4. In transversal view, the shimming volume is including the SC and approximately 3 cm of the surrounding tissue from left to right and anterior to posterior direction. D: Flip-angle map of a slice positioned similar to the transversal slice in C. The white circle marks the values that were averaged for the adjustment of the transmit voltage.

During RF transmission, the array was driven in the circular polarized mode with a 45° phase shift between adjacent transceiver loops. This was achieved with an eight-way splitter box, with corresponding phase shifts incorporated.

A comprehensive set of safety tests of the RF coil has been performed according to our internal standard operational procedures approved by the local institutional review board; the coil was certified for in vivo use in human subjects as described earlier.[28] The specific absorption rate was continuously monitored and supervised by means of the k-factor,[28] which is incorporated in the coil file. Sequence parameters that would exceed the specific absorption-rate limit are hence not allowed, and the parameters have to be adjusted accordingly prior to the scan. In case the specific absorption rate is still exceeded during the scan, it is stopped automatically by the vendor-integrated specific absorption-rate–monitoring system.

2.2 | Volunteer scans

Ten healthy volunteers (eight men, two women, age: 27.4 ± 4.72 years, weight: 75.4 ± 11.77 kg) were scanned on a 9.4T whole-body MR scanner (Siemens Healthcare, Erlangen, Germany) equipped with a SC72 whole-body gradient system with a maximum amplitude and slew rate of 40 mT/m and 200 mT/m/ms, respectively.

All experiments were performed with the approval of the local ethics committee. Informed signed consent was obtained from each volunteer before each MR experiment.

2.3 | Study design

Each in vivo scan session was performed with the following routine. A localizer sequence was applied and used to position the B_0 shimming volume (Figure 1C). The tested B_0 shim approaches are explained in the B_0 shimming comparison subsection below.

After B_0 shimming, a flip-angle (FA) map using the AFI (Actual Flip-angle Imaging) sequence[29] (field of view (FOV): 243 × 243 mm^2, in-plane resolution: 1.68 × 1.68 mm^2, number of slices: 12, slice thickness: 5 mm, repetition time (TR) = 20/100 ms, TE = 4 ms, FA: 53 degree, acquisition time: 1:47 minutes:seconds, dimension: 3D, R = 2 [Gene Ralized

Autocalibrating Partially Parallel Acquisitions (GRAPPA)]) acceleration) was acquired to check the achieved mean FA at the SC position (see FA map in Figure 1D). If the mean FA was unequal to the desired one, the transmit voltage was adjusted according to the proportion of desired and measured FA. After adjustment of the transmit voltage, the AFI sequence was applied and the mean FA was evaluated again to ensure correct FA adjustment. The FA homogeneity within the SC was assessed visually in the FA map.

All anatomical images were acquired with an axial T_2*-weighted GRE sequence.[23] The sets of parameters used during this study are listed in Table 1. Every time sequence A, B, C, D, E, F, G, H, or I is mentioned in the text, respectively, a GRE sequence with the parameters displayed in Table 1 is referred to. All sequences acquired one average, and phase stabilization was active. Each parameter set was tested on at least three subjects. Sequence B was applied with a slice oversampling of 66%.

2.4 | B_0 shimming comparison

Along the SC the B_0 field varies dramatically because of transitions between bone and intervertebral discs[24,25]; these "B_0 field distortions interfere with encoding of contrast and spatial origin of the MR signal, commonly causing artifacts in the form of signal loss and geometric distortion, but can also contribute to ghosting, blurring and distorted excitation volumes, amongst other effects."[13] Thus, as input for the scan protocol optimization for anatomical SC imaging, multiple B_0 shimming algorithms were compared to investigate the influence of the B_0 shim performance on SC image quality. In particular, the primary focus evaluating B_0 shim performance by the severity of signal dropouts that occur periodically in the intervertebral disc-located slices.

For all tested B_0 shimming routines, the same three-dimensional cuboid B_0 shimming volume was set on the localizer image. The B_0 shimming volume was planned to encompass a region including the SC and approximately 3 cm of the surrounding tissue (Figure 1C).

The first shimming routine was the Siemens implemented image-based shim routine using up to second- order spherical harmonics. Within this routine the B_0 map is measured with a Double-Echo Steady-State (DESS) sequence[30]; based on that, the shim values for each transmit channel were calculated and applied. Frequency adjustment was performed afterwards. The whole B_0 shim procedure was repeated three times to achieve robust convergence, which is necessary because the Siemens shim algorithm implementation does not directly consider B_0 shim field imperfections.

The next tested routine was the Fast, Automatic Shim Technique using Echo-planar Signal readouT for Mapping Along Projections (FASTESTMAP).[31] Again, the process from B_0 mapping to frequency adjust was performed three times before the image acquisition.

The third routine was the ConsTru (constrained TSVD inversion) method.[32] After acquiring the B_0 map (with all shim values set to zero), the ConsTru shim values were calculated and applied to the scanner. Before the anatomical image was measured, the frequency adjust was performed.

Lastly, the straightforward TuneUp shim was applied. The TuneUp shim is the shim setting the vendor determines to deliver a homogeneous magnetic field in a spherical phantom after installing the MR scanner. It characterizes the B_0 shim quality and is often used as an initial point for further B_0 shim calculations.

After adjusting each set of B_0 shim parameters, the anatomical images were acquired with sequence A.

TABLE 1 Description of the parameters of the gradient echo sequences

Sequence	FOV (mm^2)	In-plane resolution (mm^2)	No. of slices	Slice thickness (mm)	TR (ms)	TE (ms)	FA (degree)	Acq. time (min:s)	Dim	Acq. BW (Hz/vx)
A	133 × 133	0.22 × 0.22	9	3	365	9	50	03:40	2D	155
B	189 × 189	1.68 × 1.68	12	5	8.7	2	6	00:20	3D	580
C	150 × 150	0.47 × 0.47	1	3	250	5 or 9 or 14 or 19	25	01:20	2D	155
D	140 × 140	0.23 × 0.23	12	3	500	4 and 10 and 16 and 22	50	05:04	2D	316
E	140 × 140	0.23 × 0.23	12	3	500	5.1 and 9.4 and 13.8 and 17.7	50	05:04	2D	316
F	147 × 147	0.15 × 0.15	10	3	259	12	25	04:14	2D	158
G	147 × 147	0.15 × 0.15	10	3	500	5.1 and 13.8	50	07:46	2D	220
H	147 × 147	0.15 × 0.15	10	3	500	9.4 and 17.7	50	07:46	2D	220
I	160 × 160	0.50 × 0.50	128	1	2800	10	50	15:00	2D	300

Acq. BW: acquisition bandwidth in Hz per voxel; Acq. time: acquisition time; FA: flip angle; FOV: field of view; TE: echo time; TR: repetition time

2.5 | Calculation of the intrinsic signal-to-noise ratio

To create intrinsic SNR maps ("the SNR that would be obtained with a homogeneous FA of 90°, an infinite repetition time and an echo time of zero"[14]), signal measurements were acquired using sequence B. Afterwards a corresponding noise scan was performed by applying the same sequence with the transmit voltage set to zero. Based on the noise data, the noise covariance matrix[33] was calculated. Analogous to Pohmann et al,[14] the pseudo-multiple replica approach[34] was employed. Experimental SNR was then computed with the formulation from Roemer et al[35] for phased array root-sum-of-squares magnitude image combination. Afterwards, these SNR values were corrected with Equation 1 from Pohmann et al,[14] to achieve the intrinsic SNR. The correction was done based on the FA map acquired with the AFI sequence mentioned in the Study design subsection. The intrinsic SNR in the SC was averaged for each slice, respectively.

2.6 | Sequence parameter optimization and high-resolution anatomical images

To show that the RF coil can be used to acquire high-quality anatomical images of the SC, single low-resolution axial slices were acquired with sequence C, utilizing each time another TE (5, 9, 14, or 19 ms) as initial input for scan parameter optimization.

Following the feasibility test, multiecho sequences, where the signal is measured at four different TEs, were applied (sequence D and E). Within these sequences, 12 different transversal slices with an in-plane resolution of 0.23 × 0.23 mm^2 were acquired along the upper cervical SC (level C1, C2, C3, and partly C4). The parameters of sequence E were set analogously to those set in Massire et al,[27] because these TEs produced good results at 7T. The data from both sequence D and E were combined to create MEDIC (Multi Echo Data Image Combination)[36] images and to calculate T_2* maps. MEDIC images were obtained by computing the sum of squares of the image from each TE. To assess the GM/WM contrast for different TEs, the contrast-to-noise ratio (CNR) for each TE and each slice was calculated. We defined the CNR (analogously to Bachmann et al,[9] Fushimi et al,[37] and Constable and Henkelman[38]) as the difference between the mean signal of GM and WM, divided by the standard deviation of artifact free background noise. To average the signal intensities, the GM and WM tissue masks resulting from image segmentation (see Segmentation subsection) were utilized.

By means of the intrinsic SNR, statements for the experimental SNR of acquisitions with different sequence parameter values can be derived. For various values of TE, TR, or FA, Equation 1 from Pohmann et al[14] were employed to calculate the experimental SNR from the intrinsic SNR. For various voxel sizes, matrix sizes, or sequence dimensions, the rules from Constable and Henkelman,[38] Hendrick,[39] Edelstein et al,[40] and Brown et al,[41] were applied. Following these rules, the experimental SNR for the parameters of sequence D and E was derived.

To observe the benefits of very high-resolution images, measurements (sequence F, G, and H) with the highest axial in-plane resolution (0.15 × 0.15 mm^2) achievable with the proposed sequence settings and gradient timings, were performed to make the small SC structures visible. The scanner did not allow the measurement of higher resolutions because the gradients could induce too severe peripheral nerve stimulation. Although sequence F is a single-echo sequence, the sequences G and H are multiecho sequences, with two echoes, respectively. For that high resolution, the scanner did not permit the measurement of four echoes in one sequence because of the risk of too strong nerve stimulation. The data from both sequences G and H were combined to create MEDIC images.

2.7 | Segmentation

Using the Spinal Cord Toolbox (v.4.0; sourceforge.net/projects/spinalcordtoolbox),[42] algorithmic SC detection, as well as GM/WM segmentation within the SC, was performed. The Spinal Cord Toolbox is a comprehensive software program used to process MRI SC data. From the wide range of applications and algorithms implemented in the Spinal Cord Toolbox, the propagated cord segmentation (*function sct_propseg*)[43] for detecting the SC within the full FOV and the deep-learning algorithm with dilated convolutions (*function sct_deepseg_gm*)[44] to segment the GM within SC were employed. Once the SC detection and the GM segmentation were executed successfully, the WM segments were detected by subtracting the GM mask from the full SC mask. To test the SC detection algorithm, a GRE sequence acquiring 128 slices (sequence I, slice thickness: 1 mm) was applied. With these 128 transversal slices, it was possible to create sufficient sagittal and coronal coverage to visualize the SC detection result in all three dimensions. The SC detection algorithm was also tested on the data acquired with sequence D and E. Additionally, on this data the GM segmentation algorithm was applied.

2.8 | T_2*-time calculation for gray matter and white matter

To perform pixel-wise T_2*-time calculations, the multiecho results from sequences D and E were employed. In addition

to the four TEs adopted from Massire et al[27] (sequence E), another four TEs (sequence D) were measured. This yielded eight, instead of four, sample points per pixel to calculate a more accurate mono-exponential fit. The fitting was performed with a nonlinear least squares algorithm using MATLAB (MathWorks, Natick, MA).

To calculate the average T_2*-relaxation times of GM and WM separately, the segmented GM and WM tissue masks were applied to T_2* maps. All the fitted T_2* values of GM and WM pixels from three subjects were pooled to calculate mean GM and WM specific T_2*-relaxation times and a two-sample *t* test was performed with MATLAB to investigate statistically significant differences.

3 | RESULTS

3.1 | B_0 shimming comparison

Figure 2 presents the results acquired with sequence A. The Siemens shim routine offered the images with the best quality and was consequently utilized for all of the following measurements. Most notably, the Siemens shim performed much better in the first and second slice. Signal dropouts, which are visible for the other three set-ups, arose just marginally for the Siemens shim. For slices three to six, all routines provided excellent image quality. The Tune-Up shim, which consists of a fixed set of shim values, delivered similar image quality to those of other shimming routines. For slice seven, the Siemens shim again offered the best image quality. Because this slice touched a disc, a slight signal dropout occurred in the lower area of the SC and cerebrospinal fluid (CSF). This dropout worsened for Tune-Up, FASTESTMAP, and ConsTru shim relative to the Siemens shim. For slices eight and nine, again all routines provided similar, sufficient image quality.

3.2 | Calculation of the intrinsic signal-to-noise ratio

Figure 3A shows a map of the intrinsic SNR, represented by 6 out of the 12 measured slices. For the two presented subjects, the highest SNR in the SC was achieved in slices 3 to 10, with values mostly observed between 6600 and the maximum of 8060 (subj.1, slice 4). For slices positioned further in the head direction than slice 3 and placed further in the feet direction than slice 10, the SNR dropped dramatically (Figure 3B).

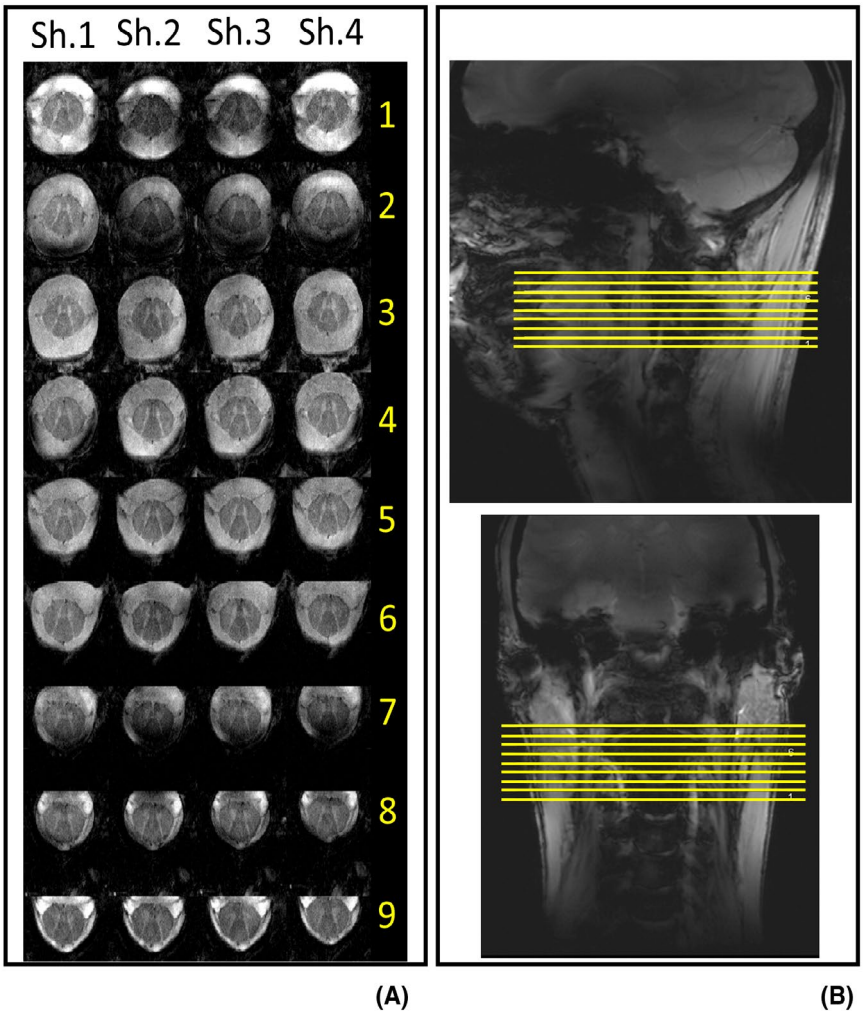

FIGURE 2 A: Comparison of the influence of different shimming routines. All images were acquired with gradient echo (GRE) sequence A. The table of images presents different slices (labeled with the yellow numbers) acquired with the same shim set-up in the columns and same slices acquired with different shim set-ups (Sh.1 = Siemens shim, Sh.2 = TuneUp, Sh.3 = fast, automatic shim technique using echo-planar signal readout for mapping along projections [FASTESTMAP], Sh.4 = ConsTru) in the rows. Enlargements of the full field of view are shown. B: The top (bottom) image presents the central sagittal (coronal) slice. The yellow lines mark the position of the transversal slices, depicted in A

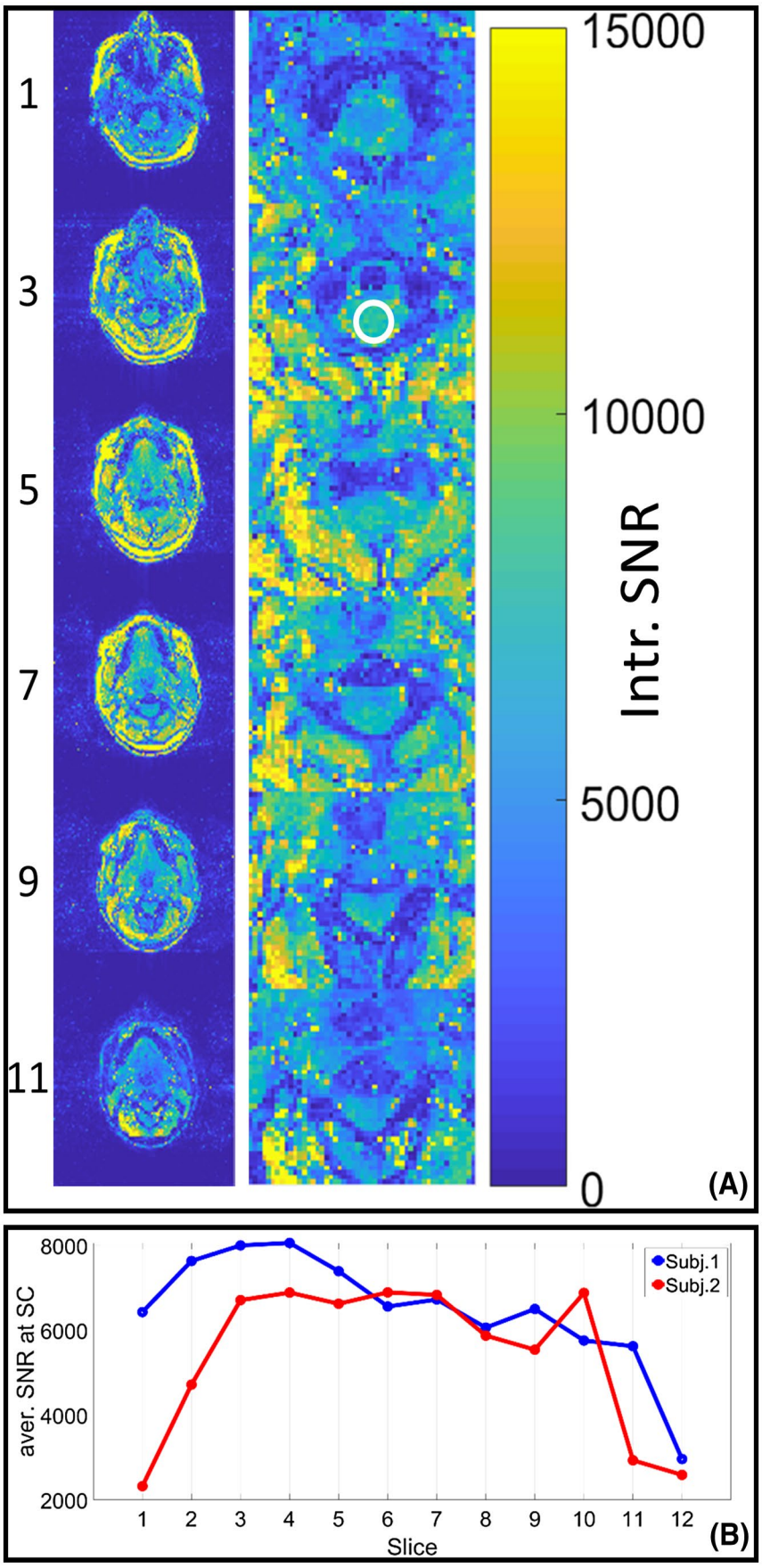

FIGURE 3 A, Intrinsic signal-to-noise ratio (SNR) map. Six of 12 measured slices are displayed by skipping every second slice. From left to right, the number of the displayed slice, the full field of view of that slice, and an enlargement of the spinal cord (SC) is visible. The slice positioning is similar to Figure 2B. The white circle in slice three marks the values that were averaged. The same circle (adjusted for the SC position, respectively) was used in each slice. B, Slice-wise averaged SNR values for two subjects. The SNR map from subject 1 is shown in A

3.3 | Sequence parameter optimization and high-resolution anatomical images

First, a single slice with a low in-plane resolution of 0.47 × 0.47 mm^2 was measured four times, each time with a different TE. Figure 4 displays the FOV of one volunteer. Anteriorly, the teeth can be seen and on the posterior side, the neck muscles are visible. In the center of the FOV, the SC is surrounded by CSF (yellow box) and the vertebrae. In the four surrounding images in Figure 4, enlargements from the

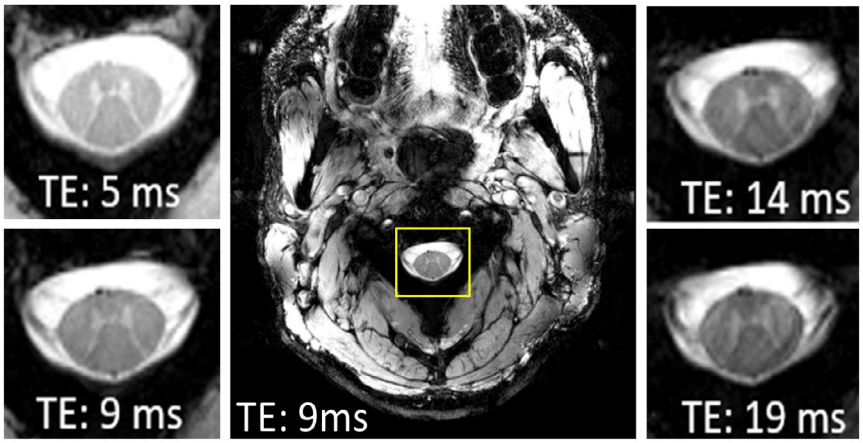

FIGURE 4 Comparison of images, acquired with gradient echo (GRE) sequence C (in-plane resolution: 0.47 × 0.47 mm^2) and four different echo times (TEs). Central picture: Full transversal field of view of the measurement with TE: 9 ms. The yellow box marks the position of the enlargement, which is visible in the four surrounding pictures. Surrounding pictures: Enlargements of the spinal cord measured at four different TEs (one TE per sequence application)

FOV at the SC location at different TEs are displayed. At a short TE of 5 ms, a high signal with low GM/WM contrast is visible. With increasing TE, the signal has partially decayed and GM/WM contrast has increased. The "butterfly" shape of the GM is clearly visible and distinguishable from the WM for a TE of 9 ms and 14 ms; furthermore, nerve roots at the left and right side of the SC are apparent. A TE of 19 ms seems to be too long, as GM/WM contrast has diminished and magnetic susceptibility effects appear, especially in the CSF.

In Figure 5A, the results of the two multiecho GRE sequences D (TEs: 4/10/16/22 ms) and E (TEs: 5.1/9.4/13.8/17.7 ms) with an in-plane resolution of 0.23 × 0.23 mm^2 are depicted. Figure 5B shows the corresponding CNR for each slice and TE. Figure 5C illustrates the averaged experimental SNR in the SC for each TE recalculated from the intrinsic SNR depicted in Figure 3B (Subj.1).

As Figure 4 has already shown, as TE increases, the signal decays and GM/WM contrast grows. While a TE of less than 9.4 ms seems too short to achieve a strong visual GM/WM contrast, a TE of between 9.4 ms and 13.8 ms provided the best compromise between signal intensity and tissue contrast as illustrated in Figure 5A. Confirming this observation, the CNR between GM and WM is increasing from a TE of 4 ms until 13.8 ms for most slices. After 13.8 ms, the CNR is decreasing or rises only marginally.

Slice five is located at an intervertebral disc location. With increasing TE, a signal dropout occurred here. While this dropout does not or only marginally occurs for the first four TEs, it became severe for a TE of 13.8 ms and longer. To not adulterate the CNR of that slice, the GM and WM masks were corrected manually to exclude the pixels where the dropout occurs (see Supporting Information Figure S1 for the CNR values including signal dropout).

The experimental SNR is decreasing along an exponential curve with increasing TE. In slice three (which had one of the highest intrinsic SNR values of 8000 as seen in Figure 3) the highest experimental SNR was acquired.

The MEDIC images offer excellent GM/WM contrast, as it can be seen in the images in Figure 5A, as well as from the CNR values in Figure 5B. For instance, slice three provides a CNR of 4.95 at a TE of 13.8 ms and a CNR of 7.95 for the MEDIC image.

The results given in Figure 5 were acquired with a TR of 500 ms and a FA of 50°; the results given in Figure 4 were acquired with a TR of 250 ms and a FA of 25°. After a proper scaling, there is no visible difference in the image quality.

As TEs between 9 and 13.8 ms are good compromises between tissue contrast and minimal magnetic susceptibility effects, a TE of 12 ms was chosen for the single-echo measurements with an in-plane resolution of 0.15 × 0.15 mm^2 (sequence F). In all depicted slices (Figure 6A), high-quality images of the SC are visible. GM and WM can be distinguished. Nerve roots and blood vessels are shown in excellent detail in most of the slices. The anterior median fissure and the posterior median septum are recognizable. The same is valid for the MEDIC images (Figure 6B) created out of the measurements acquired with multiecho sequences G and H. The MEDIC images offer improved GM/WM contrast compared with the single-echo measurements, while showing similar sharpness and number of details.

For comparison, Figure 6C,D show 7T GRE acquisitions from Sigmund et al[10] and Massire et al[27] with an in-plane resolution of 0.18 × 0.18 mm^2.

3.4 | Segmentation

The white-colored pixels in Figure 7 mark the SC, as it was masked by the SC detection algorithm. All white-colored pixels mark the location of the spinal cord in each perspective correctly, except for the bottom slices, where the SC was not detected.

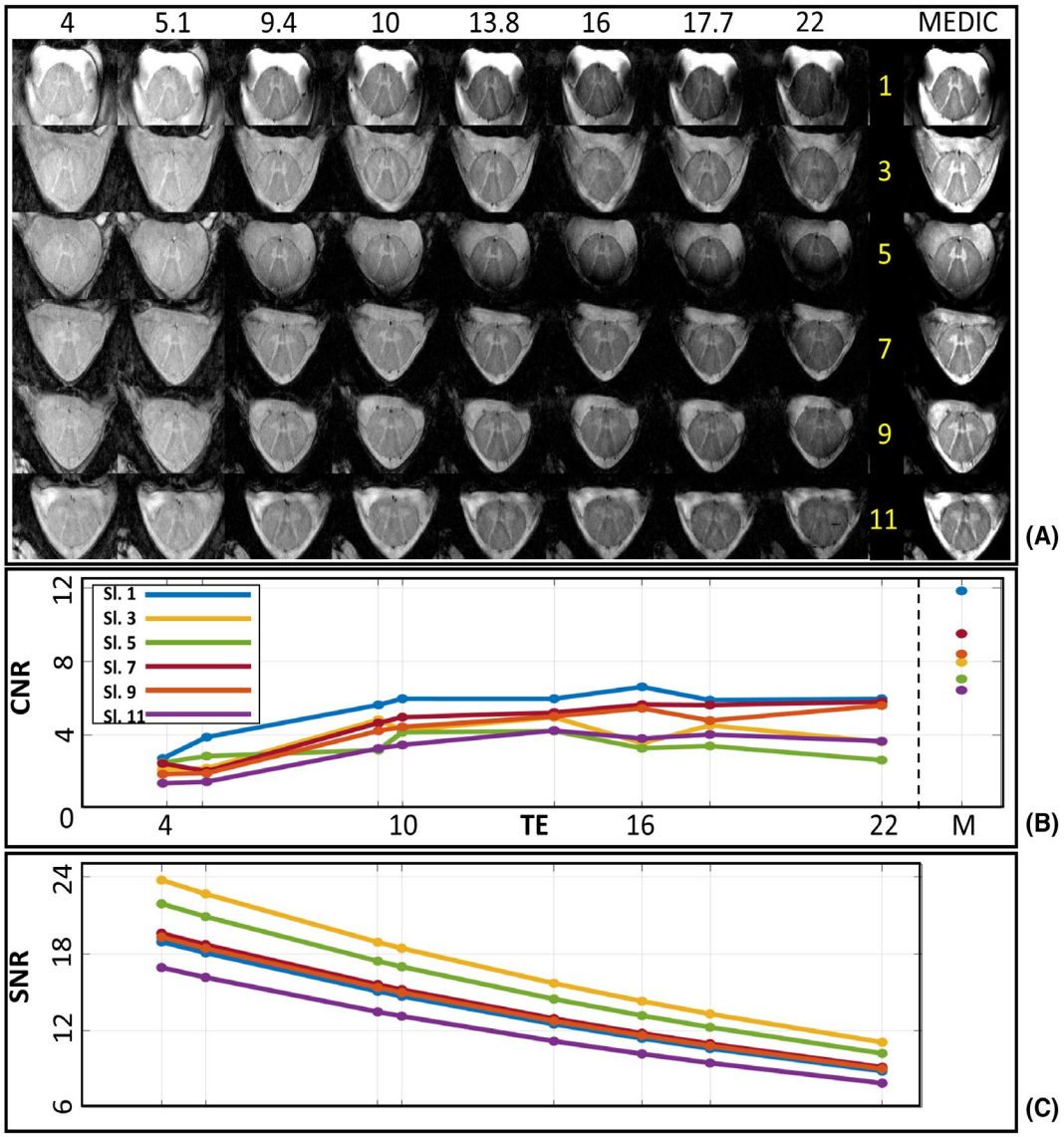

FIGURE 5 A: Images acquired with two multiecho gradient-echo (GRE) sequences D (TE: 4/10/16/22 ms) and E (TE: 5.1/9.4/13.8/17.7 ms) (in-plane resolution: 0.23 × 0.23 mm^2). Six out of 12 measured slices are displayed by skipping every second slice. The slice positioning is similar to Figure 2B. In A, enlargements of the spinal cord (SC) are visible. Each column presents the measurements from different slices (slice number displayed by yellow numbers) at a certain echo time (TE; depicted at the header in ms). Each row presents measurements from the same slice position, but at a different TE. The very right column of images show scaled multiecho data image combination (MEDIC) images calculated as the sum of squares from the eight measurements from the table of images. B: Plot of the contrast-to-noise ratio (CNR) values for all of the SC images shown in A. Each line presents the CNR values of a certain slice at different TEs and in the MEDIC image. C: Plot of the averaged experimental SNR values in the SC recalculated from the intrinsic SNR in Figure 3B (Subj.1). Each line presents the SNR values of a certain slice at different TEs. The x-axis and the legend is equal to B

On the slices acquired with sequence D and E, the SC detection algorithm and the GM segmentation algorithm were applied. Figure 8 shows three segmented example slices. The algorithm detected the SC and segmented GM and WM correctly. The typical butterfly shape is observed as depicted by white pixels in the GM mask.

3.5 | T_2*-time calculation for gray matter and white matter

For each of the three subjects that were measured with multiecho sequences D and E (12 slices acquired per sequence), a T_2* map was calculated. Figure 9 shows an example slice, where the CSF and the SC are distinguishable; to some extent, the GM and WM within the SC are also discernible. T_2* slices, in which these tissue types were not recognizable because of midvertebra disks-related signal dropouts, were excluded from averaging. Based on the created GM and WM masks, mean T_2* values were calculated. For the cervical SC at 9.4T, the calculated T_2* value for GM is 24.88 ms ± 6.68 ms and for WM 19.37 ms ± 8.66 ms.

A two-sample *t*-test results in *p* value of $1.6233*10^{-271}$ for the null hypothesis ("The mean of the GM sample is equal to the mean of the WM sample."). For that reason, the null hypothesis needs to be rejected. Thus, the means of GM and WM T_2*-relaxation times differ significantly.

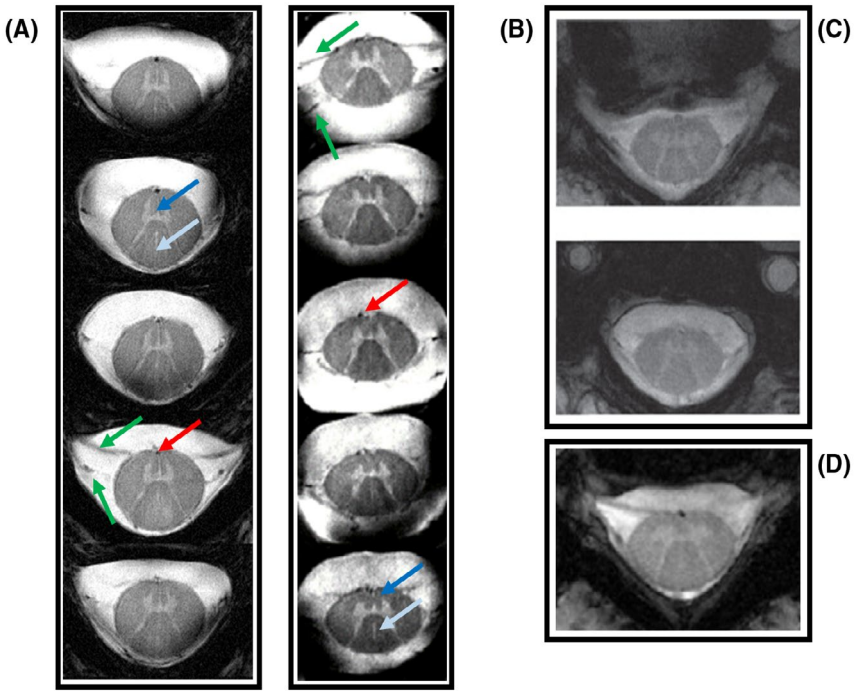

FIGURE 6 A: 9.4T spinal cord (SC) images acquired with single-echo gradient echo (GRE) sequence F (in-plane resolution: 0.15 × 0.15 mm^2). B: 9.4T multiecho data image combination (MEDIC) images calculated from the measurements acquired with multi-echo sequence G and H (in-plane resolution: 0.15 × 0.15 mm^2). 5 of 10 measured slices are displayed by skipping every second slice. Nerve roots (green arrows), blood vessels (red arrow), the anterior median fissure (dark blue arrow), and the posterior median septum (sky blue arrow) are marked. C: 7T SC GRE images from Sigmund et al.[10] D: 7T SC GRE image from Massire et al.[27]. C and D have an in-plane resolution of 0.18 × 0.18 mm^2

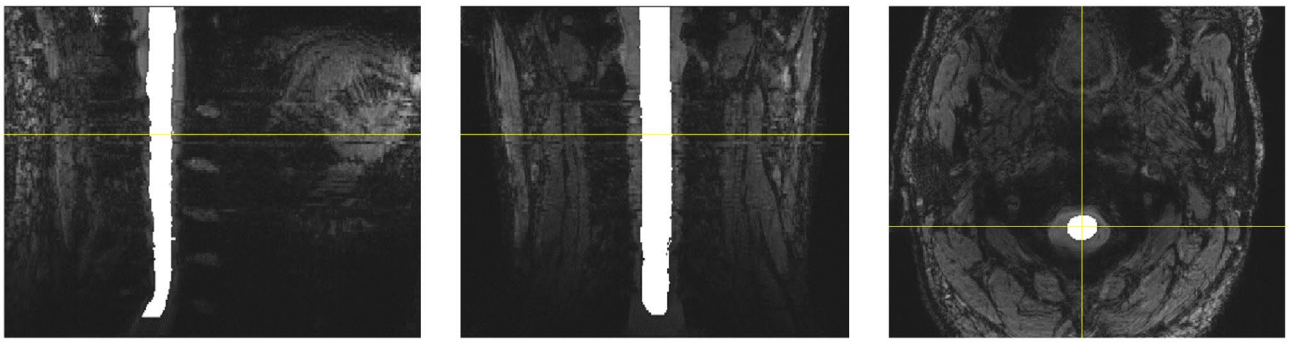

FIGURE 7 Spinal cord (SC) detection applied on the images acquired with sequence I. From left to right, sagittal, coronal, and a transversal slices are displayed. The yellow line on the sagittal and coronal image marks the position of the transversal slice in the right picture. The yellow vertical line in the transversal slice marks the position of the sagittal slice. The yellow horizontal line in the transversal slice marks the position of the coronal slice. The white-colored pixels in each image show the SC that the SC-detection algorithm determined

4 | DISCUSSION

This work presents the first in vivo MR images of the human SC measured at the B_0 field strength of 9.4T. An RF coil optimized for central SNR in the human brain was employed to acquire in vivo cervical SC images.

A TE between 9 and 13.8 ms was found to offer the best image quality with an excellent contrast between CSF, GM, and WM (Figures 4 and 5). That TE recommendation is slightly higher in comparison with what Sigmund et al[10] suggested at 7T with their SC-dedicated coil (GRE sequence with TE = 4.91 ms). In comparison with the noncombined data, the combined MEDIC images[36] show improved image quality in terms of tissue contrast. Because the acquisition of multiecho data does not require additional scan time, MEDIC is an attractive alternative to single-echo measurements. Slice one in Figure 5A shows high contrast between CSF and the SC largely independent of TE, which possibly occurs because of the reduction in transmit B_1^+ field at the edge of the FOV of the RF coil in that slice position.

The highest axial in-plane resolutions (in vivo) acquired prior to this work were 0.18 × 0.18 mm^2 by Sigmund et al[10] (Figure 6C) and Massire et al[27] (Figure 6D) at a field strength of 7T with SC-dedicated coils. We presented

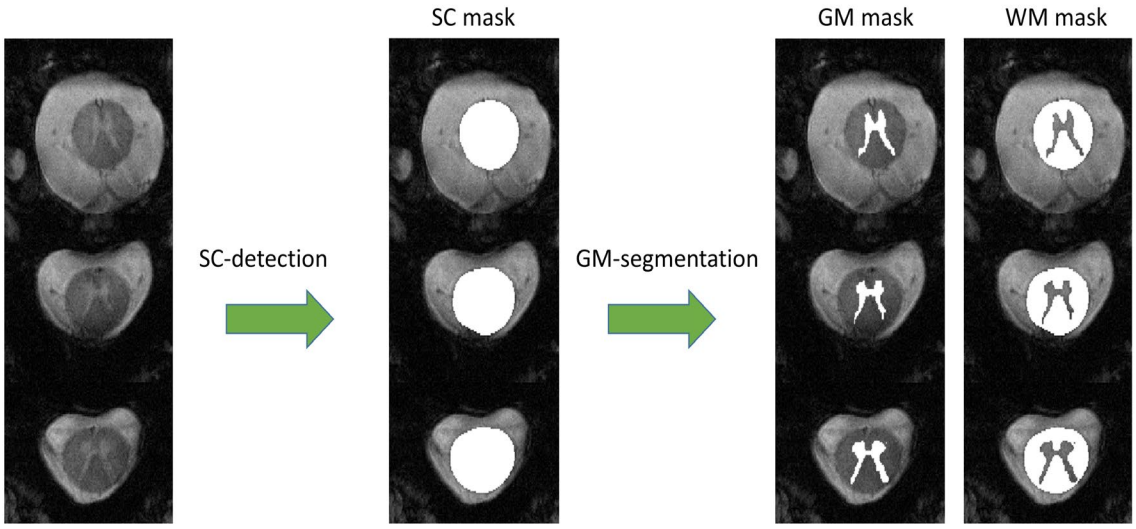

FIGURE 8 Spinal cord (SC) and gray matter (GM) segmentation applied on the results acquired with gradient echo sequence E (echo time: 9.4 ms). Enlargements of three transversal example slices are shown in the left column of images. The central column of images depicts where the SC-detection algorithm determines the SC (white-colored pixels). On the right hand side, one column depicts where the GM-segmentation algorithm determines the GM (white-colored pixels) within the SC. The other column presents the white matter (WM) pixels

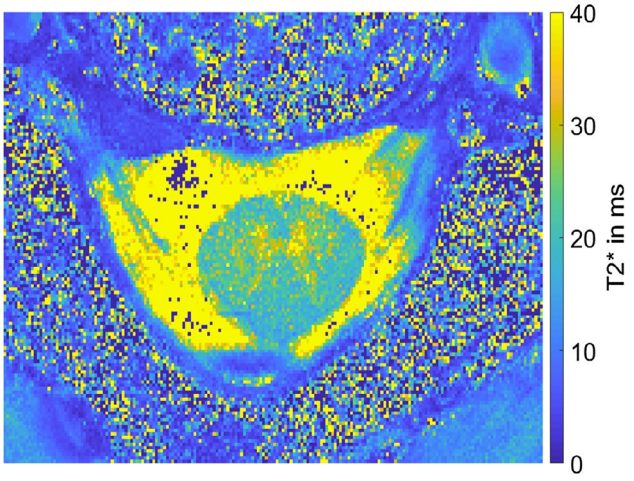

FIGURE 9 Enlargement at the spinal cord position of an example slice from a T_2* map

an improved resolution of 0.15 × 0.15 mm^2. That means in the 9.4T images (Figure 6A,B) the area of each pixel is decreased by approximately 30% from 0.0324 mm^2 to 0.0225 mm^2 compared with the 7T acquisitions. The 9.4T results show the small SC structures in excellent detail. The quality of these images seems to outperform the 7T results, as the nerve roots are also visible at 7T, but are not as sharp as at 9.4T. Moreover, the anterior median fissure and the posterior median septum are recognizable in T_2*-weighted images at 9.4T, whereas they are hard to detect at 7T.[10,27] In the most recent work from Massire et al,[45] these two structures are recognizable on 7T T_1 maps of the SC, but again difficult to detect on T_2*-weighted images, as is possible at 9.4T.

Compared with the acquisitions with an in-plane resolution of 0.23 × 0.23 mm^2 (Figure 5A), the 0.15 × 0.15 mm^2 images present the SC in slightly improved acuity. However, the enhancement may not be as strong as expected from the difference between both spatial resolutions. A possible reason for this is the physiological SC motion (between 0.40 and 0.50 mm in superior/inferior, 0.60 ± 0.34 mm in anterior/posterior, and 0.17 ± 0.09 mm in right/left direction[46,47]), which possibly blurs images, especially in cases of very high spatial resolutions. Cardiac triggering or prospective motion correction[48] could be an option to mitigate the influence of motion; however, it was not applied during this study. Future work should test whether image acuity at a spatial resolution of 0.15 × 0.15 mm^2 can be improved and even higher spatial resolutions are feasible by including optimized motion compensation methods and encoding schemes that prevent excessive peripheral nerve stimulation. Even if a higher spatial resolution would be possible technically, it remains to be clarified whether this can further improve diagnostic specificity and sensitivity.

T_2* maps were derived from multiecho GRE images and showed clear distinction between GM, WM, and CSF. By means of the Spinal Cord Toolbox, masks for GM and WM were calculated, and the T_2* times for all GM and WM voxels inside the respective masks were averaged. Although an uncertainty remains when using this pixel-by-pixel fit method (see noise in Figure 9 and the resulting relatively high SD) the first estimate of T_2* times in the human SC at 9.4T has been presented (GM 24.88 ms ± 6.68 ms and for WM 19.37 ms ± 8.66 ms) and a statistically significant difference was found between GM and WM. These results are consistent with the literature. While Massire et al[27] presented the

expected slightly higher T_2*times from the cervical SC at 7T (GM: 29.3 ms ± 4.5 ms, WM: 23.5 ms ± 5.7 ms), Pohmann et al[14] published T_2*times at 9.4T for the human brain (GM: 23.8 ms ± 1.0 ms, WM: 19.2 ms ± 0.9 ms), which are very similar to the values calculated for the SC at 9.4T.

Periodic signal dropouts were observed in slices near intervertebral discs, possibly due to strong magnetic susceptibility between soft tissue and bone.[24,25] although among the herein investigated B_0 shimming approaches, the vendor-implemented second-order B_0 shimming offers the best image quality for slices next to intervertebral disks; in general, the differences within the four different shimmed images are not very prominent (Figure 2). Even the TuneUp shim, which is a fixed set of shim values, does not have a substantially poorer performance in most slices in comparison with FASTEST MAP and ConsTru. Although the vendor shim mitigates the dropouts, it did not obliterate it. Tackling the B_0 inhomogeneities for SC imaging remains a future challenge. A possible solution could be dedicated B_0 shim hardware.[49-53] In addition, a 3T study showed improved B_0 homogeneity within the neck by placing pyrolytic graphite foam behind the neck[54]; this could also be worth investigating at ultrahigh field.

The simplicity of the utilization of a 16-channel transceiver array RF coil driven in circular polarized mode for SC imaging that was originally optimized to yield high SNR in central brain structures and high transmit efficiency for brain MRI and MRS is worth noting. Utilizing the same coil for both brain and cervical SC applications is cost-efficient and offers the opportunity to tackle "the lack of commercial SC-dedicated coils" as reported in Massire et al.[27] There is no costly development of a SC-dedicated coil needed to achieve comparable results for the cervical SC. Two of the 10 subjects reported that the positioning inside the coil was not as comfortable as for brain scans; however, no subject needed to interrupt or abort a scan session.

We chose to investigate the intrinsic SNR of the SC (ie, the SNR in the situation of a homogeneous FA of 90°, an infinite TR and an TE of zero) to achieve a normalized SNR value that allows for the comparison between different field strength and hardware set-ups by correcting for the influence of the sequence parameters. It is worth noting that the reported intrinsic SNR values featured in Figure 3 are not achievable in experiments.

The intrinsic SNR reported in Pohmann et al[14] (approximately 3000 in brain center at 9.4T, but smaller voxel size as in sequence B) can be recalculated with respect to the parameter values from sequence B by multiplying it with a factor of 3.2 (eq. 7.12 from Hendrick[39]). With the coil[55] used in Pohmann et al[14] and the settings from sequence B, the intrinsic SNR in the brain center theoretically would be 9600. This value is higher than the intrinsic SNR that was acquired in the SC during this study (Figure 3; SNR between 6600 and 8060 in slices 3 to 10). The lower SNR in the SC compared with the brain center at 9.4T is most likely caused by the different coil set-ups utilized. The dedicated brain coil[55] has 31 receive channels arranged on a close-fitting helmet to maximize SNR. The coil employed in this study was a single row eight-channel transceiver coil with eight additional receive-only elements and has, therefore, a limited coverage, which negatively impacts central SNR.[15] On the other hand, the combination of transceiver loops and dipolar receive-only elements was designed to enhance the SNR in deep-brain structures.[22] The design of the coil used herein allows SC applications, which is not the case for the dedicated brain coil design in Pohmann et al.[14] However, the coil loading differs between the subject position for SC imaging and brain imaging (Figure 1B), which may also lead to SNR losses. All these influence factors could be reasons for the slightly lower SNR in the SC as compared with the central brain at 9.4T.[14]

In Sigmund et al,[10] the authors report an average experimental SC SNR in vivo of 227 at 7T. If we recalculate the intrinsic SNR from this study (Figure 3, slices 3 to 10) with respect to the sequence parameter from Sigmund et al[10] (utilizing eq. 7.12 from Hendrick[39] and eq. 1 from Pohmann et al,[14] acquisition bandwidth was not mentioned; therefore, we assumed the same bandwidth as in sequence B) and we achieved an experimental SNR between 265 and 324. The SNR increase was expected; however, it is not as high as the change from 7T to 9.4T may imply.[14,15]

In general, an increase of the static magnetic B_0 field strength leads theoretically to an almost quadratic increase of SNR and thus doubles the SNR at 9.4T versus 7T for similar sequences and coils.[14,15] Furthermore, at high field a combination of surface loops and dipolar elements is needed for SNR optimization in central regions.[15] In addition, wrap-around coils (such as the coil in Zhang et al[56]), tend to provide higher SNR compared with the neck coils used by Sigmund et al[10] and Zhao et al[11] with only posterior elements. Both advantages are incorporated in the coil proposed herein.

The decreased SNR in slices 1, 2, 11, and 12 (Figure 3), as well as the failed SC detection in the lowest positioned slices in Figure 7, indicates a drawback of the proposed coil: the relatively small longitudinal coverage for areas that are not placed in the center of the loops. Vertebras C1, C2, C3, and to some extent, C4 can be covered excellently, but reaching any lower vertebra seems to be problematic. In addition, measuring the brain and the SC within the same scan is not possible. To achieve extended coverage, other array architectures (eg, with dipole receive elements instead of loops[57] or SC-dedicated coils (eg, see Sigmund et al,[10] Zhao et al,[11] Kraff et al,[58] or Barry et al[13] for an overview of all 7T SC coils) need to be employed. Having a coil design that considers the principles of the proposed coil, but is further optimized for SC imaging could improve results with respect

to longitudinal coverage, SNR, and subject comfort. With an extended longitudinal coverage, the brain and the SC could be imaged in the same experiment, as it is necessary to assess the functional connectivity between both regions.

With this work, we have taken the first step into SC research at a B_0 field strength higher than 7T. By testing and optimizing other sequences (eg, magnetization-prepared 2 rapid gradient echoes [MP2RAGE],[59] T2W, echo planar imaging, MRS, or the AMIRA approach[60]) in the future, anatomical image quality could be further improved and multimodal SC imaging at 9.4T can be enabled. Furthermore, T_1- and T_2-relaxation-time measurements need to be performed to complete the set of tissue relaxation times as input for sequence optimization and quantitative MRI for the SC at 9.4T.

5 | CONCLUSION

With this work, the first step into SC research at a B_0 field strength of 9.4T was performed. With an RF coil, originally optimized for maximal SNR and transmit efficiency in deep brain structures, we were able to acquire high-resolution (in-plane: 0.15×0.15 mm^2) anatomical SC data in excellent detail and quality. Algorithmic SC detection, as well as GM/WM segmentation, reliably works on the data. The T_2*times of GM and WM in the human SC at 9.4T were presented. Such high-resolution images at ultrahigh field of the human SC might open new possibilities in the field of SC research and clinical patient care. Knowing the T_2*-relaxation time allows optimization of imaging parameters and potentially enables improvements in sensitivity and contrast.

ACKNOWLEDGMENTS

Funding by the European Union (ERC Starting Grant, SYNAPLAST MR, Grant Number: 679927) and the Cancer Prevention and Research Institute of Texas (Established Investigator Award RR180056) is gratefully acknowledged. We would like to thank Rolf Pohmann for supporting us with the SNR maps. In addition, we appreciate the help from Andrew Wright and Saipavitra Murali Manohar for text proofreading. Open access funding enabled and organized by Projekt DEAL.

ORCID

Ole Geldschläger https://orcid.org/0000-0002-8400-0635
Nikolai I. Avdievich https://orcid.org/0000-0001-7608-0869

REFERENCES

1. Ciccarelli O, Werring DJ, Barker GJ, et al. A study of the mechanisms of normal-appearing white matter damage in multiple sclerosis using diffusion tensor imaging. *J Neurol*. 2003;250:287-292.
2. Ciccarelli O, Wheeler-Kingshott CA, McLean MA, et al. Spinal cord spectroscopy and diffusion-based tractography to assess acute disability in multiple sclerosis. *Brain*. 2007;130:2220-2231.
3. Kearney H, Schneider T, Yiannakas MC, et al. Spinal cord grey matter abnormalities are associated with secondary progression and physical disability in multiple sclerosis. *J Neurol Neurosurg Psychiatry*. 2014;86:608-614.
4. Sach M, Winkler G, Glauche V, et al. Diffusion tensor MRI of early upper motor neuron involvement in amyotrophic lateral sclerosis. *Brain*. 2004;127:340-350.
5. Demir A, Ries M, Moonen CTW, et al. Diffusion-weighted MR imaging with apparent diffusion coefficient and apparent diffusion tensor maps in cervical spondylotic myelopathy. *Radiology*. 2003;229:37-43.
6. Mahmood NS, Kadavigere R, Ramesh AK, Rao VR. Magnetic resonance imaging in acute cervical spinal cord injury: A correlative study on spinal cord changes and 1 month motor recovery. *Spinal Cord*. 2008;46:791-797.
7. Gilmore CP, Geurts JJG, Evangelou N, et al. Spinal cord grey matter lesions in multiple sclerosis detected by post-mortem high field MR imaging. *Mult Scler J*. 2008;15:180-188.
8. Sicotte NL, Voskuhl RR, Bouvier S, Klutch R, Cohen MS, Mazziotta JC. Comparison of multiple sclerosis lesions at 1.5 and 3.0 Tesla. *Invest Radiol*. 2003;38:423-427.
9. Bachmann R, Reilmann R, Schwindt W, Kugel H, Heindel W, Krämer S. FLAIR imaging for multiple sclerosis: A comparative MR study at 1.5 and 3.0 Tesla. *Eur Radiol*. 2005;16:915-921.
10. Sigmund EE, Suero GA, Hu C, et al. High-resolution human cervical spinal cord imaging at 7 T. *NMR Biomed*. 2011;25:891-899.
11. Zhao W, Cohen-Adad J, Polimeni JR, et al. Nineteen-channel receive array and four-channel transmit array coil for cervical spinal cord imaging at 7T. *Magn Reson Med*. 2013;72:291-300.
12. Dula AN, Pawate S, Dortch RD, et al. Magnetic resonance imaging of the cervical spinal cord in multiple sclerosis at 7T. *Mult Scler J*. 2015;22:320-328.
13. Barry RL, Vannesjo SJ, By S, Gore JC, Smith SA. Spinal cord MRI at 7T. *NeuroImage*. 2018;168:437-451.
14. Pohmann R, Speck O, Scheffler K. Signal-to-noise ratio and MR tissue parameters in human brain imaging at 3, 7, and 9.4 Tesla using current receive coil arrays. *Magn Reson Med*. 2015;75:801-809.
15. Pfrommer A, Henning A. The ultimate intrinsic signal-to-noise ratio of loop- and dipole-like current patterns in a realistic human head model. *Magn Reson Med*. 2018;80:2122-2138.
16. Geldschläger O, Manohar SM, Wright A, Avdievitch N, Henning A. First MRI of the human spinal cord at 9.4T. In 27th ISMRM; Montreal, Canada. 2019. Abstract number: 1585.
17. Scholtes F, Adriaensens P, Storme L, et al. Correlation of postmortem 9.4 Tesla magnetic resonance imaging and immunohistopathology of the human thoracic spinal cord 7 months after traumatic cervical spine injury. *Neurosurgery*. 2006;59:671-678.
18. Chen LM, Mishra A, Yang PF, Wang F, Gore JC. Injury alters intrinsic functional connectivity within the primate spinal cord. *Proc Natl Acad Sci USA*. 2015;112:5991-5996.
19. Wang F, Qi HX, Zu Z, et al. Multiparametric MRI reveals dynamic changes in molecular signatures of injured spinal cord in monkeys. *Magn Reson Med*. 2014;74:1125-1137.
20. Bilgen M, Al-Hafez B, Berman NEJ, Festoff BW. Magnetic resonance imaging of mouse spinal cord. *Magn Reson Med*. 2005;54:1226-1231.

21. Ellingson BM, Kurpad SN, Li SJ, Schmit BD. In vivo diffusion tensor imaging of the rat spinal cord at 9.4T. *J Magn Reson Imaging*. 2008;27:634-642.
22. Avdievich NI, Giapitzakis IA, Pfrommer A, Borbath T, Henning A. Combination of surface and "vertical" loop elements improves receive performance of a human head transceiver array at 9.4 T. *NMR Biomed*. 2017;31:e3878.
23. Bernstein M, King K, Zhou X. *Handbook of MRI Pulse Sequences*. Oxford: Elsevier; 2004.
24. Cooke FJ, Blamire AM, Manners DN, Styles P, Rajagopalan B. Quantitative proton magnetic resonance spectroscopy of the cervical spinal cord. *Magn Reson Med*. 2004;51:1122-1128.
25. Finsterbusch J, Eippert F, Büchel C. Single, slice-specific z-shim gradient pulses improve T_2*-weighted imaging of the spinal cord. *NeuroImage*. 2012;59:2307-2315.
26. Hock A, Fuchs A, Boesiger P, Kollias SS, Henning A. Electrocardiogram-triggered, higher order, projection-basedB-0shimming allows for fast and reproducible shim convergence in spinal cord1H MRS. *NMR Biomed*. 2012;26:329-335.
27. Massire A, Taso M, Besson P, Guye M, Ranjeva JP, Callot V. High-resolution multi-parametric quantitative magnetic resonance imaging of the human cervical spinal cord at 7T. *NeuroImage*. 2016;143:58-69.
28. Hoffmann J, Henning A, Giapitzakis IA, et al. Safety testing and operational procedures for self-developed radiofrequency coils. *NMR Biomed*. 2015;29:1131-1144.
29. Yarnykh VL. Actual flip-angle imaging in the pulsed steady state: A method for rapid three-dimensional mapping of the transmitted radiofrequency field. *Magn Reson Med*. 2007;53:192-200.
30. Bruder H, Fischer H, Graumann R, Deimling M. A new steady-state imaging sequence for simultaneous acquisition of two MR images with clearly different contrasts. *Magn Reson Med*. 1988;7:35-42.
31. Gruetter R, Tkac I. Field mapping without reference scan using asymmetric echo-planar techniques. *Magn Reson Med*. 2000;43:319-323.
32. Nassirpour S, Chang P, Fillmer A, Henning A. A comparison of optimization algorithms for localized in vivo B0 shimming. *Magn Reson Med*. 2017;79:1145-1156.
33. Kellman P, McVeigh ER. Image reconstruction in SNR units: A general method for SNR measurement. *Magn Reson Med*. 2005;54:1439-1447.
34. Robson PM, Grant AK, Madhuranthakam AJ, Lattanzi R, Sodickson DK, McKenzie CA. Comprehensive quantification of signal-to-noise ratio andg-factor for image-based andk-space-based parallel imaging reconstructions. *Magn Reson Med*. 2008;60:895-907.
35. Roemer PB, Edelstein WA, Hayes CE, Souza SP, Mueller OM. The NMR phased array. *Magn Reson Med*. 1990;16:192-225.
36. Held P, Dorenbeck U, Seitz J, Fründ R, Albrich H. MRI of the abnormal cervical spinal cord using 2D spoiled gradient echo multiecho sequence (MEDIC) with magnetization transfer saturation pulse: A T2* weighted feasibility study. *J Neuroradiol*. 2003;30:83-90.
37. Fushimi Y, Miki Y, Si U, et al. Gray matter-white matter contrast on spin-echo T1-weighted images at 3 T and 1.5 T: A quantitative comparison study. *Eur Radiol*. 2007;17:2921-2925.
38. Constable RT, Henkelman RM. Contrast, resolution, and detectability in MR imaging. *J Comput Assist Tomogr*. 1991;15:297-303.
39. Hendrick ER. *Breast MRI: Fundamentals and Technical Aspects*. New York: Springer Science and Business Media; 2008.
40. Edelstein WA, Glover GH, Hardy CJ, Redington RW. The intrinsic signal-to-noise ratio in NMR imaging. *Magn Reson Med*. 1986;3:604-618.
41. Brown RW, Cheng YCN, Haacke EM, Thompson MR, Venkatesan R, editors. *Magnetic Resonance Imaging*. Hoboken, NJ: John Wiley & Sons Ltd; 2014.
42. Leener BD, Lévy S, Dupont SM, et al. SCT: Spinal cord toolbox, an open-source software for processing spinal cord MRI data. *NeuroImage*. 2017;145:24-43.
43. Leener BD, Kadoury S, Cohen-Adad J. Robust, accurate and fast automatic segmentation of the spinal cord. *NeuroImage*. 2014;98:528-536.
44. Perone CS, Calabrese E, Cohen-Adad J. Spinal cord gray matter segmentation using deep dilated convolutions. *Sci Rep*. 2018;8, 1–13.
45. Massire A, Rasoanandrianina H, Guye M, Callot V. Anterior fissure, central canal, posterior septum and more: New insights into the cervical spinal cord gray and white matter regional organization using T1 mapping at 7T. *NeuroImage*. 2020;205:116275.
46. Figley CR, Stroman PW. Investigation of human cervical and upper thoracic spinal cord motion: Implications for imaging spinal cord structure and function. *Magn Reson Med*. 2007;58:185-189.
47. Mikulis DJ, Wood ML, Zerdoner OA, Poncelet BP. Oscillatory motion of the normal cervical spinal cord. *Radiology*. 1994;192:117-121.
48. Eschelbach M, Aghaeifar A, Bause J, et al. Comparison of prospective head motion correction with NMR field probes and an optical tracking system. *Magn Reson Med*. 2019;81:719-729.
49. Topfer R, Starewicz P, Lo KM, et al. A 24-channel shim array for the human spinal cord: Design, evaluation, and application. *Magn Reson Med*. 2016;76:1604-1611.
50. Topfer R, Foias A, Stikov N, Cohen-Adad J. Real-time correction of respiration-induced distortions in the human spinal cord using a 24-channel shim array. *Magn Reson Med*. 2018;80:935-946.
51. Germain G, Stockmann J, Topfer R, Wald LL, Stikov N, Cohen-Adad J. Optimization of geometry for combined RF/shim coil arrays for the spinal cord. In Proc. ISMRM; 2016;24:1154.
52. Walter S, Perl R, Notohamiprodjo M, Nikolaou K, Gatidis S. Improvement of EPI-based DWI of the head/neck region using additional local shim coils at 3 Tesla. In Proc. ISMRM; 2019;27:3521.
53. Biber S, Wohlfarth K, Kirsch J, Schmidt A. Design of a local shim coil to improve B0 homogeneity in the cervical spine region. In Proc. ISMRM. 2012;20:2746.
54. Lee G, Jordan C, Tiet P, et al. Improved frequency selective fat suppression in the posterior neck with tissue susceptibility matched pyrolytic graphite foam. *J Magn Reson Imaging*. 2014;41:684-693.
55. Shajan G, Kozlov M, Hoffmann J, Turner R, Scheffler K, Pohmann R. A 16-channel dual-row transmit array in combination with a 31-element receive array for human brain imaging at 9.4 T. *Magn Reson Med*. 2013;71:870-879.
56. Zhang B, Seifert AC, Kim JW, Borrello J, Xu J. 7 Tesla 22-channel wrap-around coil array for cervical spinal cord and brainstem imaging. *Magn Reson Med*. 2016;78:1623-1634.
57. Avdievich NI, Solomakha G, Ruhm L, Scheffler K, Henning A. Evaluation of short folded dipole antennas as receive elements of ultra-high-field human head array. *Magn Reson Med*. 2019;82:811-824.
58. Kraff O, Bitz AK, Kruszona S, et al. An eight-channel phased array RF coil for spine MR imaging at 7 T. *Invest Radiol*. 2009;44:734-740.
59. Marques JP, Kober T, Krueger G, Zwaag W, Moortele PFV, Gruetter R. MP2RAGE, a self bias-field corrected sequence for

improved segmentation and T1-mapping at high field. *NeuroImage*. 2010;49:1271-1281.
60. Weigel M, Bieri O. Spinal cord imaging using averaged magnetization inversion recovery acquisitions. *Magn Reson Med*. 2017;79:1870-1881.

SUPPORTING INFORMATION

Additional supporting information may be found online in the Supporting Information section.

FIGURE S1 Plot of the CNR-values for all of the SC images shown in Figure 5A, from the main document, but without removing the signal dropout in slice 5 from the signal averaging. Each line presents the CNR-values of a certain slice at different TEs and in the MEDIC image

How to cite this article: Geldschläger O, Bosch D, Avdievich NI, Henning A. Ultrahigh-resolution quantitative spinal cord MRI at 9.4T. *Magn Reson Med*. 2021;85:1013–1027. https://doi.org/10.1002/mrm.28455

PUBLICATION 2

Local excitation universal parallel transmit pulses at 9.4T.

Geldschläger O*, Bosch D*, Glaser S, Henning A.

Magnetic Resonance in Medicine. 2021 Jun.

DOI: 10.1002/mrm.28905

* shared first-authorship

Received: 2 April 2021 | Revised: 7 June 2021 | Accepted: 7 June 2021

DOI: 10.1002/mrm.28905

RESEARCH ARTICLE

Magnetic Resonance in Medicine

Local excitation universal parallel transmit pulses at 9.4T

Ole Geldschläger[1] | **Dario Bosch**[1,2] | **Steffen Glaser**[3] | **Anke Henning**[1,4]

[1]High-Field Magnetic Resonance Center, Max Planck Institute for Biological Cybernetics, Tübingen, Germany

[2]Biomedical Magnetic Resonance, University Hospital Tübingen, Tübingen, Germany

[3]Department for Chemistry, Technical University of Munich, Garching, Germany

[4]Advanced Imaging Research Center, University of Texas Southwestern Medical Center, Dallas, Texas, USA

Correspondence
Ole Geldschläger, High-Field Magnetic Resonance Center, Max Planck Institute for Biological Cybernetics, Max-Planck-Ring 11, 72076 Tübingen, Germany.

Email: ole.geldschlaeger@tuebingen.mpg.de

Funding information
This project was co-sponsored by the European Research Council/SYNAPLAST MR/Grant number: 679927, the Deutsche Forschungsgemeinschaft (DFG – German Research Foundation) under the Reinhart Koselleck Programme (DFG SCHE 658/12) and the Cancer Prevention and Research Institute of Texas (CPRIT)/Grant number: RR180056.

Purpose: To demonstrate that the concept of "universal pTx pulses" is applicable to local excitation applications.

Methods: A database of B_0/B_1^+ maps from eight different subjects was acquired at 9.4T. Based on these maps, universal pulses that aim at local excitation of the visual cortex area in the human brain (with a flip angle of 90° or 7°) were calculated. The remaining brain regions should not experience any excitation. The pulses were designed with an extension of the "spatial domain method." A 2D and a 3D target excitation pattern were tested, respectively. The pulse performance was examined on non-database subjects by Bloch simulations and in vivo at 9.4T using a GRE anatomical MRI and a presaturated TurboFLASH B_1^+ mapping sequence.

Results: The calculated universal pulses show excellent performance in simulations and in vivo on subjects that were not contained in the design database. The visual cortex region is excited, while the desired non-excitation areas produce the only minimal signal. In simulations, the pulses with 3D target pattern show a lack of excitation uniformity in the visual cortex region; however, in vivo, this inhomogeneity can be deemed acceptable. A reduced field of view application of the universal pulse design concept was performed successfully.

Conclusions: The proposed design approach creates universal local excitation pulses for a flip angle of 7° and 90°, respectively. Providing universal pTx pulses for local excitation applications prospectively abandons the need for time-consuming subject-specific B_0/B_1^+ mapping and pTx-pulse calculation during the scan session.

KEYWORDS
9.4T, high-field MRI, local excitation, parallel transmit, pTx, reduced FOV, universal pulses

Ole Geldschläger and Dario Bosch contributed equally to this work.

1 | INTRODUCTION

Operating MRI systems with a B_0 field strength of 7T and above (ie, ultra-high field (UHF)), provide higher signal-to-noise ratio, facilitates higher spatial resolutions, and potentially improves diagnostic sensitivity and specificity compared to clinical field strength, such as 1.5T or 3T.[1-3] However, various technical challenges prevent UHF systems from being used routinely in the clinic.[4] The shorter electromagnetic wavelength at UHF, which results in inhomogeneity of the radiofrequency (RF) field,[5,6] can lead to spatially varying flip angles (FAs) and, thus, a spatial variation of the image contrast, signal dropouts or brightening. The most flexible approach to overcome this issue is parallel transmission (pTx).[7] PTx enables much-improved control over the spatial and temporal RF field[8,9] by exploiting the additional degrees of freedom of multiple independent RF transmission channels. Thus, research not only focuses on pulses for homogeneous slice selective[10,11] or whole volume excitation,[12] but also on pulses that produce local excitation[13,14] (LEx, also called inner volume or spatially selective excitation) within the scanned object.

In general, pTx pulse design is based on a set of calibration measurements for each individual subject at the beginning of the scan session/experiment. Subject-specific static magnetic field (B_0) offset and transmit (B_1^+) field distribution maps from each transmit coil need to be acquired before the actual pulse can be calculated. The time needed for B_0 and B_1^+ map acquisition and pulse calculation is usually between 10 and 15 min,[4] while the subject is already positioned in the scanner. Based on these maps, an RF pulse is calculated, which, usually in conjunction with a gradient waveform, excites a desired spatial pattern in the subject's tissue. The computational effort of pulse design increases when RF power limitations have to be taken into account. This whole procedure consumes time that gives no clinical information and is a barrier to clinical uptake of the pTx technique.

Recently, Gras et al[15] introduced the concept of "universal pTx pulses" (UPs). The general idea is to collect a database of B_0 and B_1^+ maps from a representative subject cohort. An RF pulse is designed based on this database and turns out to also perform well on subjects who were not inside the design database. The reliability and benefit of this concept for non-selective and slice selective pulses has been proven for pulses with small and large target FAs as well as their applications in various MRI sequences in the human brain at 7T.[16-19] It has been shown that UPs are virtually immune to inter-site differences.[20] Additionally, a feasibility study for UPs calculated and simulated on B_0/B_1^+ maps acquired at 9.4T,[21] has been presented. In all of these studies, the used transmit k-space trajectories are either "spokes"[22] or "kT-points."[12]

In contrast to existing approaches, the goal of this study is to investigate the concept of UPs for LEx at 9.4T. In our own preliminary work, it was shown in simulations that it is possible to design pulses that can selectively excite the same 2D[23] or 3D target pattern[24] at 9.4T, as well as at 7T,[25] across multiple subjects. The transmit k-space trajectories in these studies, as well as in the current work, are "spiral" k-space trajectories, which is another difference compared to previous UP studies. The advantages of spirals for LEx were already discussed.[26]

In general, LEx can be used for reduced (or zoomed) field of view (FOV) applications. It allows to reduce the FOV in phase-encoding direction by masking the tissues outside the FOV, which would otherwise fold into the image.[27] Consequently, LEx can reduce the total signal acquisition time and/or increase the spatial resolution which is important for a range of clinical brain and body applications.[28] Furthermore Lex can reduce the distortion in EPI readouts in functional and diffusion-weighted MRI,[29] due to the reduced FOV, especially because the decreased number of points in the readout direction allows shorter inter-echo spacing. LEx pulses were applied within various imaging sequences such as the gradient-echo (GRE) in rats[13] or the fast-spin-echo sequence in the human brain,[30] as well as for diffusion-weighted imaging in human prostate[31] and pancreas.[32] Moreover, LEx has been exploited for MR spectroscopy in the human brain at 3T[33] and 7T[34] to define shaped voxels.

In this work, we demonstrate the feasibility of the combination of LEx and UPs by local excitation of the visual cortex in the human brain with excellent suppression of the remaining brain areas as proof of principle. For that purpose, we collected a database of B_0 and B_1^+ maps from eight different subjects. We designed pulses that aim to excite a predefined 2D or 3D target excitation pattern (target FA of 90°, FA90), on the database heads. Afterward, the performance of these pulses was tested in simulations and in vivo at 9.4T. In order to show the potential of UPs for LEx, a GRE sequence with a reduced FOV was applied.

2 | METHODS

2.1 | UP calculation

To design UPs that produce the same excitation pattern on different heads, the "spatial domain method"[35] from Grissom et al. was applied. Its basic idea is to exploit the linearity of the Bloch equations for small tip angle regimes. Using the small tip angle approximation (STA), Pauly et al[26] derived that the Bloch equation can be approximated by a Fourier integral of any desired (and realizable) excitation k-space trajectory,[36] $\boldsymbol{k}(t)$, weighted by a complex RF pulse $p(t)$, and spatially weighted by the transmit coils complex transmit sensitivity $s(\boldsymbol{x})$:

$$m(\boldsymbol{x}) = i\gamma m_0 s(\boldsymbol{x}) \int_0^T p(t)\, e^{i\gamma \Delta B_0(\boldsymbol{x})(t-T)} e^{i\boldsymbol{x}\boldsymbol{k}(t)} dt, \qquad (1)$$

with $m(\boldsymbol{x})$ is the magnetization in voxel $\boldsymbol{x}$, γ is the gyromagnetic ratio, m_0 is the equilibrium magnetization magnitude, T is the pulse length, and $\Delta B_0(\boldsymbol{x})$ denotes the field map.

To form an aggregate excitation pattern the single excitation patterns $s_r(\boldsymbol{x})$ from the R transmit coils can be spatially superposed:

$$m(\boldsymbol{x}) = i\gamma m_0 \sum_{r=1}^{R} s_r(\boldsymbol{x}) \int_0^T p_r(t)\, e^{i\gamma \Delta B_0(\boldsymbol{x})(t-T)} e^{i\boldsymbol{x}\boldsymbol{k}(t)} dt. \quad (2)$$

Analogously to Yip et al,[37] discretizing time to N_t samples and space to N_s voxels yields the following matrix-vector multiplication

$$\boldsymbol{m} = \sum_{r=1}^{R} \boldsymbol{S}_r \boldsymbol{A} \boldsymbol{p}_r = \left[\boldsymbol{S}_1\boldsymbol{A} \cdots \boldsymbol{S}_R\boldsymbol{A}\right] \begin{bmatrix} \boldsymbol{p}_1 \\ \vdots \\ \boldsymbol{p}_R \end{bmatrix} = \boldsymbol{A}_{full}\boldsymbol{p}_{full}, \quad (3)$$

with $\boldsymbol{m}$ is the length-N_S vector of the magnetization from each voxel $\boldsymbol{x}$ and $\boldsymbol{S}_r = diag\left\{s_r\left(\boldsymbol{x}_i\right)\right\}$ is a diagonal matrix containing the sensitivity pattern of transmit coil r. The (i,j)-th element of the $N_S \times N_T$ system matrix $\boldsymbol{A}$ is given by:

$$a_{ij} = i\gamma m_0 \Delta t e^{i\gamma \Delta B_0(x_i)(t_j - T)} e^{ix_i k(t_j)}. \quad (4)$$

$\boldsymbol{A}_{full}$ is a vertical concatenation of the matrices $\boldsymbol{S}_r\boldsymbol{A}$ and $\boldsymbol{p}_{full}$ is a horizontal concatenation of the length-N_T vectors $\boldsymbol{p}_r$ of RF-pulse samples from coil r.

By defining a target excitation pattern $\boldsymbol{m}_{tar}$ we obtain the optimization problem

$$\boldsymbol{p}_{TP}^* = \underset{\boldsymbol{p}}{\operatorname{argmin}} \left\{ \left\| \boldsymbol{A}_{full}\boldsymbol{p}_{full} - \boldsymbol{m}_{tar} \right\|^2 \right\} \quad (5)$$

By minimizing this problem in Equation (5), we design the RF pulse p_{TP}^* that aims to excite the desired target pattern on one specific head (ie, the tailored pulse [TP]).

While the original "spatial domain method" was intended for designing pulses tailored to one specific subject, we extend this method herein in order to create a pulse p_{UP}^* that excites the same target pattern on multiple heads (ie, the UP):

$$\boldsymbol{p}_{UP}^* = \underset{\boldsymbol{p}}{\operatorname{argmin}} \left\{ \left\| \begin{bmatrix} \boldsymbol{A}_{full,1} \\ \vdots \\ \boldsymbol{A}_{full,N_{DB}} \end{bmatrix} \boldsymbol{p} - \begin{bmatrix} \boldsymbol{m}_{tar} \\ \vdots \\ \boldsymbol{m}_{tar} \end{bmatrix} \right\|^2 \right\}, \quad (6)$$

where $A_{full,j}$, with $j = 1, \ldots, N_{DB}$, is the full system information matrix of subject j and N_{DB} is the size of the design database, ie, the number of subject heads based on which the pulse will be designed. By minimizing Equations (5) or (6) all voxels are weighted equally, ie, no specific weighting function was applied.

The optimization problem in Equation 6 was solved by performing two steps. First, the least-squares method implemented in the *lsqr*-function[38] from MATLAB (MathWorks, Natick, MA) was applied, which solves a system of linear equations. The optimization was stopped after 20 iterations, which was empirically found as a compromise between performance and compute time. Applying higher iteration numbers led to drastically increased pulse voltages with only minor performance improvements, and no regularization term for voltage was applied. Notably, with the least-squares method, it is not possible to exclude the phase of the resulting excitation from the optimization, however, the profiles phase was of no interest during this study. For that reason, in the second step of the UP calculation, the *lsqr* result was used as an initial guess for the *active-set* algorithm implemented in MATLAB's *fmincon*-function. The cost function used for this optimization is presented in Equation (6), ie, only the magnitude of the profiles are considered. Analogously to the literature,[15,16,18,21] the *active-set* algorithm was chosen because of its speed and robustness.[39,40] By means of the *active-set* algorithm, the solution was constrained to a maximum pulse amplitude of 130 Volt at plug level (hardware limit). The optimization was stopped if the improvement of the cost-function values was negligible during 30 consecutive iterations.

Although this approach was introduced for designing small tip angle pulses, it also "holds well at tip angles of 90°."[26,35,41] For that reason, we designed two different UPs with FA90. The first UP (UP2D) aimed to excite the visual cortex region in the central transversal slice of a head (by means of a 2D target pattern, Figure 1A)) with FA90. The remaining areas within the target slice should not be excited. The UP2D pulse is non-slice-selective and has a fixed duration of 7.96 ms using a 2D spiral-in k-space trajectory (max. amplitude: 23 mT/m, max. slew rate: 150 T/m/s, Figure 1A). That pulse length was chosen as a compromise between sufficient degrees of freedom for the optimization and application possibilities for pulses of that length. Tissue outside of the target slice was not taken into account for designing UP2D. Since UP2D is non-slice selective, a 3D sequence was used for performance evaluation, with frequency encoding along the head-foot direction (see "UP versus TP performance evaluation" section).

Analogously, UP3D aimed to excite the visual cortex area as well with FA90, but by means of a 3D target pattern (Figure 1B) and based on a 3D stack-of-spiral-in trajectory[42,43] (max. amplitude: 7.4 mT/m, max. slew rate: 150 T/m/s, six spirals, Figure 1B). The pulse duration was 8.18 ms. For both pulses and gradient shapes, the dwell time was 10 μs. The scanner inherent gradient delay of 4 μs was taken into account in the

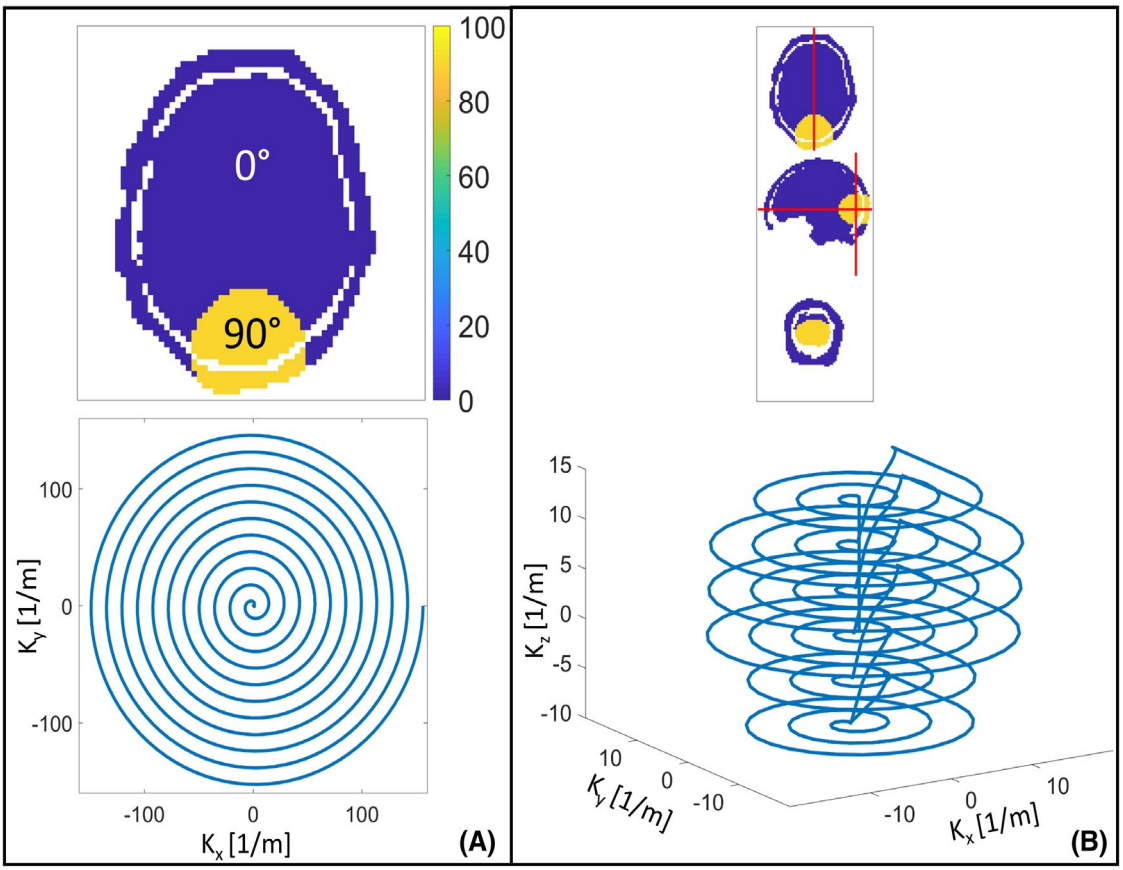

FIGURE 1 A, The upper picture displays the 2D target pattern with the desired FAs in the excitation and non-excitation areas. The image below shows the spiral-in k-space trajectory based on which the 2D target pattern pulse is designed. B, The upper picture displays the 3D target pattern (same desired FAs and colorbar as in A), with red lines marking the position of the respective sagittal, coronal and transversal slice depicted. The image below shows the stack of spiral-ins k-space trajectory based on which the 3D target pattern pulses are designed

pulse files. For UP3D (FA90), the deviations between the STA forecasts and the results from the Bloch simulations were compared.

In order to create not only UPs for large tip angles, but also for small tip angles, the calculated UPs for FA90, were scaled down proportionally in order to create UPs with a desired FA of 7° (FA7). We also tested UP calculations directly with a target FA of 7°, but since these pulses did not considerably outperform the downscaled UPs (on the non-database heads, see Supporting Information Figure S1, which is available online, for 2D- and Supporting Information Figure S2 for 3D results), we maintained the downscaled approach.

To create a representative design database for the calculation of the UPs, B_0 and eight single-channel B_1^+ maps were acquired from the heads of eleven different subjects at 9.4T. Eight of the eleven datasets were used for UP design and three for performance evaluation in simulations. These numbers were based on a 7T simulation study[25] in which it was shown that database size of five different heads theoretically is sufficient to design reliable LEx UPs. To increase reliability and since herein the field strength is higher, we wanted to be more conservative and added three more heads to the design database.

To calculate UP2D, the B_0/B_1^+ map information and the resulting excitation pattern from only the central slice of each head were taken into account. After application of the masking routine, each of the eight central slices consisted of between 1942 and 2208 voxels, which resulted in a total of 16533 voxels for all eight heads. For the design of UP3D, the information from the entire heads was employed (57028 to 65801 voxels per head, 487734 voxels for all eight heads).

Both optimization problems were solved on a high-performance-compute system node equipped with an Intel "Haswell" Xeon E5-2698 processor (128 GB RAM, 32 cores with 2.3 GHz each).

The design of UP2D was done using parallel computing on the 32 cores. However, for calculating UP3D, parallel computing was not applied because of RAM limitations.

During this study, the subject-specific TPs were calculated as a reference by solving the optimization problem in Equation (5) with MATLABs *lsqr*-function. As mentioned before, the *lsqr*-function does not allow to exclude the excitation phase from the optimization. However, only *lsqr* was used for TP design, due to time limitations for online pulse design (20 iterations ~ 0.7 (19) seconds for 2D (3D)). It should be noted that the TPs for FA7 were not downscaled FA90 pulses, but directly designed with a target FA of 7°. In case the maximum pulse amplitude exceeded the limit of 130

V, the TPs were constrained by applying the optimal control based pulse-design method GRAPE.[44,45]

2.2 | UP versus TP performance evaluation

Bloch equations were used to simulate the magnetization profiles of each RF pulse (using the corresponding B_0/B_1^+ maps of the heads). For simplicity, relaxation effects during the RF pulse dynamics were ignored but could be incorporated with knowledge of T1/T2 maps. The magnetization profiles were converted to FA profiles afterward. For each FA profile the normalized root mean square error (NRMSE) between the profile and the target excitation FA pattern, respectively, was determined, in order to evaluate the overall performance of a pulse. Additionally, the mean FA in the target excitation and non-excitation areas, respectively, were calculated for each profile to also verify the background suppression performance.

Before the application of TPs and UPs at the scanner, both, global SAR and maximum local SAR for each pulse were calculated using the VOP method.[46] None of the pulses calculated during this study exceeded any of the SAR regulation limits. However, SAR constraints were not incorporated in the pulse design algorithm.

To test the pulses in vivo at 9.4T, all FA7 pulses (ie, UP2D/UP3D and the corresponding TPs for FA7) were applied on three non-database subjects in a T2*-weighted 3D short repetition time (TR) GRE-sequence (voxel size: $0.8 \times 0.8 \times 0.8$ mm^3, matrix size: 224 (left to right) × 280 (anterior to posterior) × 280 (head to feet), 3D encoding direction: left to right, phase-encoding direction: anterior to posterior, frequency encoding direction: head to feet, TR = 18 ms, echo time (TE) = 8 ms, bandwidth (BW) = 260 Hz/px, GRAPPA[47] 2 × 2. To further prove the performance of the pulses, UP3D for FA7 was applied in a GRE-sequence with a reduced FOV (voxel size: $0.4 \times 0.4 \times 0.4$ mm^3, matrix size: $224 \times 162 \times 200$, TR = 18 ms, TE = 8 ms) on one non-database subject.

All FA90 pulses (ie, UP2D/UP3D and the corresponding TPs for FA90) were applied on three non-database subjects with a sequence analog to the one used for acquisition of the B_0/B_1^+ maps (see "Volunteer scans" section). For that purpose, the FA90 pulses were used as preparation pulse in the TurboFLASH sequence,[48] in order to create their FA maps. Applying FA90 pulses to the short TR GRE-sequence was not possible due to conservative SAR constraints, which lead to long TRs and, thus, unrealistic scan times.

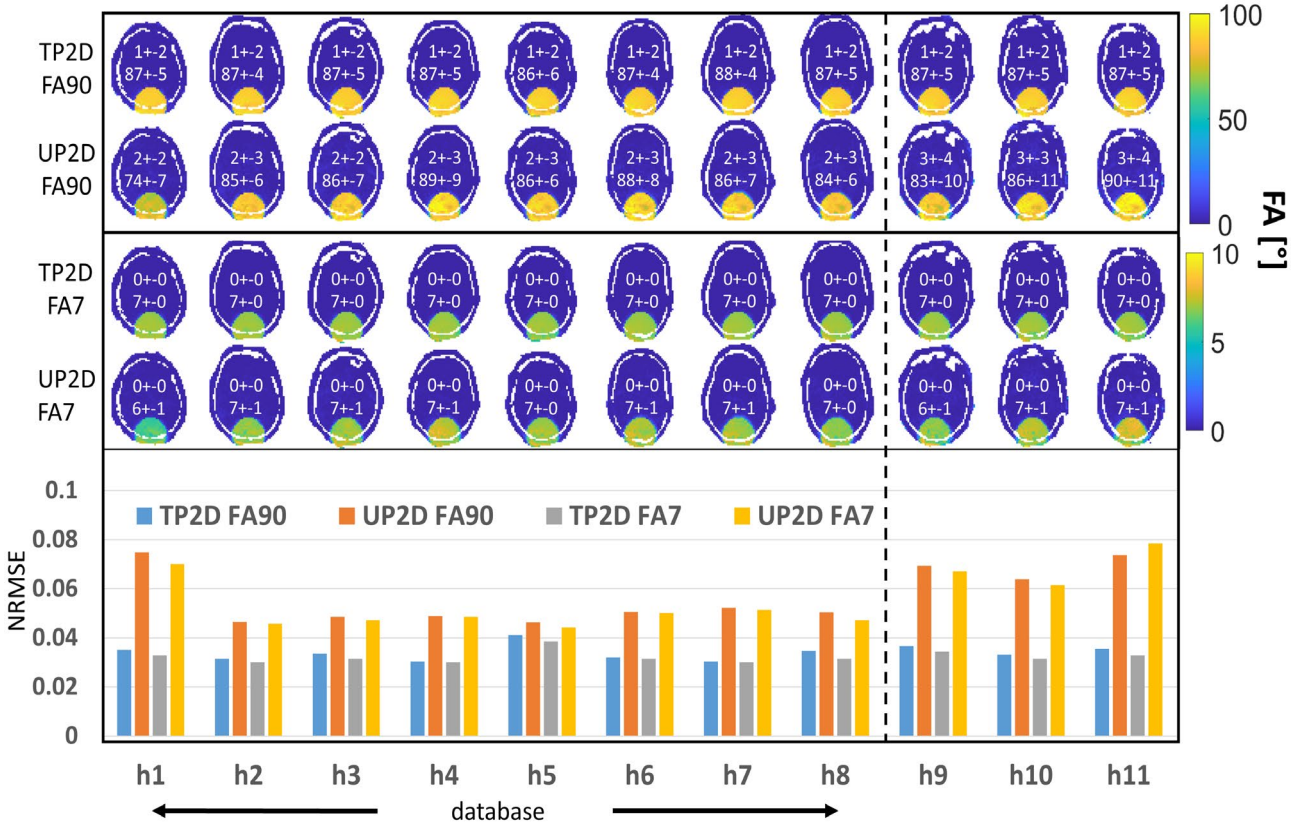

FIGURE 2 Bloch simulated FA profiles of the TPs for FA90 (first row of profiles), UP2D for FA90 (second row of profiles), the TPs for FA7 (third row), and UP2D for FA7 (fourth row). The eight columns on the left present the database heads. The three columns on the right present the non-database heads. The upper numbers within each profile depict the mean FA and the corresponding SD in the non-excitation region. The lower numbers within each profile depict the mean FA and the corresponding SD in the excitation region. The bar plot below the profiles illustrates the NRMSEs between the target pattern and resulting profile for each pulse and head

2.3 | Volunteer scans

All measurements were performed on a 9.4T whole-body MR scanner (Siemens Healthcare, Erlangen, Germany) equipped with an SC72 whole-body gradient system, with a maximum amplitude and slew rate of 40 mT/m and 200 mT/m/ms, respectively. An in-house-built 16 channel tight-fit array coil,[49] consisting of eight transceiver surface loops and eight additional receive-only loops was used. All experiments were performed with the approval of the local Ethics Committee. Informed signed consent was obtained from each volunteer, before each MR experiment.

A 3D presaturated TurboFLASH (satTFL) sequence was used for interferometric individual-channel B_1^+ mapping[48] (TR = 2.44 ms, TE = 0.75 ms, BW = 700 Hz/Px, asymmetric echo, elliptical k-space acquisition, GRAPPA 2 × 2, recovery time between acquisitions = 7.5 s, nominal FA saturation = 60°, FA readout = 4°). An additional scan with 500 µs prolonged TE was used to calculate B_0 maps, from the phase evolution between the two different echo times. All maps were recorded with 3.5 mm isotropic spatial resolution and a matrix size of 64 × 64 × 64. Note that, as most FA mapping methods, this sequence allows for measuring accurate FA maps within the range of ~30-150°.[50] The acquired B_0/B_1^+ maps of each database head (central transversal slice) is visible in Supporting Information Figure S3.

To guarantee that all heads were positioned highly analogous relative to the coil and the isocenter of the scanner, the top of each head was aligned to a marker inside the coil. Furthermore, all scans were executed with the same pad underneath the head. Scanning was performed in the head-first supine position.

Based on a reference image of the B_1^+ mapping data, tissue masks were created using a neural network implemented in MATLAB, which was trained on five manually segmented datasets. The major purpose for creating these tissue masks was to exclude the voxels in the skull bone positions, for which contribution to the signal is negligibly low. Here, the B_0 maps change rapidly, which makes pulse design particularly difficult in those regions. Since these voxels do produce almost no signal in the MR acquisition, they can be neglected in the pulse design. It should be noted that only the skull bone voxels were masked out, not the subcutaneous fatty tissue voxels (Figure 1).

3 | RESULTS

3.1 | UP2D – 2D target pattern

After 716 iterations of the *active-set* algorithm, the optimization was stopped because the cost-function values did not decrease further. The average duration of one iteration was 3.5 min. The resulted UP2D for FA90 applied within the TFL sequence produces a maximum local specific energy dose (SED) of 2.65 J/kg. Herein, SAR is not a meaningful measure, as the pulse is played out only once in the TFL sequence. UP2D for FA7 produces a maximum local SED of 0.02 J/kg, a maximum local SAR of 0.89 W/kg, and a global SAR of 0.07 W/kg within the GRE sequence (TR = 18 ms).

Figure 2 shows simulated FA profiles of the eight databases and three non-database heads. For both FA90 and FA7, the profiles resulting from the TPs and from UP2D are very similar. The respective TPs deliver only a slightly better performance compared to the UP2D performance. The mean FAs for the TPs and UP2D are highly similar, while the SD is slightly higher for most UP2D profiles. For non-database heads, the NRMSE values of UP2D are increased compared to database heads, but the resulting profiles are still highly similar to the TP profiles. For non-database heads, UP2D

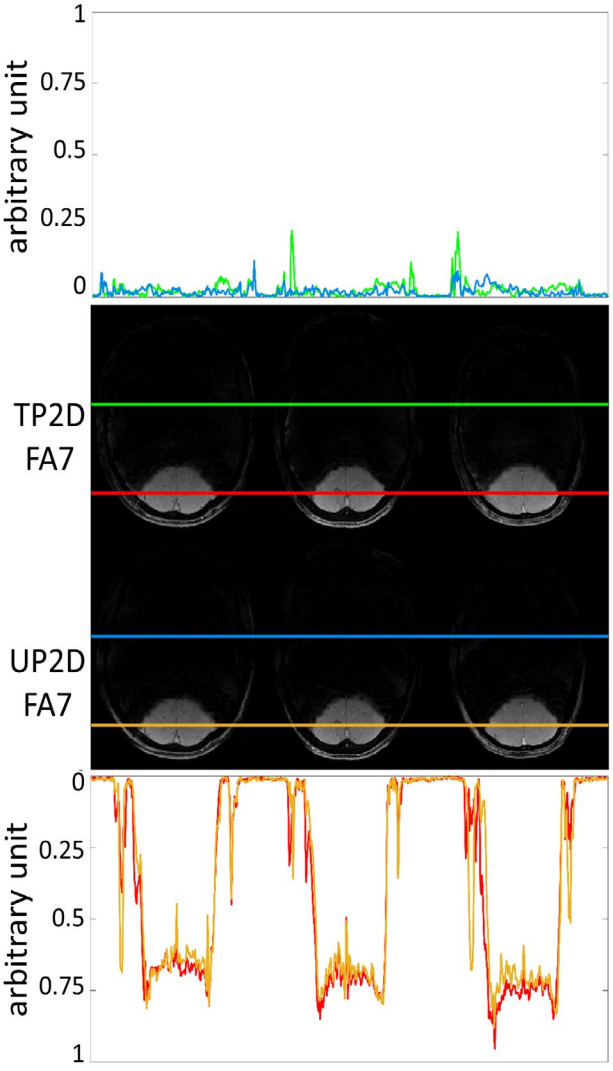

FIGURE 3 The central box shows in vivo GRE images (central transversal slice, respectively) from the three non-database heads. Both the respective TPs and UP2D for FA7 were applied on each head. The line charts above and below the GRE box show the normalized signal strengths in arbitrary units in the respective voxels in the GRE images (marked by the colored lines in the images)

performs with a mean NRMSE of 0.069 ± 0.005 for FA90 and 0.069 ± 0.009 for FA7. The mean TP performance for these heads is 0.035 ± 0.002 for FA90 and 0.033 ± 0.001 for FA7. Notably, without optimizing UP2D with the *active-set* algorithm, the mean NRMSE on non-database heads would have been 0.087 ± 0.008 for FA90 and 0.087 ± 0.009 for FA7.

Figure 3 presents images recorded with a GRE sequence at 9.4T applying UP2D for FA7 and the respective TPs, for the three non-database heads. The image quality in the target excitation region and the background suppression resulting from the TPs and UP2D are very similar. Confirming the simulation results from Figure 2, it is visible that the areas where no excitation is desired, contribute very little signal. The visual cortex area is excited almost exclusively. The TPs outperform UP2D at the subcutaneous fatty tissue regions.

By applying UP2D with FA90 and the respective TPs in the satTFL sequence (for three non-database heads), we obtain the FA maps visible in Figure 4. Again, the performance of UP2D and the TPs is similar. Excitation occurs mainly in the visual cortex area; however, there is some lack of FA homogeneity within that region. While the TPs performance is close to the desired FA90, the UP2D causes a slightly too high FA in some of the excited voxels. In the remaining areas, the shown FAs are below 30° for most voxels. As mentioned before, for observed FAs of below 30° the satTFL-sequence results are not reliable[50] (ie, the observed FAs of approximately 20° on the green and blue profile line in Figure 4 are most likely not the actual FAs). Supporting Information Figure S5 shows the mean FAs in the target excitation and non-excitation areas, respectively.

3.2 | UP3D – 3D target pattern

Each iteration of the *active-set* optimization for UP3D took 2:19 h:min on average. The algorithm was stopped after 175 iterations, as the further improvement was expected to be negligible. The resulted UP3D for FA90 applied within the TFL sequence produces a maximum local SED

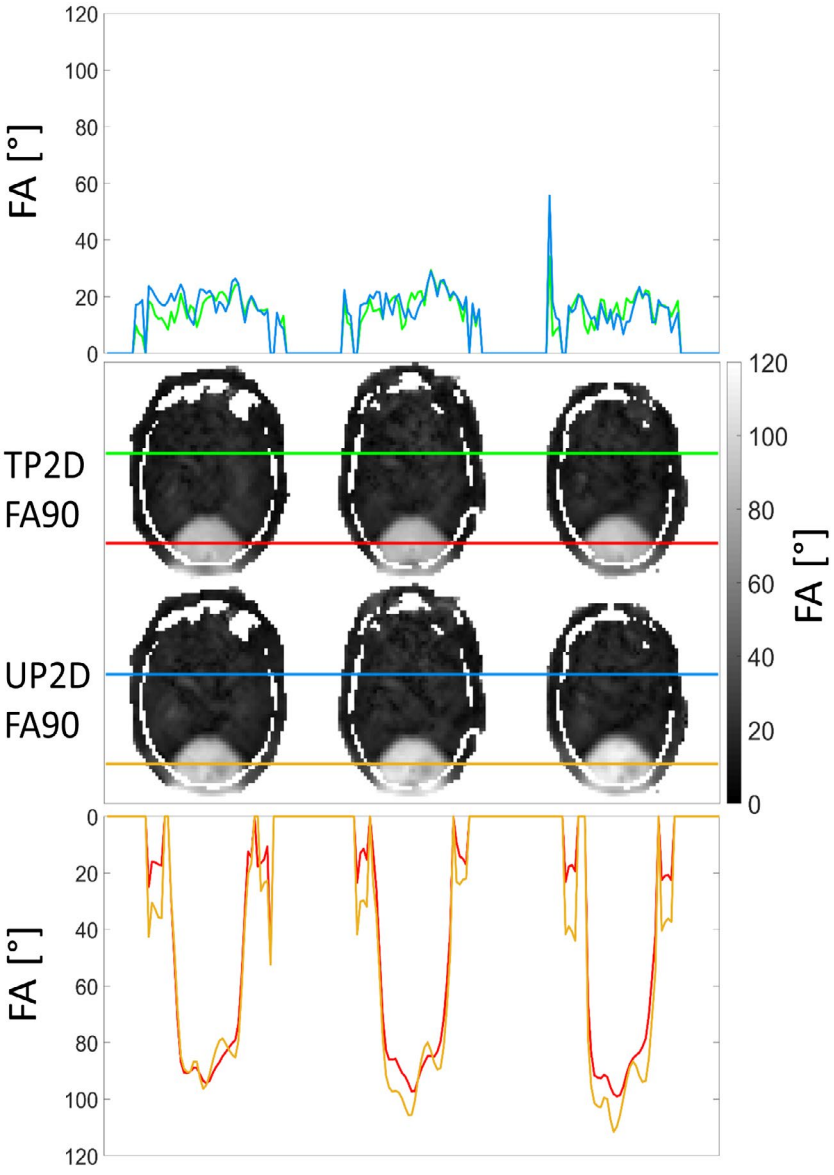

FIGURE 4 The central box of images shows FA profiles (central transversal slice, respectively) acquired in vivo with the satTFL B_1^+ mapping sequence from the three non-database heads. Both the respective TPs and UP2D for FA90 were applied on each head The line charts above and below the FA profiles, show the FAs in the respective voxels in the FA profiles (marked by the colored lines in the images)

of 0.65 J/kg. UP3D for FA7 produces a maximum local SED of 0.004 J/kg, a maximum local SAR of 0.22 W/kg, and a global SAR of 0.016 W/kg within the GRE sequence (TR = 18 ms).

Figure 5 displays the simulation results for the pulses with a 3D target pattern. Due to space limitations in the figure, only the FA profiles from three representative database subjects and three non-database subjects are depicted. Comparing the pulse performances, both UP3D and the TPs have some lack of homogeneity in the excited areas and achieve a mean FA below the desired 90° or 7°. In the center of the target excitation area, the FA is generally higher compared to the peripheral regions of the excited areas. On the non-database heads, UP3D for FA90 (FA7) creates a mean FA in the target excited areas of ~70° (~6°), while the corresponding TPs for FA90 (FA7) on the non-database heads only achieve a mean FA of ~49° (~4°). The FA SD is in general slightly higher for UP3D, compared to the TPs (Supporting Information Figure S4 depicts the mean FAs and SD in the excited/non-excited areas, respectively). Notably, the TPs for FA7 are not downscaled from the TPs for FA90, but directly designed with a target FA of 7°. Furthermore, UP3D outperforms the corresponding TPs in the overall performance which is visible observing the NRMSE values: For most database and non-database heads (FA90 and FA7) the NRMSEs from UP3D are lower than the NRMSEs from the TPs. For non-database heads, UP3D performs with a mean NRMSE of 0.114 ± 0.007 for FA90 and 0.115 ± 0.009 for FA7. The mean TP performance for those heads is 0.129 ± 0.004 for FA90 and 0.128 ± 0.004 for FA7. Without optimizing UP3D with the *active-set* algorithm, the mean NRMSE on non-database heads would have been 0.133 ± 0.004 for FA90 and 0.133 ± 0.005 for FA7. In general, the NRMSEs are higher, compared to the NRMSEs for the 2D target pattern (Figure).

Figure 6B compares the NRMSE values between the STA forecast and the Bloch simulation for UP3D (FA90) for the eight database heads, respectively. The biggest NRMSE difference is visible for h1 (0.0026). In the example FA profiles in Figure 6A, differences between the STA and the Bloch profile are barely visible. A lack of excitation uniformity in the excitation area occurs in both profiles. In the voxel-wise difference map of STA profile and Bloch profile, discrepancies

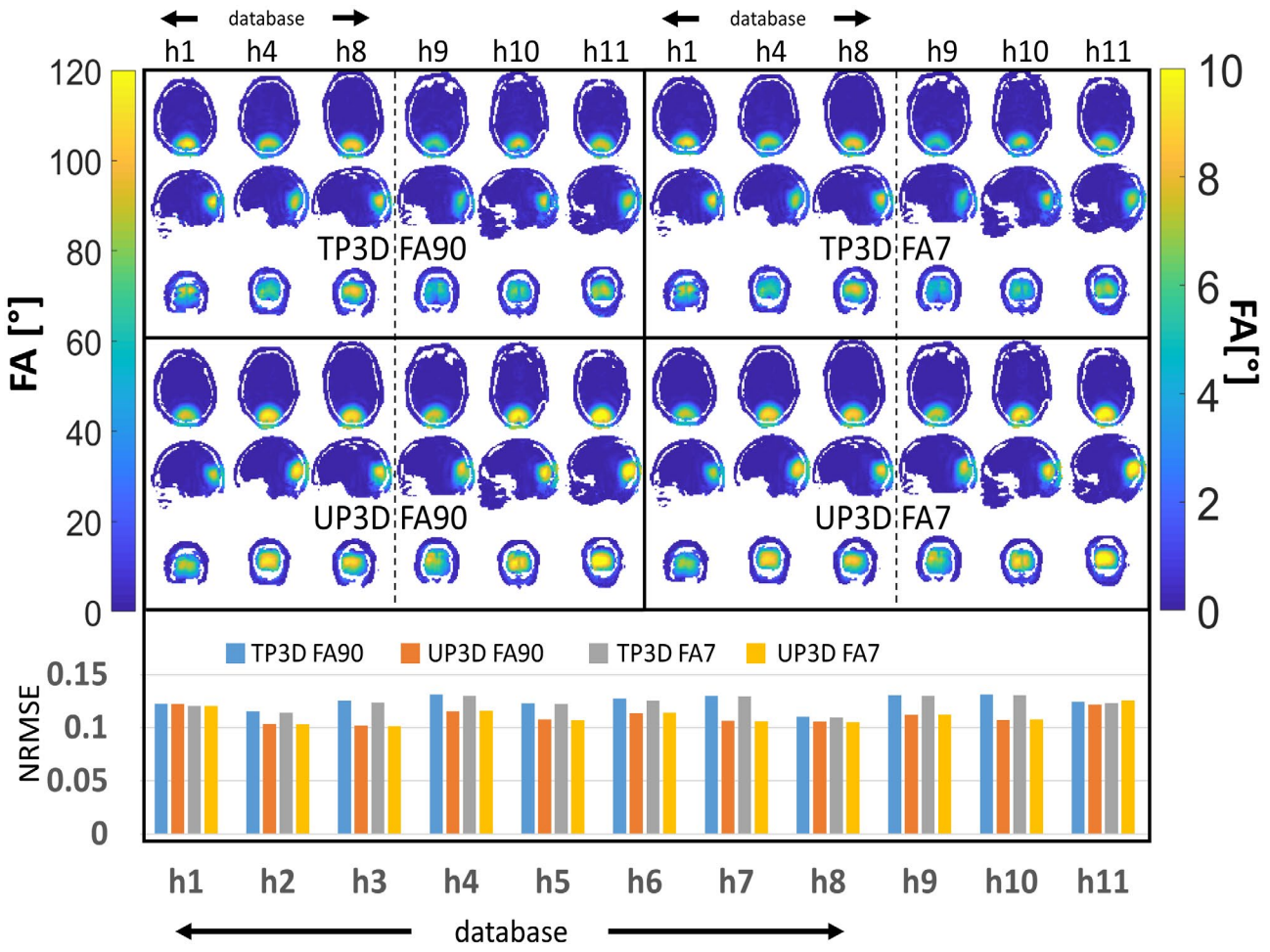

FIGURE 5 Bloch simulated FA profiles of the TPs for FA90 (upper left sector), UP3D for FA90 (lower left sector), the TPs for FA7 (upper right sector), and UP2D for FA7 (lower right sector). Depicted are just three database heads (h1, h4, h8) and the three non-database heads (h9, h10, h11). For each head, a transversal, a sagittal, and a coronal slice are depicted (see Figure 1B for the slice positioning). The different colormaps for the FA90 and FA7 profiles are worth noting. The bar plot below the profiles illustrates the NRMSEs between the target pattern and resulting profile for each pulse and head

of a maximum of 12° mainly in the excited area are observable. In the non-excited area, there are almost no differences between STA and Bloch profile. For the remaining database heads, the results are similar to the shown representative example h6.

Figure 7 depicts in vivo GRE imaging results of UP3D and the corresponding TPs for FA7 (for the three non-database subjects). On all three comparisons, UP3D and the TPs perform similarly well. UP3D delivers a slightly higher signal in the visual cortex area compared to the TPs, while there is very little signal in the remaining areas for both pulses.

In Figure 8, in vivo FA maps acquired with the satTFL B_1^+ mapping sequence by applying UP3D and the respective TPs for FA90, are shown. The FAs resulting from the TPs are mostly below the desired FA90. UP3D outperforms the TPs as the FA in the excited areas is in general closer to 90° (see Supporting Information Figure S5 for the mean FAs in the target excitation and non-excitation areas, respectively).

In order to further demonstrate the performance of UP3D, GRE images with a reduced FOV compared to the FOVs from Figures 3 and 7, were acquired (Figure 9). Since the two phase-encoding directions were anterior to posterior and left to right, folding artifacts would have occurred, if the signal from outside the FOV were not suppressed sufficiently. In fact, folding artifacts are negligible.

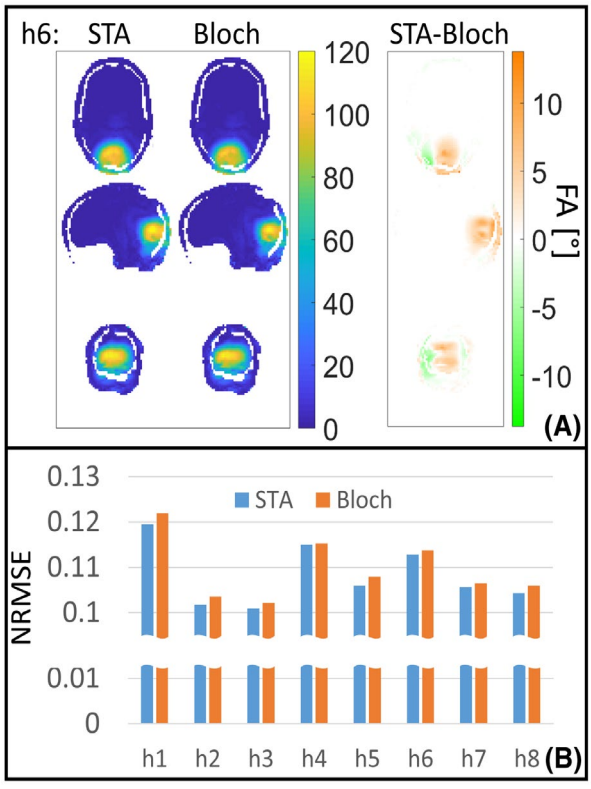

FIGURE 6 A, Left: Comparison between the STA and the Bloch simulated FA profile for UP3D (FA90) on head 6 (a database head). Right: Voxel-wise difference between the STA and the Bloch simulated FA profiles. B, Bar plot illustrating the NRMSEs between target pattern and the STA or Bloch simulation for UP3D on the database heads

4 | DISCUSSION

This work demonstrated that the concept of UPs is applicable for LEx. For a 2D and a 3D target pattern, UPs based on eight database heads were designed. The UPs delivered a good performance in simulations and in vivo on database heads and non-database heads for small and large FAs.

The pulses in this study were designed by means of an extension of the "spatial domain method."[35] This approach is based on the small-tip-angle approximation[26] of the Bloch equations. Nevertheless, it was also possible to design large FA LEx pulses with this method. However, when simulated with full Bloch equations it is revealed that the pulse performance is slightly lower than predicted by the STA method. Figure 6 shows that this decrease is minor for LEx patterns with a relatively small excited area. In the non-excited area, there are almost no differences between STA and Bloch profile, which was expected since this is inside the small-tip-angle regime. Performing pulse optimization exploiting full Bloch simulation in the *active-set* algorithm, was not feasible during this study, as replacing the matrix multiplication by full Bloch simulations would lead to immensely increased optimization time for a database of eight heads and a pulse length of 8 ms (for 3D target patterns, ~22 h per iteration).

Despite the slight difference between the STA profile and Bloch profile, the introduced method produced UPs with excellent performance. For the 2D target pattern, the respective TPs perform just slightly better than UP2D (Figure 2) on non-database heads. The mean NRMSE difference between TPs and UP2D is 0.034 ± 0.004 for FA90 and 0.036 ± 0.008 for FA7. The simulated FA profiles are very similar. That is confirmed in the in vivo measurement results (Figures 3 and 4), where TP and UP2D acquisitions are akin. Both have very low excitation in the desired non-excitation areas and good excitation in the visual cortex area. However, in the satTFL FA profiles (Figure 4) UP2D exceeded the desired 90° in some voxels, which explains the higher NRMSEs for UP2D compared to the TPs. In the GRE results in Figure 3, UP2D delivers a slight unwanted excitation of the subcutaneous fatty tissue next to the visual cortex area. A possible reason why this is not visible in simulations (Figure 2) could be inaccuracies in the B_0 field measurements of these tissues or nonlinearities in the gradient system of the scanner.

The simulated FA profiles resulting from UP3D and the respective TPs are similar as well (Figure 5). Interestingly, UP3D performs slightly better than the respective TPs. The mean NRMSE difference between TPs and UP3D on non-database heads is 0.015 ± 0.011 for FA90 and 0.013 ± 0.013 for FA7. That is most likely due to the fact that UP3D was

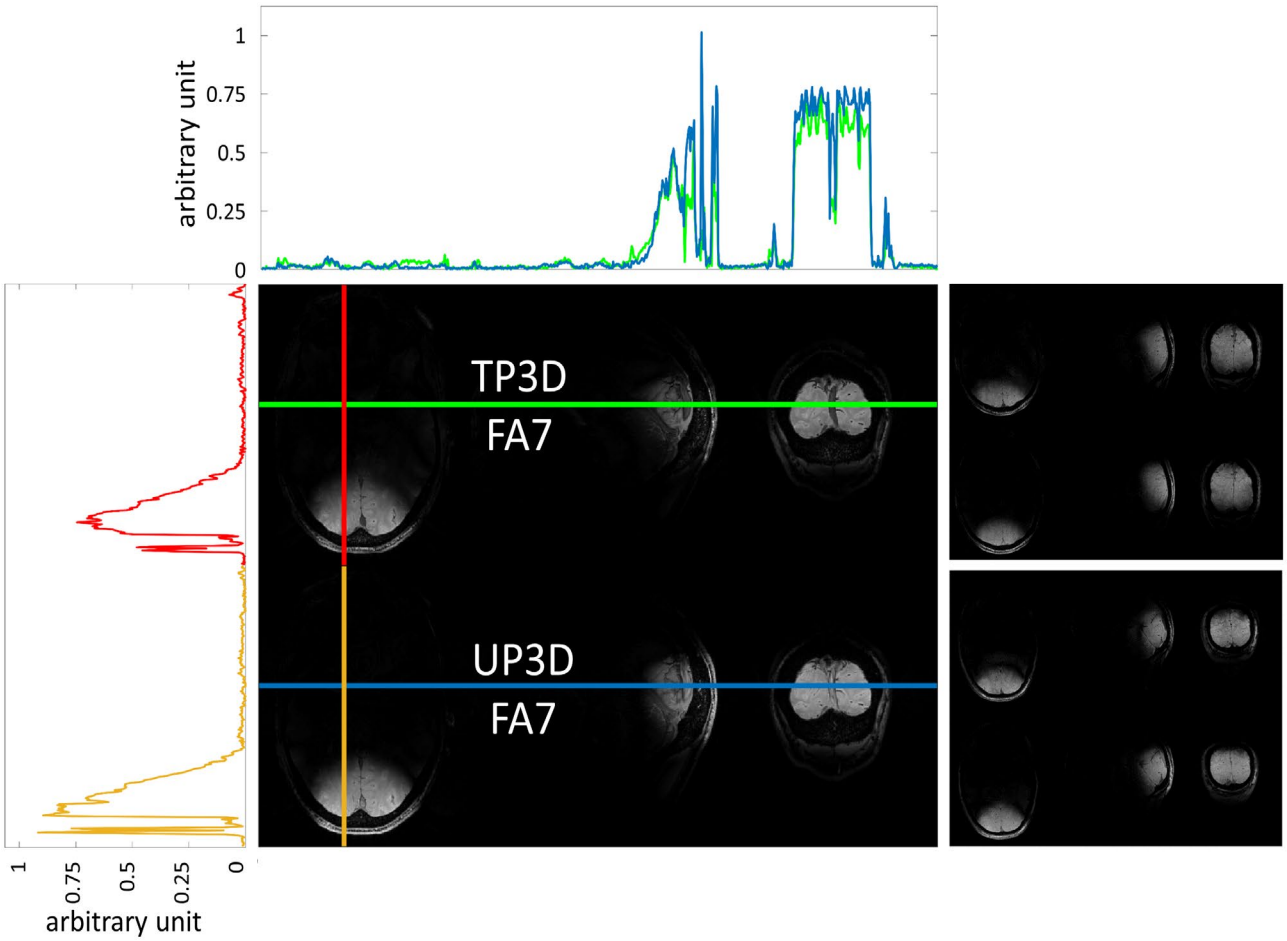

FIGURE 7 The central box and the two boxes on the right-hand side show in vivo GRE images (represented by three slices respectively, slice positioning according to Figure 1B) from the three non-database heads. Both the respective TPs and UP3D for FA7 were applied to each head. The line charts left and above the central box show the normalized signal strengths in arbitrary units in the respective voxels in the GRE images of the central box (marked by the colored lines in the images)

calculated without incorporating the excitation phase in the optimization, while it was included for the TP calculations. For that reason (and for the non-existing compute time limitations, theoretically) UP3D produces better results, although the optimization takes eight complete heads at the same time into account. The Supporting Information Figure S6 presents simulated 3D profiles for TPs that were calculated with the magnitude least-squares optimization[51] in order to exclude the phase from the calculation. As the computation time for this approach (~ 6:48 min:sec for a 3D TP) was considerably higher compared to the solely least-squares approach, the resulted pulses were not measured in vivo in this study.

In vivo (Figures 7 and 8), the performance of the corresponding TPs and UP3D (FA7 and FA90), again, is similar. Analog to the 2D results (Figure 3) it is visible for FA7 that the excitation in the target non-excitation areas is very low. Since the satTFL-sequence results (Figures 4 and 8) are not reliable for FAs of below 30°[50] and since the simulations (Figures 2 and 5) and the GRE results for FA7 (Figures 3 and 7) show a very low excitation in the target non-excitation areas, it leads to the assumption that this is also true for the UP2D- and UP3D-FA90 in vivo results.

The FAs in the visual cortex resulting from the TP in Figure 8 are mostly below the desired FA90, while UP3D is in general closer to FA90. The deviation in terms of excitation uniformity in the excitation area which is visible in FA profiles in simulations (Figure 5) and in the satTFL acquisitions (Figure 8) for TPs and UP3D can be deemed acceptable as the GRE sequence (Figure 7) as well as "most neuroimaging applications exhibit some resilience against moderate FA variations."[21] It should be noted, that this offset in the simulations is not a result of the slight discrepancy between STA forecast and Bloch simulation. Both profiles exhibit this offset problem, as visible in Figures 5 and 6A. For the 2D results (Figure 2), this offset is very small, as the optimization problem is not as difficult as for the 3D case. For the same reason, the 2D TPs were still outperforming UP2D, even though they incorporated excitation phase optimization.

This offset for 3D target pattern pulses is one of the future challenges that need to be addressed. Increasing the pulse length or applying pulse oversampling are options to increment the degrees of freedom. However, they also have their own drawbacks, such as increasing T1/T2 effects and elevated computational burden. A further solution could be

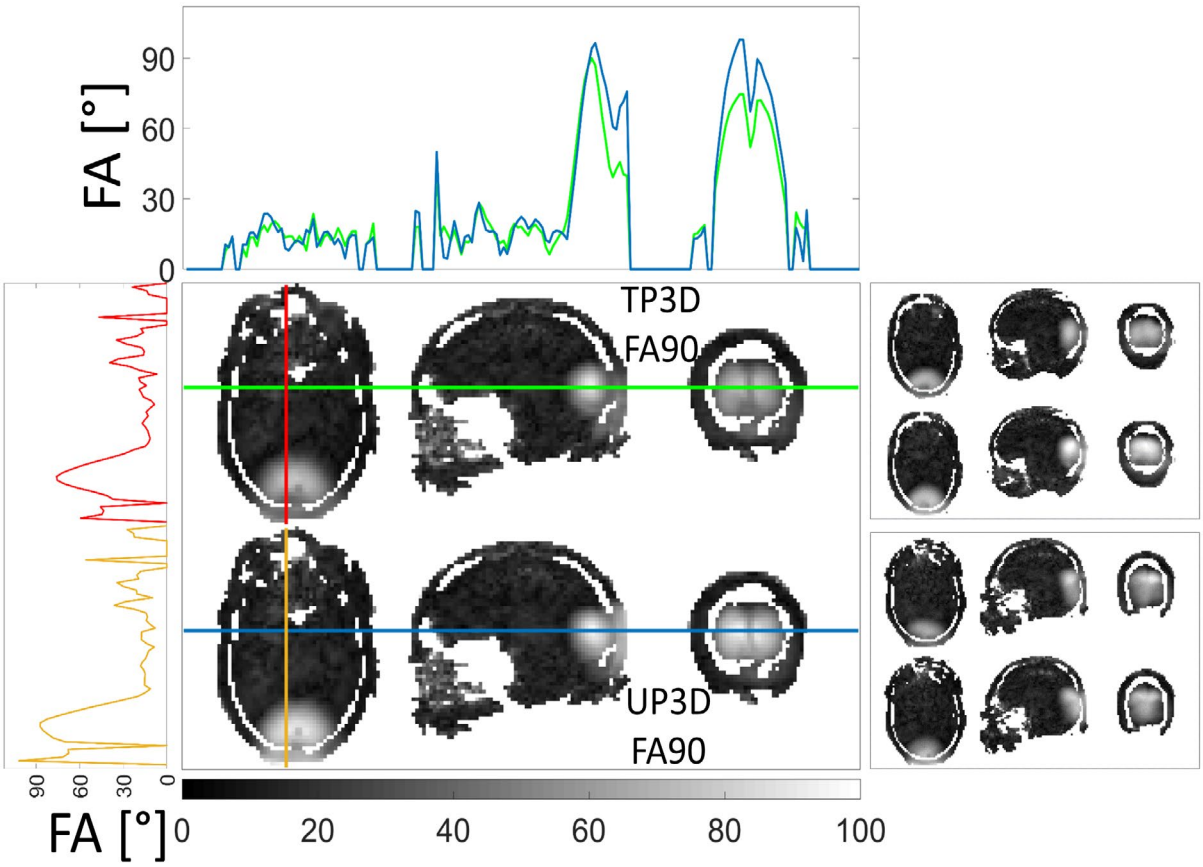

FIGURE 8 The central box and the two boxes on the right-hand side show FA profiles (represented by three slices respectively, slice positioning according to Figure 1B) from the three non-database heads, acquired in vivo with the satTFL B_1^+ mapping sequence. Both the respective TPs and UP3D for FA90 were applied to each head. The line charts left and above the central box show the FAs in the respective voxels in the FA profiles of the central box (marked by the colored lines in the images)

using another pulse design method, such as optimal control approaches,[44,52,53] which show good performance for designing LEx TPs at 7T. Extending the k-space domain parallel transmit pulse design method[54] for UP calculation could also be an option. Another possibility is the application of joint optimization methods that optimize the RF pulse shape and the k-space trajectory simultaneously.[55-57] In addition, using variable-density spiral k-space trajectories,[58,59] or completely different trajectories such as SPINS[60] or concentric shells,[13] could be worth investigating to excite a more accurate pattern.

Furthermore, the subject positioning procedure could be improved. Instead of aligning the top of the head, the subjects' eyes can be used as a reference for the position, in order to be more robust toward different head sizes/shapes. Another topic for future examinations could be to search for the optimal database size for designing LEx UPs at 9.4T.

The UP concept was originally invented for whole-brain excitation to mitigate the RF field inhomogeneity at 7T.[15-19] All of these studies are using kT-point[12] k-space trajectories based on which the pulse is optimized. During the design, the kT-points amplitudes, as well as their positions in the transmit k-space, are optimized simultaneously. By means of that approach, the authors created UPs for whole-brain excitation at 7T, which perform with an NRMSE of between 0.08 and 0.11 for non-database subjects. In the respective 9.4T feasibility study,[21] a whole-brain excitation UP with a target FA of 5° (180°) and a pulse length of 0.83 ms (3.98 ms), performs with an NRMSE of 0.129 (0.063) for the one tested head that was not contained in the design database. The average NRMSEs (0.114 for FA90, 0.115 for FA7) from UP3D for non-database heads for LEx we obtained in this study is in good agreement with the whole-brain excitation values from the literature. However, the values for the whole-brain excitation UPs and the LEx UPs are only partially comparable, as the whole brain UPs are shorter and just the kT-points' amplitudes and positions are optimized. For LEx UPs, we optimize the complete pulse shape sampled in 10 µs steps based on the spiral k-space trajectory, which is not changed during the optimization. Furthermore, a LEx target pattern creates a significantly more difficult optimization problem, as not every voxel is allowed to be excited. Only an area in the volume should be excited, while other areas should experience no excitation. Using kT-points pulse design for LEx applications is not possible due to the complexity of the optimization problem.

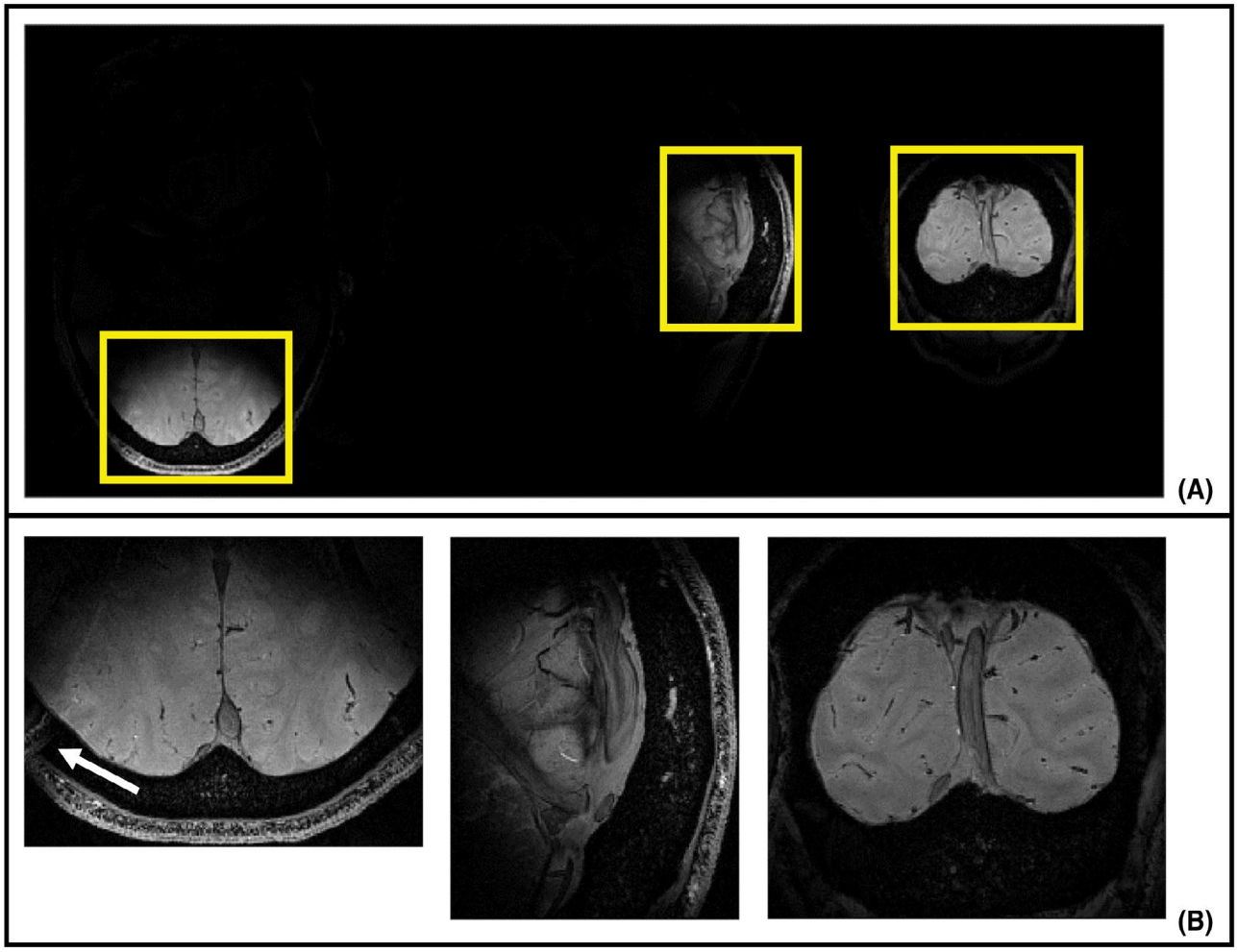

FIGURE 9 A, In vivo GRE images (represented by three slices respectively, slice positioning according to Figure 1B) from one non-database head acquired with UP3D (FA7) with full FOV. The yellow boxes in A mark the positioning of the reduced FOV applied in B. B, GRE image analog to A, but acquired with a reduced FOV. The white arrow depicts a slight folding artifact

Another interesting outcome of this study is that using spiral k-space trajectories for excitation seems to be more robust toward gradient nonlinearities than it is known from readout spirals. A possible reason for that observation may be that the RF pulse has a more significant influence compared to the applied transmit trajectory.

We demonstrated that UP3D can be used for reduced FOV acquisitions (Figure 9). Taking no acceleration methods (ie, GRAPPA[47]) into account and assuming the same spatial resolution of $0.4 \times 0.4 \times 0.4$ mm^3 for full FOV (Figure 9A) and reduced FOV (Figure 9B) measurement, the scan time duration of the full FOV acquisition theoretically would have been 75:16 min:sec (matrix size: $448 \times 560 \times 560$ (3D phase encoding, phase encoding, frequency encoding), TR = 18 ms). For the reduced FOV the scan duration was 10:53 min:sec (matrix size: $224 \times 162 \times 200$ (3D phase encoding, phase encoding, frequency encoding), TR = 18 ms). For an application in which only a certain transversal (here: the central transversal slice) is of interest, UP2D could also have been used, instead of UP3D.

A conventional way to image the visual cortex area as shown in Figure 9 would be to apply a coronal slab selective sinc pulse to excite a subvolume including the target. By again choosing the H->F direction as the frequency encoding direction, folding artifacts would be avoided in this direction. However, the FOV still needs to cover the entire L->R direction (448 steps) in order to avoid folding artifacts. For a slab sized equally to the reduced FOV scenario, that would result in 162 3D-encoding lines, respectively a scan duration of 21:46 min:sec (ie, twice of the reduced FOV scan time).

ACKNOWLEDGMENTS

Funding by the European Union (ERC Starting Grant, SYNAPLAST MR, Grant Number: 679927), the Deutsche Forschungsgemeinschaft (DFG – German Research Foundation) under the Reinhart Koselleck Programme (DFG SCHE 658/12), and the Cancer Prevention and Research Institute of Texas (Established Investigator Award RR180056) is gratefully acknowledged. Furthermore, we

would like to thank the Max Planck Computing & Data Facility in Garching (Germany) for using their Draco-Cluster. Open access funding enabled and organized by ProjektDEAL.

ORCID

Ole Geldschläger https://orcid.org/0000-0002-8400-0635
Dario Bosch https://orcid.org/0000-0002-6537-6370
Steffen Glaser https://orcid.org/0000-0003-4099-3177
Anke Henning https://orcid.org/0000-0002-2267-4861

REFERENCES

1. Pohmann R, Speck O, Scheffler K. Signal-to-noise ratio and MR tissue parameters in human brain imaging at 3, 7, and 9.4 Tesla using current receive coil arrays. *Magn Reson Med*. 2015;75:801-809.
2. Budinger TF, Bird MD, Frydman L, et al. Toward 20 T magnetic resonance for human brain studies: opportunities for discovery and neuroscience rationale. *Magn Reson Mater Phys, Biol Med*. 2016;29:617-639.
3. Uğurbil K. Imaging at ultrahigh magnetic fields: history, challenges, and solutions. *Neuroimage*. 2018;168:7-32.
4. Deniz CM. Parallel transmission for ultrahigh field MRI. *Top Magn Reson Imaging*. 2019;28:159-171.
5. Röschmann P. Radiofrequency penetration and absorption in the human body: limitations to high-field whole-body nuclear magnetic resonance imaging. *Med Phys*. 1987;14:922-931.
6. Ibrahim TS, Lee R, Abduljalil AM, Baertlein BA, Robitaille PML. Dielectric resonances and B1 field inhomogeneity in UHFMRI: computational analysis and experimental findings. *Magn Reson Imaging*. 2001;19:219-226.
7. Padormo F, Beqiri A, Hajnal JV, Malik SJ. Parallel transmission for ultrahigh-field imaging. *NMR Biomed*. 2015;29:1145-1161.
8. Katscher U, Börnert P, Leussler C, Brink JS. Transmit SENSE. *Magn Reson Med*. 2002;49:144-150.
9. Zhu Y. Parallel excitation with an array of transmit coils. *Magn Reson Med*. 2004;51:775-784.
10. Saekho S, Boada FE, Noll DC, Stenger VA. Small tip angle three-dimensional tailored radiofrequency slab-select pulse for reduced B1 inhomogeneity at 3 T. *Magn Reson Med*. 2005;53:479-484.
11. Saekho S, Cy Y, Noll DC, Boada FE, Stenger VA. Fast-kz three-dimensional tailored radiofrequency pulse for reduced B1 inhomogeneity. *Magn Reson Med*. 2006;55:719–724.
12. Cloos MA, Boulant N, Luong M, et al. kT-points: short three-dimensional tailored RF pulses for flip-angle homogenization over an extended volume. *Magn Reson Med*. 2011;67:72-80.
13. Schneider JT, Kalayciyan R, Haas M, et al. Inner-volume imaging in vivo using three-dimensional parallel spatially selective excitation. *Magn Reson Med*. 2012;69:1367-1378.
14. Zelinski AC, Angelone LM, Goyal VK, Bonmassar G, Adalsteinsson E, Wald LL. Specific absorption rate studies of the parallel transmission of inner-volume excitations at 7T. *J Magn Reson Imaging*. 2008;28:1005-1018.
15. Gras V, Vignaud A, Amadon A, Bihan DL, Boulant N. Universal pulses: a new concept for calibration-free parallel transmission. *Magn Reson Med*. 2016;77:635-643.
16. Gras V, Mauconduit F, Vignaud A, et al. Design of universal parallel-transmit refocusing kT -point pulses and application to 3D T2 -weighted imaging at 7T. *Magn Reson Med*. 2017;80:53-65.
17. Gras V, Pracht ED, Mauconduit F, Bihan DL, Stöcker T, Boulant N. Robust nonadiabatic T2 preparation using universal parallel-transmit kT -point pulses for 3D FLAIR imaging at 7 T. *Magn Reson Med*. 2019;81:3202-3208.
18. Gras V, Boland M, Vignaud A, et al. Homogeneous non-selective and slice-selective parallel-transmit excitations at 7 Tesla with universal pulses: a validation study on two commercial RF coils. *PLoS One*. 2017;12:e0183562.
19. Gras V, Vignaud A, Rabrait-Lerman C, et al. Gain of temporal signal-to-noise ratio with pTx universal pulses and the whole-brain fMRI 3D-GE EPI sequence at 7T. In Proceedings of the International Society for Magnetic Resonance in Medicine Meeting. Paris. 2018, p. 5440.
20. Wu X, Gras V, Vignaud A, et al. The travelling pulses: multi-center evaluation of universal pulses at 7T. In Proceedings of the International Society for Magnetic Resonance in Medicine 2018 Meeting (Paris), p. 1133.
21. Wiggins C, Poser B, Mauconduit F, Boulant N, Gras V. Universal pulses for MRI at 9.4 Tesla—a feasibility study. In 2019 International Conference on Electromagnetics in Advanced Applications (ICEAA); 2019: IEEE.
22. Zelinski AC, Wald LL, Setsompop K, Goyal VK, Adalsteinsson E. Sparsity-enforced slice-selective MRI RF excitation pulse design. *IEEE Trans Med Imaging*. 2008;27:1213-1229.
23. Geldschläger O, Shao T, Henning A. Universal parallel transmit pulse design for local excitation. In Proceedings of the International Society for Magnetic Resonance in Medicine Meeting 2018 (Paris), p. 3395.
24. Geldschläger O, Shao T, Henning A. Universal parallel transmit pulse design for 3-dimensional local-excitation—a 9.4T simulation study. In Proceedings of the International Society for Magnetic Resonance in Medicine 2019 Meeting (Montreal), p. 4639.
25. Geldschläger O, Herrler J, Nagel A, Henning A. Universal parallel transmit pulse design for 3-D local-excitation based on different sized databases of B0/B1+-maps—a 7T study. In Proceedings of the International Society for Magnetic Resonance in Medicine Meeting 2020 (Virtual conference), p. 3699.
26. Pauly J, Nishimura D, Macovski A. A k-space analysis of small-tip-angle excitation. *J Magn Reson*. 1989;81:43-56.
27. Stadler A, Schima W, Ba-Ssalamah A, Kettenbach J, Eisenhuber E. Artifacts in body MR imaging: their appearance and how to eliminate them. *Eur Radiol*. 2006;17:1242-1255.
28. Schneider J, Haas M, Hennig J, Junge S, Ruhm W, Ullmann P. Enhanced image resolution and reduced measurement time using inner volume imaging and parallel excitation. In Proceedings of the International Society for Magnetic Resonance in Medicine Meeting. Honolulu; 2009. Abstract 2601.
29. Wilm BJ, Svensson J, Henning A, Pruessmann KP, Boesiger P, Kollias SS. Reduced field-of-view MRI using outer volume suppression for spinal cord diffusion imaging. *Magn Reson Med*. 2007;57:625-630.
30. Malik SJ, Hajnal JV. Phase relaxed localized excitation pulses for inner volume fast spin echo imaging. *Magn Reson Med*. 2015;76:848-861.
31. Rosenkrantz AB, Chandarana H, Pfeuffer J, et al. Zoomed echo-planar imaging using parallel transmission: impact on image

quality of diffusion-weighted imaging of the prostate at 3T. *Abdom Imaging*. 2014;40:120-126.
32. Thierfelder KM, Sommer WH, Dietrich O, et al. Parallel-transmit-accelerated spatially-selective excitation MRI for reduced-fov diffusion-weighted-imaging of the pancreas. *Eur J Radiol*. 2014;83:1709-1714.
33. Waxmann P, Mekle R, Schubert F, et al. A new sequence for shaped voxel spectroscopy in the human brain using 2D spatially selective excitation and parallel transmission. *NMR Biomed*. 2016;29:1028-1037.
34. Patel G, Haas G, Darji N, Speck O. Evaluation of 2D spatially selective MR spectroscopy using parallel excitation at 7 T. *Quant Imaging Med Surg*. 2015;5:344-355.
35. Grissom W, Cy Y, Zhang Z, Stenger VA, Fessler JA, Noll DC. Spatial domain method for the design of RF pulses in multicoil parallel excitation. *Magn Reson Med*. 2006;56:620-629.
36. Stenger VA, Boada FE, Noll DC. Three-dimensional tailored RF pulses for the reduction of susceptibility artifacts inT∗2-weighted functional MRI. *Magn Reson Med*. 2000;44:525-531.
37. Yip CY, Fessler JA, Noll DC. Iterative RF pulse design for multidimensional, small-tip-angle selective excitation. *Magn Reson Med*. 2005;54:908-917.
38. Paige CC, Saunders MA. LSQR: an algorithm for sparse linear equations and sparse least squares. *ACM Trans Math Softw*. 1982;8:43-71.
39. Hoyos-Idrobo A, Weiss P, Massire A, Amadon A, Boulant N. On variant strategies to solve the magnitude least squares optimization problem in parallel transmission pulse design and under strict SAR and power constraints. *IEEE Trans Med Imaging*. 2014;33:739-748.
40. Gras V, Luong M, Amadona A, Boulant N. Joint design of kT-points trajectories and RF pulses under explicit SAR and power constraints in the large flip angle regime. *J Magn Reson*. 2015;261:181-189.
41. Domanski D, Percy AJ, Yang J, et al. MRM-based multiplexed quantitation of 67 putative cardiovascular disease biomarkers in human plasma. *Proteomics*. 2012;12:1222-1243.
42. Pauly JM, Hu BS, Wang SJ, Nishimura DG, Macovski A. A three-dimensional spin-echo or inversion pulse. *Magn Reson Med*. 1993;29:2-6.
43. Shao T, Xia L, Tao G, Chi J, Liu F, Crozier S. Advanced three-dimensional tailored RF pulse design in volume selective parallel excitation. *IEEE Trans Med Imaging*. 2012;31:997-1007.
44. Khaneja N, Reiss T, Kehlet C, Schulte-Herbrüggen T, Glaser SJ. Optimal control of coupled spin dynamics: design of NMR pulse sequences by gradient ascent algorithms. *J Magn Reson*. 2005;172:296-305.
45. Xu D, King KF, Zhu Y, McKinnon GC, Liang ZP. Designing multichannel, multidimensional, arbitrary flip angle RF pulses using an optimal control approach. *Magn Reson Med*. 2008;59:547-560.
46. Eichfelder G, Gebhardt M. Local specific absorption rate control for parallel transmission by virtual observation points. *Magn Reson Med*. 2011;66:1468-1476.
47. Griswold MA, Jakob PM, Heidemann RM, et al. Generalized autocalibrating partially parallel acquisitions (GRAPPA). *Magn Reson Med*. 2002;47:1202-1210.
48. Bosch D, Bause J, Ehses P, Zaiss M, Scheffler K. Rapid presaturated TFL transmit field mapping with an optimized 3D centric single-shot readout. In Proceedings of the International Society for Magnetic Resonance in Medicine Meeting 2020 (Virtual Conference), p. 3703.
49. Avdievich NI, Giapitzakis IA, Pfrommer A, Borbath T, Henning A. Combination of surface and "vertical" loop elements improves receive performance of a human head transceiver array at 9.4 T. *NMR Biomed*. 2017;31:e3878.
50. Pohmann R, Scheffler K. A theoretical and experimental comparison of different techniques for B1 mapping at very high fields. *NMR Biomed*. 2012;26:265-275.
51. Setsompop K, Wald LL, Alagappan V, Gagoski BA, Adalsteinsson E. Magnitude least squares optimization for parallel radio frequency excitation design demonstrated at 7 Tesla with eight channels. *Magn Reson Med*. 2008;59:908-915.
52. Vinding MS, Maximov II, Tošner Z, Nielsen NC. Fast numerical design of spatial-selective RF pulses in MRI using Krotov and quasi-Newton based optimal control methods. *J Chem Phys*. 2012;137:054203.
53. Vinding MS, Brenner D, Tse DHY, et al. Application of the limited-memory quasi-Newton algorithm for multi-dimensional, large flip-angle RF pulses at 7T. *Magn Reson Mater Phys, Biol Med*. 2016;30:29-39.
54. Ma J, Gruber B, Yan X, Grissom WA. k-Space Domain Parallel Transmit Pulse Design. *Magnetic Resonance in Medicine*. 2021;85:2568-2579.
55. Grissom WA, Khalighi MM, Sacolick LI, Rutt BK, Vogel MW. Small-tip-angle spokes pulse design using interleaved greedy and local optimization methods. *Magn Reson Med*. 2012;68:1553-1562.
56. Ma C, Xu D, King KF, Liang ZP. Joint design of spoke trajectories and RF pulses for parallel excitation. *Magn Reson Med*. 2010;65:973-985.
57. Davids M, Schad LR, Wald LL, Guérin B. Fast three-dimensional inner volume excitations using parallel transmission and optimized k-space trajectories. *Magn Reson Med*. 2015;76:1170-1182.
58. Kim DH, Adalsteinsson E, Spielman DM. Simple analytic variable density spiral design. *Magn Reson Med*. 2003;50:214-219.
59. Schröder C, Börnert P, Aldefeld B. Spatial excitation using variable-density spiral trajectories. *J Magn Reson Imaging*. 2003;18:136-141.
60. Malik SJ, Keihaninejad S, Hammers A, Hajnal JV. Tailored excitation in 3D with spiral nonselective (SPINS) RF pulses. *Magn Reson Med*. 2011;67:1303-1315.

SUPPORTING INFORMATION

Additional supporting information may be found online in the Supporting Information section.

FIGURE S1 A: First row: Bloch simulated FA profiles of the FA90 UP2D (downscaled to FA7). Second row: Bloch simulated FA profiles of a UP directly designed with target FA of 7°. B: Mean and standard deviation bars of the FAs in the excited (upper values) and non-excited regions (lower values) of each head. The green markers depict the values achieved with the downscaled UP2D, the blue markers depict the values achieved with the directly FA7 designed UP2D (legend visible in C). C: Bar plot illustrating the NRMSEs between target pattern and resulting profile for each pulse and head

FIGURE S2 C: First row: Bloch simulated FA profiles of the FA90 UP3D (downscaled to FA7). Second row: Bloch simulated FA profiles of a UP directly designed with target FA of 7°. Three representative database heads and all non-database

heads are shown. A: Mean and standard deviation bars of the FAs in the excited (upper values) and non-excited regions (lower values) of each head. The green markers depict the values achieved with the down-scaled UP2D, the blue markers depict the values achieved with the directly FA7 designed UP2D (legend visible in B). B: Bar plot illustrating the NRMSEs between target pattern and resulting profile for each pulse and head

FIGURE S3 A: B_0 map of the central transversal slice of each database head in Herz. B: B_1^+ map from each transmit channel of the central transversal slice of each database head in nano Tesla per Volt

FIGURE S4 A: Mean FAs and standard deviation bars in the respective excitation or non-excitation regions in the Bloch simulated FA profiles for UP3D (FA90) and the respective TPs. B: Analog to A, but for FA7

FIGURE S5 Left: Mean FAs and standard deviation bars in the respective excitation or non-excitation regions from the in vivo 2D FA maps from Figure 4. Right: Mean FAs and standard deviation bars in the respective excitation or non-excitation regions from the in vivo 3D FA-maps from Figure 8

FIGURE S6 Analog to Figure 5 from the main document, except that the TPs were designed by means of the magnitude least-squares optimization

How to cite this article: Geldschläger O, Bosch D, Glaser S, Henning A. Local excitation universal parallel transmit pulses at 9.4T. *Magn Reson Med*. 2021;00:1–15. https://doi.org/10.1002/mrm.28905

PUBLICATION 3

OTUP-workflow: Target specific optimization of the transmit k-space trajectory for flexible universal parallel transmit RF pulse design.

Geldschläger O, Bosch D, Henning, A.

(submitted to Magnetic Resonance in Medicine, under review)

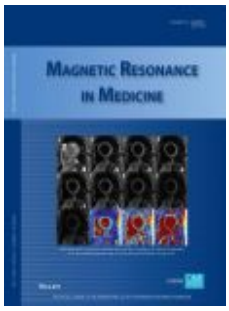

OTUP-workflow: Target specific optimization of the transmit k-space trajectory for flexible universal parallel transmit RF pulse design

Journal:	*Magnetic Resonance in Medicine*
Manuscript ID	MRM-21-22559
Wiley - Manuscript type:	Research Article
Research Type:	High field MR techniques < Technique Development
Research Focus:	Brain < Neurological

OTUP-workflow: Target specific optimization of the transmit k-space trajectory for flexible universal parallel transmit RF pulse design

Authors: Ole Geldschläger[1], Dario Bosch[1,2], Anke Henning[1,3]

1: High-Field Magnetic Resonance Center, Max Planck Institute for Biological Cybernetics, Tübingen, Germany

2: Biomedical Magnetic Resonance, University Hospital Tübingen, Tübingen, Germany

3: Advanced Imaging Research Center, University of Texas Southwestern Medical Center, Dallas, TX, United States

Corresponding author:

Ole Geldschläger

High-Field Magnetic Resonance Center

Max Planck Institute for Biological Cybernetics

Max-Planck-Ring 11

72076 Tübingen

E-mail: ole.geldschlaeger@tuebingen.mpg.de

Tel.: +49 7071 601 729

Total word count of the main document (without references): 5099/5000

Total word count of the abstract (without keywords): 250/250

Running head/title:

Grant sponsors: This project was co-sponsored by the European Research Council / SYNAPLAST MR / Grant number: 679927, the Deutsche Forschungsgemeinschaft (DFG – German Research Foundation) under the Reinhart Kosseleck Programme (DFG SCHE 658/12) and the Cancer Prevention and Research Institute of Texas (CPRIT) / Grant number: RR180056.

Abstract

Purpose:

To optimize transmit k-space trajectories for a wide range of excitation targets and to design 'Universal pTx RF pulses' based on these trajectories.

Methods:

Transmit k-space trajectories (stack-of-spirals and SPINS) were optimized to best match different excitation targets using the parameters of the analytical equations of spirals and SPINS. The performances of RF pulses designed based on optimized and non-optimized trajectories were compared. The optimized trajectories were utilized for universal pulse design. The universal pulse performances were compared with subject specific tailored pulse performances.

The workflow was tested on three test target excitation patterns. For one target (local excitation of a central area in the human brain) the pulses were tested in vivo at 9.4T.

Results:

The workflow produced appropriate transmit k-space trajectories for each test target. Utilization of an optimized trajectory was crucial for the pulse performance. Using unsuited trajectories diminished the performance.

It was possible to create target specific universal pulses. However, not every test target is equally well suited for universal pulse design. There was no significant difference in the in vivo performance between subject specific tailored pulses and universal pulse at 9.4T.

Conclusions:

The proposed workflow further exploited and improved the universal pulse concept by combining it with gradient trajectory optimization for stack-of-spirals and SPINS. It emphasized the importance of a well-suited trajectory for pTx RF pulse design. Universal and tailored pulses performed highly similarly.

The implemented OTUP-workflow and the B_0/B_1^+ map data from 18 subjects measured at 9.4T are available as open source (https://github.com/ole1965/workflow_OTUP.git).

Keywords: parallel transmit, pTx, universal pulses, local excitation, reduced FOV, high-field MRI, 9.4T, gradient optimization

Introduction

The great potential of MRI scanners operating at ultra high field (UHF) (i.e. a B_0 field strength of 7T and above) was extensively discussed[1,2,3]. UHF systems provide higher signal-to-noise ratios[4], reduced acquisition times and improved spatial resolutions. However, the shorter electromagnetic wavelength at UHF results in inhomogeneity of the radiofrequency (RF) field. The most promising approach to overcome these issues is the parallel transmission (pTx) technique, as it provides improved control over the spatial and temporal RF field[5,6].

PTx RF pulse design is accompanied with an underlying transmit (or excitation) k-space trajectory spanned by appropriate gradients. Usually the pTx pulse is calculated based on that transmit k-space trajectory. Both are played out simultaneously, resulting in excitation of the spins in a scanned object. For a desired target excitation pattern 'the choice of a suitable transmit k-space trajectory is crucial'[7]. For non-selective (whole brain) and slice selective excitation, various studies have optimized the positions of 'kT-points'[8,9] and 'spokes'[10,11] trajectories together with an appropriate RF pulse. RF pulses based on more sophisticated and optimized trajectories such as 'stack-of-spirals' (SOS)[12], 'concentric-shells'[12] and spiral nonselective (SPINS)[13]-trajectories were also investigated in the past, both in simulations[14,15] and measurements (in rats)[7].

In the first part of the following workflow (called OTUP), we optimized transmit k-space trajectories for pTx RF pulse design. For three test target excitation patterns, we investigated and optimized four basis trajectories. These trajectories were a single variable density spiral-in trajectory[16,17,18] (1SOS), a two stack of variable density spiral-in trajectory[12,14] (2SOS), a three stack of variable density spiral-in trajectory (3SOS) and a SPINS[13] trajectory. Davids et al.[15] were optimizing these trajectories utilizing certain shape parameters for each trajectory. For each set of shape parameters a set of control points was assigned. Connecting these control points resulted in the final trajectory, based on which a pTx pulse was designed and evaluated. The optimized trajectories and resulting pulses were tested only in simulations. In the current work we utilized a similar approach. However, we considered the analytical equations of spirals[16] and SPINS[13] in order to create the trajectories. The parameters to be optimized were the parameters of these equations.

During the second part of this study, so-called 'Universal pTx RF Pulses'[19] (UPs) based on the optimized k-space trajectories were designed.

Traditionally the transmit RF field (B_1^+) and the static magnetic field (B_0) distribution is measured for each subject and based on this information the pTx RF pulse is calculated during the scan session. The concept of UPs was introduced by Gras et al.[19] to circumvent this pTx inherent lengthy calibration procedure. The major idea of the UP concept is to design RF pulses based on a database of B_0/B_1^+ maps from different subjects prior to pTx scan sessions. Due to the similarity of these maps for most subjects, the UPs also perform well on subjects which were not contained in the pulse design database.

The UP concept was proved[20,21] and developed[9,22,23] for different sequences, applications and RF coils at 7T. These works have in common that they present UPs for nonselective or slice selective excitation, based on 'kT-points'[8] or 'spokes'[10]. Additionally, a recent study performed a combination of UPs and subject specific tailored pulses (TPs)[24] for whole brain excitation using SPINS[13] trajectories.

Most recently, we published a feasibility study for local excitation (LEx) UPs at 9.4T[25]. We created LEx UPs based on fixed non-optimized spiral transmit k-space trajectories, which locally excited the visual cortex region of the human brain, while the surrounding tissues experienced only minor excitation.

The UPs in the current study were calculated based on the optimized k-space trajectories. As UPs can be calculated offline with (theoretically) no time limitation, additional computation time to optimize the trajectories next to the actual RF pulse is not problematic. The entire OTUP workflow was tested on three different target excitation patterns (two LEx- , one 'whole brain like'-target pattern). For one target the resulting RF pulses and transmit trajectories were applied in vivo at 9.4T for proof of principle. The OTUP code was made available as open source.

Methods

Test target patterns

The following three target excitation patterns (Figure 1) were created in order to test the workflow:

- 'targetNuclei': A small central region encompassing the red nuclei should be excited with a homogenous flip angle (FA) of 7° in eight consecutive transversal slices. The surrounding voxels within these slices should not experience excitation. The voxels directly adjacent to the excited region were excluded from the pulse design mask, to avoid a direct transition from excitation to non-excitation regions, thereby reducing the complexity of the optimization problem. The red nuclei are small structures in the human rostral midbrain involved in motor coordination[26]. This structure is of special interest for research on Parkinson's disease[27,28] and may be of interest for practical reduced FOV application.
- 'targetM': The letter 'M' should be excited with a FA of 7° in one central transversal slice. The surrounding voxels within these slices should experience no excitation. Desired excited and non-excited voxels are directly adjacent. This target pattern served as a 'proof of concept' pattern.
- 'targetWB': All brain voxels located in 16 consecutive transversal slices should be excited with a homogenous FA of 7° (i.e. there are no voxels which were not allowed to experience excitation). Excitation of the whole brain was not possible as the coverage of the utilized RF coil was not sufficient to reach the upper and lower brain (see B_1^+ maps in the supporting information Figure S1).

All target patterns had in common, that the transversal slices located above or below the slices of interest (see red horizontal lines in Figure 1) are excluded from the pulse design mask, i.e. the performance of the pulse in these excluded slices is neither evaluated nor optimized by the pulse design algorithm. This approach is feasible since the head to feet direction was chosen as the frequency encoding direction for in vivo imaging. Thereby, folding artifacts from tissues above and below the red lines would not appear.

For each of the three targets pattern the OTUP workflow consisting of 'Gradient Trajectory optimization' and 'Final UP calculation' was tested. The workflow was implemented in Matlab (MathWorks, Natick, MA) and is available as open source (https://github.com/ole1965/workflow_OTUP.git).

Gradient Trajectory optimization

In order to save computation time, we optimized the transmit k-space trajectory based on only one head from the design database. Afterwards the UPs were designed on B_0/B_1^+ maps from the entire design database using the resulting optimal k-space trajectories (see 'Final UP calculation' section).

Four different basis k-space trajectories were chosen: A single variable density spiral-in trajectory[16,17,18] (1SOS), a two stack of variable density spiral-in trajectory[12,14] (2SOS), a three stack of variable density spiral-in trajectory (3SOS) and a spiral nonselective trajectory (SPINS)[13].

A single variable density spiral-in trajectory[16] can be represented by:

$$k(t) = \lambda t^{\alpha} e^{i\omega t} \quad \text{Eq. 1}$$

with $t = 1, 1 - \frac{1}{T-1}, 1 - \frac{2}{T-1}, \ldots, 0,$ where $T \in \mathbb{N}$ is the length, $\lambda \in \mathbb{R}_{>0}$ is the radial extent of the spiral, $\alpha \in \mathbb{R}_{>0}$ is the density variable and $\omega = 2\pi n$, with n is the number of spiral turns.

For 1SOS Eq. 1 was implemented in a cost-function having the equation parameter T, λ, α, n and the position z of the spiral on the k_z-axis as input parameter. Within the cost-function, the spiral k was created based on these input parameters. For that trajectory, a RF pulse was designed based on the B_0/B_1^+ map of one subject. For RF pulse design the 'Spatial domain method'[29] was utilized because of its speed, due to the small tip angle approximation[30] of the Bloch equations. The output parameter of the cost-function was the root mean squared error (RMSE) between the FA profile of that pulse (Bloch simulated) and the target excitation pattern.

For 2SOS and 3SOS the procedure was analogous with the only exception that two or three spirals were designed, respectively. For 2SOS the cost-functions input parameter were $T_1, \lambda_1, \alpha_1, n_1$ for the first spiral and $T_2, \lambda_2, \alpha_2, n_2$ for the second spiral, as well as z_1 and z_2 as the positions on the k_z-axis. For 3SOS a third spiral with corresponding input parameters for the cost-function was added.

A SPINS trajectory[13] can be created using Eq. 2-4:

$$k_r(t) = \frac{k_{max}}{1 + e^{\alpha(\frac{t}{T} - \beta)}} \quad \text{Eq. 2}$$

$$k_\theta(t) = ut \quad \text{Eq. 3}$$

$$k_\varphi(t) = vt \quad \text{Eq. 4}$$

Where k_r is the radial coordinate and k_θ and k_φ are the polar and azimuthal angles. The parameter $k_{max} \in \mathbb{R}_{>0}$ is the maximum radial extent, $u \in \mathbb{R}_{>0}$ and $v \in \mathbb{R}_{>0}$ are the respective angular velocities and $T \in \mathbb{N}$ is the length of the trajectory. Additional parameters are $\alpha, \beta \in \mathbb{R}_{>0}$. Similar to 1SOS, 2SOS and 3SOS a cost-function with the SPINS parameter ($k_{max}, \alpha, \beta, u, v, T$) as input parameter was implemented in order to create a SPINS trajectory for each set of parameters and to design a pulse based on this trajectory.

Trajectories that exceeded the maximum gradient amplitude or slew rate were punished with a very high cost-function output value, in order to prevent the optimization from considering these trajectories as optimum. The maximum allowed trajectory duration was 10ms. Reasonable lower and upper bounds for the input parameters were found empirically. Each basis k-space trajectory was optimized separately. From the four optimized trajectories the one that enabled the lowest RMSE performance or a considerably shorter duration with similar RMSE, was considered for UP calculation.

To solve the four optimization problems the 'Particle swarm optimization'[31], implemented in Matlabs *particleswarm* function was utilized. Particle swarm optimization 'works by maintaining a swarm of particles that move around in the search-space influenced by the improvements discovered by the other particles'[32]. This optimization routine was chosen because it creates a reliable overview on the entire search-space and it does not require an initial guess, which would be hard to find in this case. As this algorithm is stochastic and non-deterministic the calculated optimum of the *particleswarm* function can differ from one call to another. For that reason, the *particleswarm* function was executed 20 times for each cost-function mentioned above. From the 20 optimized parameter sets, the one that provided the lowest RMSE was utilized for further RF pulse calculation. In case several parameter sets provided equal or highly similar RMSE values, the one that produced the shortest trajectory duration was used further.

In order to show the influence of the underlying transmit trajectory on the RF pulse performance, we tested each of the optimized trajectories for each of the test targets, respectively. For instance, for targetWB, we calculated pulses based on the optimal trajectory for targetNuclei, targetM and targetWB, respectively. The pulses were calculated and applied on one example subject using Bloch simulations.

Final UP calculation

Analog to the own preliminary work[25] the following optimization problem was considered in order to create a pulse p_{UP}^{*} that excites the same target pattern on multiple heads (i.e. the UP):

$$\boldsymbol{p}_{UP}^{*} = \arg\min_{\boldsymbol{p}} \left\{ \left\| \left| \begin{bmatrix} \boldsymbol{A}_{full,1} \\ \vdots \\ \boldsymbol{A}_{full,N_{DB}} \end{bmatrix} \boldsymbol{p} \right| - \begin{bmatrix} \boldsymbol{m}_{tar} \\ \vdots \\ \boldsymbol{m}_{tar} \end{bmatrix} \right\|^{2} \right\}, \qquad \text{Eq. 5}$$

where $A_{full,j}$, with $j = 1, \dots, N_{DB}$, is the full system information matrix[29] of subject j and N_{DB} is the size of the design database, i.e. the number of subject heads based on which the pulse will be designed. $\boldsymbol{p}$ is the RF pulse and $\boldsymbol{m}_{tar}$ is the target excitation pattern. This approach is an extension of the spatial domain method[29].

For each test target and optimized trajectory, we solved this optimization problem in Eq. 5 with a combination of the 'magnitude least squares' (MLS) optimization[33] and the active-set algorithm implemented in Matlabs *fmincon*-function.

The MLS optimization relies (similar to the spatial domain method) on the small tip angle approximation[30] but considers only the resulting magnetization profile's magnitude in the optimization process. The spatial domain method used within the gradient optimization was drastically faster but includes the profile's phase and magnitude in the optimization. However, the profile's phase was of no

interest during this study. Considering only the profiles magnitude and not the phase in the pulse design results in an improved pulse performance for applications where the profile's phase is of no relevance[33].

Similar to the own preliminary work[25] the MLS result was post processed in order to potentially further improve the pulse performance. The MLS pulse was utilized as the initial guess for the active-set algorithm. Within the cost-function minimized by the active-set algorithm the FA profile for a given pulse was simulated with Bloch equations (without relaxation). The output parameter of the cost-function was the RMSE between the resulting FA profile and the target FA pattern.

In line with the literature[19,20,22,21], the active-set algorithm was chosen because of its speed and robustness[34,9]. With the *fmincon*-function the solution was constrained to a maximum pulse amplitude of 130 Volt at plug level (hardware limit). The optimization was stopped if further improvement on 30 consecutive iterations was negligible.

The final UPs were simulated on 7 non-database heads using Bloch-equations. Their performances were compared with the corresponding TP performances. The TPs were calculated with the MLS method only.

For all of the mentioned calculations a target FA of 7° was set. In the 'Results'-section we will only focus on the results for that FA. However, we ran analogous calculations for targetNuclei for a FA of 180° (results are shown in the supporting information Figure S4).

The UP design database consisted of the B_0/B_1^+ maps from 11 different subjects. The 11 datasets were randomly chosen from the 18 overall acquired B_0/B_1^+ maps at 9.4T. In the supporting information we provide an 'Analysis of database size', where we explain why the design database contains 11 heads.

All calculations (gradient trajectory optimization, analysis of database size (supporting information) and final UP calculation) were performed on a high-performance-compute system node equipped with an Intel Xeon IceLake Platinum 8360Y processor (256 GB RAM, 72 cores with 2.4 GHz each) exploiting parallel computing.

Measurement system and data acquisition

All measurements were performed on a 9.4T whole-body MR scanner ('Magnetom 9.4T', Siemens Healthcare, Erlangen, Germany) equipped with a SC72 whole-body gradient system, with a maximum amplitude and slew rate of 40mT/m and 200 mT/m/ms, respectively. An in-house-built 16 channel tight-fit array coil[35], consisting of eight transceiver and eight receive-only loops was used. All experiments were performed with approval of the local Ethics Committee. Informed signed consent was obtained from each volunteer, before each MR-experiment.

Individual-channel B_1^+ mapping was performed using a 3D presaturated TurboFLASH sequence[36] (TR=2.44ms, TE=0.75ms, BW=700Hz/Px, asymmetric echo, elliptical k-space acquisition, GRAPPA[37] 2x2, recovery time between acquisitions=7.5s, nominal FA saturation = 60°, FA readout = 4°). For B_0 mapping an additional scan with 500µs prolonged TE was utilized. B_0 were then calculated from the phase evolution between two different echo times. All maps were acquired with a 3.5mm isotropic spatial resolution and a matrix size of 64x64x64. With these scanning procedure 18 different subjects were measured. The resulting B_0/B_1^+ maps can be seen in the supporting information Figure S1.

Tissue masks were created using a masking routine based on a neuronal network[25].

The final UP for targetNuclei was applied in vivo at 9.4T as proof of principle example. In order to test the in vivo performance for targetNuclei, the calculated pulses were applied in a T2*-weighted 3D short TR spoiled GRE-sequence (voxel size: 0.8x0.8x0.8mm^3, matrix size: 224 (left to right) x 280 (anterior to posterior) x 280 (head to feet), 3D encoding direction: left to right, phase encoding direction: anterior to posterior, frequency encoding direction: head to feet, TR=18ms, TE=8ms, BW=260Hz/px, GRAPPA 2x2).

Global and local SAR were supervised using the VOP method[38,39]. The dwell time for RF pulses and gradient shapes was 10 µs. The scanner inherent gradient delay of 4µs was taken into account in the pulse files.

Results

Gradient Trajectory optimization

Figure 2 shows the optimized transmit k-space trajectories. It should be noted that all plots have the same k_x and k_y axes limits, however, for the sake of clarity the limits of the k_z axes of the SPINS plots differs from the limits of the k_z axes of the SOS plots. The RMSE values next to each plot are based on the difference between the target FA profile and the respective Bloch simulated FA profile (i.e. the unit of the RMSE is degree).

For targetNuclei the 1SOS optimization resulted in a 9.44ms long spiral located on -3m^{-1} on the k-space z-axis. The spiral had an extent of approximately ±80m^{-1} on the k_x and k_y axis. The first of the two spirals from the 2SOS result (6.5ms) had the same extent. The extent of the second spirals is approximately half of the extent of the first spiral. One spiral of the 3SOS result (8.37ms) had an extent of ±100m^{-1} in k_x and k_y direction. Next to a second, smaller spiral, the optimization created an additional very short third spiral shaped like an arc or a half-turn, rather than a full spiral. The SPINS optimization resulted in a trajectory (9.38ms) similar to a concentric 3D-shell[7].

As the 2SOS trajectory enables the shortest duration (6.5ms), while having a similar RMSE as the other trajectories (0.26), it was chosen for UP calculations for targetNuclei.

The trajectories for targetM extended further into the outer k-space compared to the targetNuclei trajectories. The 1SOS and the 2SOS results were very similar having one large spiral reaching ±150m^{-1} on the the k_x and k_y axis (one spiral of the 2SOS result is only an arc). The 3SOS result consisted of a big low density spiral having the same k_x and k_y extend as 1SOS and 2SOS and smaller spiral underneath. The third spiral, again, was only an arc. The SPINS result had a similar extend on the k_x and k_y axis, but a large extend on the k_z axis (from 0m^{-1} till -400m^{-1}).

Again, all four results were similarly well suited for RF pulse design, i.e. all four RMSE values were between 0.15 and 0.17. All trajectories exploited the maximum allowed duration of 10ms. The SPINS result was considered for further pulse calculations for targetM because it showed the best performance.

For targetWB all trajectories exhibited a drastically lower extend in k-space compared to the targetNuclei and targetM trajectories. Additionally, the durations are shorter compared to the durations

from the other trajectories. As the 3SOS result constituted the best compromise between duration (3.96ms) and RMSE (0.36) this trajectory was chosen for further pulse calculations for targetWB.

The calculation time for each of these k-space trajectory optimizations was below 24 hours, respectively (depending on the target (Figure 1)).

As Figure 3 shows, for each target pattern the associated optimal transmit trajectory enabled the best performing RF pulse. However, if the underlying trajectory was not designed for the respective target pattern, the RF pulse performance diminished. This effect is most pronounced in case the optimal trajectory for targetM pattern is applied to the targetWB pattern and vice versa. The maximum pulse voltages were relatively low if the RF pulse was designed based on the trajectory designed for a certain target. Utilizing a suboptimal trajectory can lead to dramatically higher pulse amplitudes (for instance, 586V for targetWB using the targetM trajectory, 24V using the targetWB trajectory).

Final UP calculation

For targetNuclei, the *fmincon* function was stopped after 395 iterations (~9 days). Figure 4 presents a comparison between the simulated performances of the UP and the corresponding TPs on seven non-database heads. The TPs were slightly outperforming the UP. The computation time of each TP was ~24 seconds (pulse length: 6.5ms). The FA profiles resulting from the TPs exhibited a uniform excitation of the desired excitation area with mean FAs close to 7°. The desired non-excitation areas were in some voxels only very slightly excited with mean FAs close to 0°. The mean RMSE performance of the TPs (UP) was 0.25 (0.52). For the UP the mean FAs in the nuclei area were between 6° and 7° (except of head 14) and the excitation in the desired non-excitation areas was close to 0°.

Analogously, Figure 5 displays the TP and UP performances for targetM. The mean TP (UP) RMSE performance was 0.14 (0.53). Each TP created an excitation perfectly shaped like an 'M'. For the UP (*fmincon* function was stopped after 820 iterations, ~6days) the transition between desired excitation and non-excitation voxels was not as sharp as for the TPs (computation time per TP was approximately 5 seconds, pulse length: 9.92ms). The mean UP excitation within the 'M' is mostly between 6° and 7.5°. However, for head 14 the mean excitation was 5.3°.

In Figure 6 pulse performances for targetWB are depicted. The TPs reached a mean excitation of 7° on all heads, the mean RMSE performance was 0.38. The computation time per TP was approximately 22 seconds (pulse length: 3.96ms). The mean RMSE for the UP was 0.81 (*fmincon* function was stopped after 950 iterations, ~11days). It was striking that especially on head 14 the UP performance was insufficient, but also on head 12 and 13 the RMSEs differed considerably between UP and the corresponding TPs. For heads 15-18 the UP and TPs performances were similar.

The targetNuclei UP performance was satisfactory on all non-database heads. It provided the lowest difference between the mean RMSE TP value and the mean RMSE UP value (0.27). For that reason, the pulses for targetNuclei were tested in vivo at 9.4T. Additionally, targetNuclei was tested for calculation of pulses with a FA of 180° in the target excitation area. The results are presented in the supporting Figure S4.

In Figure 7 GRE images of two different non-database subjects with targetNuclei excitation are visible. For both subjects, UP and TPs images appeared almost identical. The central voxels containing the nuclei were excited relatively uniformly, while excitation in the surrounding tissues was visible, but drastically lower compared to the desired excitation area. The mean excitation values and standard deviation were highly similar. For the UP, the mean excitation in the desired excitation area was 0.33 for the one subject and 0.40 for the other subject. In the desired non-excitation areas the excitation was 0.04 and 0.05 (only about 12% of the excited region). For the TPs these values were very similar.

Discussion

This work presents the OTUP workflow to optimize the underlying transmit k-space trajectory for pTx UPs and through that further exploit the advantages of the UP concept.

As the theoretically unlimited computation time is one of the main advantages of UP design, the underlying transmit k-space trajectories is optimized to achieve the best possible match with the excitation target (up to 24hours) before the actual UP design process started. For each of three test target excitation patterns (Figure 1), four basis transmit trajectories were optimized, respectively. The optimization procedure was also utilized for subject specific TP designed herein for comparison.

The optimized k-space trajectories revealed that with increasing complexity of the target excitation pattern the extent of the optimized trajectories in k_x and k_y direction in k-space increased. For the least complex targetWB (i.e. excitation of 16 entire transversal brain slices) the optimized trajectory ran close to the k-space center, covering only low frequencies. For that reason, the targetWB trajectory is unsuitable for excitation of targetM (i.e. the most complex target pattern exciting only the voxels along an area shaped like the letter 'M') (Figure 3).

For targetM, a very sharp transition between excitation and non-excitation between adjacent voxels needed to be achieved. The optimized targetM trajectory covered high frequencies and expanded till $\pm 150 m^{-1}$. That resulted in a k-space FOV of $300 m^{-1}$ in k_x and k_y direction. Converting this value to the voxel size in the image space (i.e. calculating the reciprocal of the k-space FOV) results in the utilized voxel size of the B_1^+ maps of 3.5mm approximately. As visible in Figure 3, such high frequencies are unsuited for excitation of targetWB.

As some of the spirals in the SOS trajectory optimization reduced to arcs (i.e. the shortest possible spiral) the number of spirals could be included as another parameter to be optimized in future optimizations.

Interestingly, the SPINS trajectories had completely different shapes for the three tested excitation targets. Although originally thought to be well suited for entire brain slices[13], the proposed optimization method created a SPINS trajectory that was also well suited for the complex LEx targetM. In general, SPINS tend to have a longer duration for similar RMSEs as SOS trajectories.

While in the current work the underlying transmit trajectories were optimized, the following two and numerous other pulse design studies[29,33,40,41,7] have in common, that the respective transmit trajectories were only adapted to a given target pattern, field of view and matrix size, rather than an actual trajectory optimization. Any RF pulse calculations started only after the transmit trajectories were fixed.

Shao et al.[14] presented the concept of transmit k-space trajectory container 'that shapes and forms the candidate trajectory'[14] based on which the RF pulse will be designed later. In Malik et al.[13], the study that introduced the SPINS trajectory, the parameters of the analytical equation of the SPINS were adapted in order to match the excitation target pattern (homogenous excitation of five brain slices). For instance, 'k_{max} was chosen to cover sufficiently high spatial frequencies to correct for typical B_1^+ variations across the adult brain' at 3T. With that approach a 1ms SPINS trajectory were designed that enables a subject specific tailored RF pulse performing with a normalized RMSE (NRMSE) of 5.5% on the whole brain at 3T (target FA: 8°). The mean TP performance for targetWB with the optimized 3SOS from the current study was also 5.5% (mean TP RMSE of 0.38 divided by the FA of 7°), but the utilized field strength of 9.4T was drastically higher herein.

An actual optimization of the k-space trajectory was performed for spokes[11,42,10,43]- and kT-points-trajectories[9], where the location of the spokes and the kT-points is optimized simultaneously with the RF pulse for non-selective or slice selective excitation.

In a 7T study[19], 0.7ms long kT-point TPs performed with ~7% (NRMSE) for a target FA of 9° for whole brain excitation. Davids et al.[15] presented a NRMSE of 6.2% for whole brain excitation with a 4.5ms optimized shells trajectory. The 3SOS TPs for targetWB from the present study (NRMSE: 5.5%) outperformed these two NRMSEs from the literature, but has a considerably longer duration as the kT-point pulse (3.96ms versus 0.7ms).

Furthermore, Davids et al.[15] tested a LEx target pattern exciting a cube at the back of the head (NRMSE: 3.6%, duration: 5ms). This cube target is comparable with respect to its complexity to targetNuclei from this work (NRMSE: 3.7%, duration: 6.5ms).

In order to create and optimize the k-space trajectories SOS, shells and cross, Davids at al.[15] assigned a set of up to 50 control points for each set of certain shape parameters for the respective basis trajectory. These control points needed to be connected afterwards with further software[44]. In contrast, in the current work, the trajectories were created by analytical equations for given parameters, what is more straightforward and easier to implement as the approach in the literature.

It should be noted, that none of the presented performance values from the literature is directly comparable to the values from the present work, as the utilized coils, target pattern and field strengths differed, respectively. However, the OTUP workflow yielded optimized transmit trajectories and TPs that produces similar or improved performances compared to the approaches in the literature. Only for whole brain excitation, optimized kT-points trajectories seems to have advantages in terms of the pulse duration.

For each test target, the optimal trajectory was utilized to calculate UPs. Considering the UP results for targetWB it was conspicuous that the UP performance on head 14 is drastically lower as the performance on the remaining non-database heads. Taking all heads except of head 14 into account the mean RMSE (NRMSE) is 0.72 (~10%). Head 14 exhibited a different head size and shape compared to the other heads which is most likely the reason for the poor UP performance on that head. In order to avoid such suboptimal performances in the future, different UPs for different head sizes and shapes should be designed.

The UP performances for targetWB (without consideration of head 14) slightly outperformed the kT-point UPs for whole brain excitation from Gras et al.[19] (mean UP NRMSE of 12% for a target FA of 9° on non-database heads). However, as already mentioned, the duration of the kT-point trajectory (0.7ms) is drastically lower as the duration of 3SOS trajectory utilized in the current study (3.96ms).

In an own previous study[25] we presented UPs for LEx of the visual cortex in the human brain, based on non-optimized transmit trajectories (duration: 8.18ms). These UPs performed with a mean NRMSE of 11.4% on non-database heads. This visual cortex target is comparable to targetNuclei from the present work. With optimized transmit trajectories we were able to outperform the UPs from the previous study, as we achieved a mean UP NRMSE for targetNuclei of 7.4% and a pulse duration of 6.5ms. To our knowledge, there are no further works on UPs for LEx, yet.

The GRE acquisitions in Figure 7 demonstrate that the experimental results confirm the simulation results and that the presented UP design software is fully functional. The power of the UP concept with optimized transmit trajectories is clearly demonstrated: Although the depicted subjects were non-database subjects, the UP had a highly similar in vivo performance at 9.4T as the subject specific TPs. Before the TP could be applied, subject specific B_0/B_1^+ mapping and pulse calculation needed to be performed, while the UP could be applied immediately. In all images the red nuclei are excited. For UP and TPs, there is some slight excitation in areas were no excitation was desired. Especially in the TP simulations (Figure 4) this excitation was not visible at all. That leads to the assumption that there are experimental inaccuracies in the transmission of the RF pulse or the execution of the gradient waveform. B_0/B_1^+ map inaccuracies may also be possible[36,45]. The calculated pulses itself should not be responsible for the unwanted excitation, even if it is only slight. These problems should be further investigated and addressed in the future.

Conclusion

We introduced and validated a new pTx pulse design method that optimizes the transmit k-space trajectory (SOS and SPINS) to best match the excitation target of interest prior to calculation of respective UPs or subject specific TPs. OTUP was demonstrated for three different target excitation patterns. The importance of utilizing an optimized target dependent k-space trajectory was emphasized.

For one of the target patterns the resulting pulses were tested in vivo at 9.4T as proof of principle for the integrity of the design method. TPs and UP produced highly similar GRE images, proofing the power of the UP-concept. Both excited the target excitation area, while the surrounding tissues experienced only minor excitation.

The workflow code and the B_0/B_1^+ map data from 18 subjects measured at 9.4T are available online as open source.

Acknowledgements

Funding by the European Union (ERC Starting Grant, SYNAPLAST MR, Grant Number: 679927), the Deutsche Forschungsgemeinschaft (DFG – German Research Foundation) under the Reinhart Kosseleck Programme (DFG SCHE 658/12) and the Cancer Prevention and Research Institute of Texas (Established Investigator Award RR180056) are gratefully acknowledged. Furthermore, we would like to thank the Max Planck Computing & Data Facility in Garching (Germany) for using their Raven-Cluster.

We thank Tingting Shao for kindly providing us with the code the implementation of the 'spatial domain method' is based on.

References

1. Uğurbil K. Imaging at ultrahigh magnetic fields: History, challenges, and solutions. NeuroImage. 2018 Mar; 168: 7–32.

2. Budinger TF, Bird MD, Frydman L, Long JR, Mareci TH, Rooney WD, et al. Toward 20 T magnetic resonance for human brain studies: opportunities for discovery and neuroscience rationale. Magnetic Resonance Materials in Physics, Biology and Medicine. 2016 May; 29: 617–639.

3. Nowogrodzki A. The world's strongest MRI machines are pushing human imaging to new limits. Nature. 2018 Oct; 563: 24–26.

4. Pohmann R, Speck O, Scheffler K. Signal-to-noise ratio and MR tissue parameters in human brain imaging at 3, 7, and 9.4 tesla using current receive coil arrays. Magnetic Resonance in Medicine. 2015 Mar; 75: 801–809.

5. Katscher U, Börnert P, Leussler C, van den Brink JS. Transmit SENSE. Magnetic Resonance in Medicine. 2002 Dec; 49: 144–150.

6. Zhu Y. Parallel excitation with an array of transmit coils. Magnetic Resonance in Medicine. 2004; 51: 775–784.

7. Schneider JT, Kalayciyan R, Haas M, Herrmann SR, Ruhm W, Hennig J, et al. Inner-volume imaging in vivo using three-dimensional parallel spatially selective excitation. Magnetic Resonance in Medicine. 2012 Jun; 69: 1367–1378.

8. Cloos MA, Boulant N, Luong M, Ferrand G, Giacomini E, Bihan DL, et al. kT-points: Short three-dimensional tailored RF pulses for flip-angle homogenization over an extended volume. Magnetic Resonance in Medicine. 2011 May; 67: 72–80.

9. Gras V, Luong M, Amadona A, Boulant N. Joint design of kT-points trajectories and RF pulses under explicit SAR and power constraints in the large flip angle regime. Journal of Magnetic Resonance. 2015 Dec; 261: 181-189.

10. Zelinski AC, Wald LL, Setsompop K, Goyal VK, Adalsteinsson E. Sparsity-Enforced Slice-Selective MRI RF Excitation Pulse Design. IEEE Transactions on Medical Imaging. 2008 Sep; 27: 1213–1229.

11. Grissom WA, Khalighi MM, Sacolick LI, Rutt BK, Vogel MW. Small-tip-angle spokes pulse design using interleaved greedy and local optimization methods. Magnetic Resonance in Medicine. 2012 Mar; 68: 1553–1562.

12. Irarrazabal P, Nishimura DG. Fast Three Dimensional Magnetic Resonance Imaging. Magnetic Resonance in Medicine. 1995 May; 33: 656–662.

13. Malik SJ, Keihaninejad S, Hammers A, Hajnal JV. Tailored excitation in 3D with spiral nonselective (SPINS) RF pulses. Magnetic Resonance in Medicine. 2011 Aug; 67: 1303–1315.

14. Shao T, Xia L, Tao G, Chi J, Liu F, Crozier S. Advanced Three-Dimensional Tailored RF Pulse Design in Volume Selective Parallel Excitation. IEEE Transactions on Medical Imaging. 2012 May; 31: 997–1007.

15. Davids M, Schad LR, Wald LL, Guérin B. Fast three-dimensional inner volume excitations using parallel transmission and optimized k-space trajectories. Magnetic Resonance in Medicine. 2015 Nov; 76: 1170–1182.

16. Kim Dh, Adalsteinsson E, Spielman DM. Simple analytic variable density spiral design. Magnetic Resonance in Medicine. 2003 Jun; 50: 214–219.

17. Schröder C, Börnert P, Aldefeld B. Spatial excitation using variable-density spiral trajectories. Journal of Magnetic Resonance Imaging. 2003 Jun; 18: 136–141.

18. Liu Y, Feng K, McDougall MP, Wright SM, Ji J. Reducing SAR in parallel excitation using variable-density spirals: a simulation-based study. Magnetic Resonance Imaging. 2008 Oct; 26: 1122–1132.

19. Gras V, Vignaud A, Amadon A, Bihan DL, Boulant N. Universal pulses: A new concept for calibration-free parallel transmission. Magnetic Resonance in Medicine. 2016 Feb; 77: 635–643.

20. Gras V, Boland M, Vignaud A, Ferrand G, Amadon A, Mauconduit F, et al. Homogeneous non-selective and slice-selective parallel-transmit excitations at 7 Tesla with universal pulses: A validation study on two commercial RF coils. PLOS ONE. 2017 Aug; 12: e0183562.

21. Wiggins C, Poser B, Mauconduit F, Boulant N, Gras V. Universal Pulses for MRI at 9.4 Tesla - a Feasibility Study. In 2019 International Conference on Electromagnetics in Advanced Applications (ICEAA); 2019 Sep: IEEE.

22. Gras V, Mauconduit F, Vignaud A, Amadon A, Bihan DL, Stöcker T, et al. Design of universal parallel-transmit refocusing kT -point pulses and application to 3D T2 -weighted imaging at 7T. Magnetic Resonance in Medicine. 2017 Nov; 80: 53–65.

23. Gras V, Pracht ED, Mauconduit F, Bihan DL, Stöcker T, Boulant N. Robust nonadiabatic T2 preparation using universal parallel-transmit kT -point pulses for 3D FLAIR imaging at 7 T. Magnetic Resonance in Medicine. 2019 Jan; 81: 3202–3208.

24. Herrler J, Liebig P, Gumbrecht R, Ritter D, Schmitter S, Maier A, et al. Fast online-customized (FOCUS) parallel transmission pulses: A combination of universal pulses and individual optimization. Magnetic Resonance in Medicine. 2021 Jan; 85: 3140–3153.

25. Geldschläger O, Bosch D, Glaser S, Henning A. Local excitation universal parallel transmit pulses at 9.4T. Magnetic Resonance in Medicine. 2021 Jun.

26. Cacciola A, Milardi D, Basile GA, Bertino S, Calamuneri A, Chillemi G, et al. The cortico-rubral and cerebello-rubral pathways are topographically organized within the human red nucleus. Scientific Reports. 2019 Aug; 9.

27. Lewis MM, Du G, Kidacki M, Patel N, Shaffer ML, Mailman RB, et al. Higher iron in the red nucleus marks Parkinson\textquotesingles dyskinesia. Neurobiology of Aging. 2013 May; 34: 1497–1503.

28. Philippens IHCHM, Wubben JA, Franke SK, Hofman S, Langermans JAM. Involvement of the Red Nucleus in the Compensation of Parkinsonism may Explain why Primates can develop Stable Parkinson's Disease. Scientific Reports. 2019 Jan; 9.

29. Grissom W, Yip Cy, Zhang Z, Stenger VA, Fessler JA, Noll DC. Spatial domain method for the design of RF pulses in multicoil parallel excitation. Magnetic Resonance in Medicine. 2006; 56: 620–629.

30. Pauly J, Nishimura D, Macovski A. A k-space analysis of small-tip-angle excitation. Journal of Magnetic Resonance. 1989 Jan; 81: 43–56.

31. Kennedy J, Eberhart R. Particle swarm optimization. In Proceedings of the IEEE International Conference on Neural Networks, Perth, Australia, 1995, #1942-1945.

32. Pedersen ME. Good Parameters for Particle Swarm Optimization.: Luxembourg: Hvass Laboratories; 2010.

33. Setsompop K, Wald LL, Alagappan V, Gagoski BA, Adalsteinsson E. Magnitude least squares optimization for parallel radio frequency excitation design demonstrated at 7 Tesla with eight channels. Magnetic Resonance in Medicine. 2008; 59: 908–915.

34. Hoyos-Idrobo A, Weiss P, Massire A, Amadon A, Boulant N. On Variant Strategies to Solve the Magnitude Least Squares Optimization Problem in Parallel Transmission Pulse Design and Under Strict SAR and Power Constraints. IEEE Transactions on Medical Imaging. 2014 Mar; 33: 739–748.

35. Avdievich NI, Giapitzakis IA, Pfrommer A, Borbath T, Henning A. Combination of surface and `vertical' loop elements improves receive performance of a human head transceiver array at 9.4 T. NMR in Biomedicine. 2017 Dec; 31: e3878.

36. Bosch D, Bause J, Ehses P, Zaiss M, Scheffler K. Rapid pre-saturated TFL transmit field mapping with an optimized 3D centric single-shot readout. In Proceedings of the International Society for Magnetic Resonance in Medicine Meeting 2020 (Virtual Conference), #3703.

37. Griswold MA, Jakob PM, Heidemann RM, Nittka M, Jellus V, Wang J, et al. Generalized autocalibrating partially parallel acquisitions (GRAPPA). Magnetic Resonance in Medicine. 2002 Jun; 47: 1202–1210.

38. Eichfelder G, Gebhardt M. Local specific absorption rate control for parallel transmission by virtual observation points. Magnetic Resonance in Medicine. 2011 May; 66: 1468–1476.

39. Hoffmann J, Henning A, Giapitzakis IA, Scheffler K, Shajan G, Pohmann R, et al. Safety testing and operational procedures for self-developed radiofrequency coils. NMR in Biomedicine. 2015 Apr; 29: 1131–1144.

40. Xu D, King KF, Zhu Y, McKinnon GC, Liang ZP. Designing multichannel, multidimensional, arbitrary flip angle RF pulses using an optimal control approach. Magnetic Resonance in Medicine. 2008 Mar; 59: 547–560.

41. Setsompop K, Wald LL, Alagappan V, Gagoski B, Hebrank F, Fontius U, et al. Parallel RF transmission with eight channels at 3 Tesla. Magnetic Resonance in Medicine. 2006 Nov; 56: 1163–1171.

42. Dupas L, Massire A, Amadon A, Vignaud A, Boulant N. Two-spoke placement optimization under explicit specific absorption rate and power constraints in parallel transmission at ultra-high field. Journal of Magnetic Resonance. 2015 Jun; 255: 59–67.

43. Yip CY, Grissom WA, Fessler JA, Noll DC. Joint design of trajectory and RF pulses for parallel excitation. Magnetic Resonance in Medicine. 2007; 58: 598–604.

44. Davids M, Ruttorf M, Zollner FG, Schad LR. Fast and Robust Design of Time-Optimal k-Space Trajectories in MRI. IEEE Transactions on Medical Imaging. 2015 Feb; 34: 564–577.

45. Pohmann R, Scheffler K. A theoretical and experimental comparison of different techniques for B 1 mapping at very high fields. NMR in Biomedicine. 2012 Sep; 26: 265–275.

Figure captions:

Figure 1: The three target FA pattern to test the workflow. From left to right: targetNuclei, targetM and targetWB. The patterns are displayed by a representative slice in all three orientations (from top to bottom: transversal, sagittal, coronal). For the pulse design, only the voxels between the two horizontal red lines were taken into account for each target pattern, respectively.

Figure 2: Optimized transmit trajectories. In each column, the same basis trajectory (1SOS, 2SOS, 3SOS or SPINS) was utilized, respectively. Each row presents the results for one of the three test target patterns, respectively. For each optimized trajectory the duration of the trajectory (in ms) and the RMSE (in °) that the trajectories enables, is displayed.

Figure 3: Bloch simulated FA profiles of RF pulses designed for different target patterns and different transmit trajectories. In the first row subject specific TPs aiming at excitation of targetNuclei were applied. Each pulse was designed based on another trajectory (depicted in the columns). In the first column, the underlying trajectory was the optimized trajectory for targetNuclei. In the second (third) column, the underlying trajectory was the optimized trajectory for targetM (targetWB). Analog, in row two and three TPs were applied aiming at excitation of targetM and target WB, respectively. Below each profile, the corresponding RMSE and the maximum amplitude of each TP is displayed.

Figure 4: TargetNuclei. The images above present the resulting FA profiles for the corresponding TPs (first row) and UP (second row) for the heads 12-18 (non-database heads for the UP). The bar plot displays the corresponding RMSE values for TPs and UP for the FA profiles from above. The plot below

shows the mean FAs in the excited and non-excited areas from the FA profiles above. The means are depicted by small diamonds. The bars below and above the diamonds present the standard deviations.

Figure 5: TargetM. The images above present the resulting FA profiles for the corresponding TPs (first row) and UP (second row) for the heads 12-18 (non-database heads for the UP). The bar plot displays the corresponding RMSE values for TPs and UP for the FA profiles from above. The plot below shows the mean FAs in the excited and non-excited areas from the FA profiles above. The means are depicted by small diamonds. The bars below and above the diamonds present the standard deviations.

Figure 6: TargetWB. The images above present the resulting FA profiles for the corresponding TPs (first row) and UP (second row) for the heads 12-18 (non-database heads for the UP). The bar plot displays the corresponding RMSE values for TPs and UP for the FA profiles from above. The plot below shows the mean FAs in the excited areas from the FA profiles above. The means are depicted by small diamonds. The bars below and above the diamonds present the standard deviations.

Figure 7: A and B present two different subjects. The structure is the same in both boxes. The images in the left column show the pulse design mask with the target excitation area (yellow) and non-excitation areas (blue) with a representative transversal, sagittal and coronal slice for targetNuclei. The black-white images are GRE acquisitions utilizing the UP and the respective TP for targetNuclei on two non-database head. Only the voxels between the two red horizontal lines on the sagittal and coronal images were taken into account for the pulse design. The numbers above depict the mean signal and standard deviation in desired excitation and non-excitation regions, calculated by means of the masks on the left. The GRE images are expressed in normalized arbitrary unit, i.e. the values of each voxel was divided by the maximum signal values in the whole acquisitions.

Supporting Information Figure S1: A: Left: Central transversal B_1^+ map from each transmit channel of each head. Right: Central sagittal B_1^+ map (sum of all transmit channels) of each head. B: B_0 map of the central transversal and sagittal slice of each head.

Supporting Information Figure S2:

To create a representative analysis of UP performances with differently sized databases (DBs), we ordered the 18 datasets of B_0/B_1^+ maps randomly 500 times. For each order the following design databases were created: DB1 contained the B_0/B_1^+ maps from the first head in the order, DB2 contained the B_0/B_1^+ maps from the first and the second head in the order,…, DB17 contained all but the 18th head in the order.

For each DB and order an 'like UP' was designed utilizing the MLS optimization (33). All pulses were simulated on the respective 18^{th} head in the order, with Bloch simulations neglecting relaxation. As performance measure, we calculated the RMSE between the target excitation FA pattern and the resulting FA pattern.

Both plots belong to the database size investigation for the optimized 2SOS trajectory for targetNuclei. A: Each thin dotted line corresponds to one of the 500 random orders of B_0/B_1^+ maps. It displays the RMSE values the UPs based on DB1,…,UP-DB17 produced on the respective 18^{th} head (non-database head). The bold blue line presents the mean values of the 500 lines for each DB. The bold red lines present the 95% confidence interval (calculated with the percentile method). For instance, for DB11 the mean RMSE is 0.501, while for DB17 the RMSE is 0.487.

B: For each thin dotted line in A, the differences between the RMSE for each DB and DB17, respectively, are displayed by new thin dotted lines. Analog to A, bold blue and red lines depict mean values and 95% CI for each DB size. Blue and red arrows mark certain RMSE values of interest. For a database size of 11, the 97.5% quantile of the differences is 0.068, i.e. lower as 1% of the target excitation FA of 7°. That means for 97.5% of the 500 random orders the UP performance improvement from DB11 to DB17 is below 0.068.

Supporting Information Figure S3: The diagram shows the RMSE values for different sized design databases on the 18th head (a non-database head) for a representative order of B_0/B_1^+ maps. The diagram corresponds to one thin dotted line in Figure S2 A. Additionally, the RMSE for the TP for the 18th head is depicted. For certain database size (DB1, DB2, DB3, DB8, DB9, DB11, DB17) and the TP, the resulting FA profile on the 18th head is shown above. The performance from the pulse for DB9 and DB11 is very similar with the DB17 performance. That means there is no improvement in the performance of an UP calculated based on 11 heads compared to an UP calculated based on 17 heads.

Supporting Information Figure S4: TargetNuclei. The images above present the resulting FA profiles for the corresponding TPs (first row) and UP (second row) for the heads 12-18 (non-database heads for UP). The bar plot displays the corresponding RMSE values for TPs and UP for the FA profiles from above. The plot below shows the mean FAs in the excited and non-excited areas from the FA profiles above. The means are depicted by small diamonds. The bars below and above the diamonds present the standard deviations.

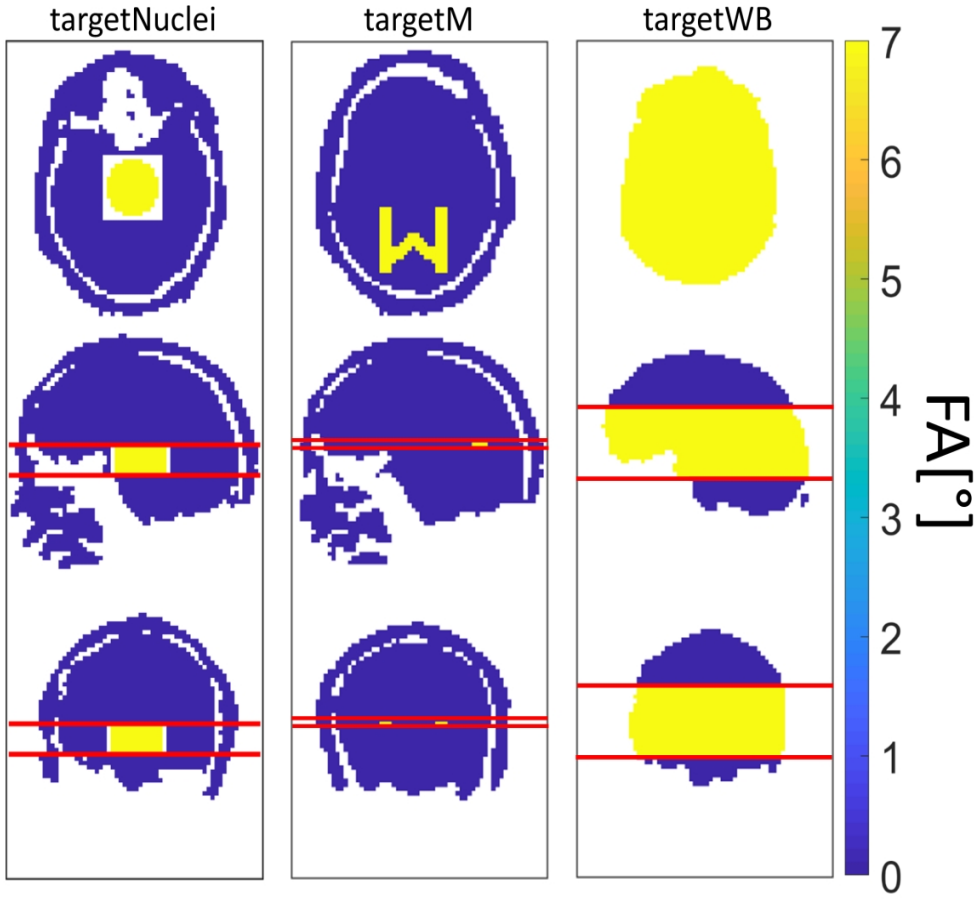

Figure 1: The three target FA pattern to test the workflow. From left to right: targetNuclei, targetM and targetWB. The patterns are displayed by a representative slice in all three orientations (from top to bottom: transversal, sagittal, coronal). For the pulse design, only the voxels between the two horizontal red lines were taken into account for each target pattern, respectively.

183x156mm (300 x 300 DPI)

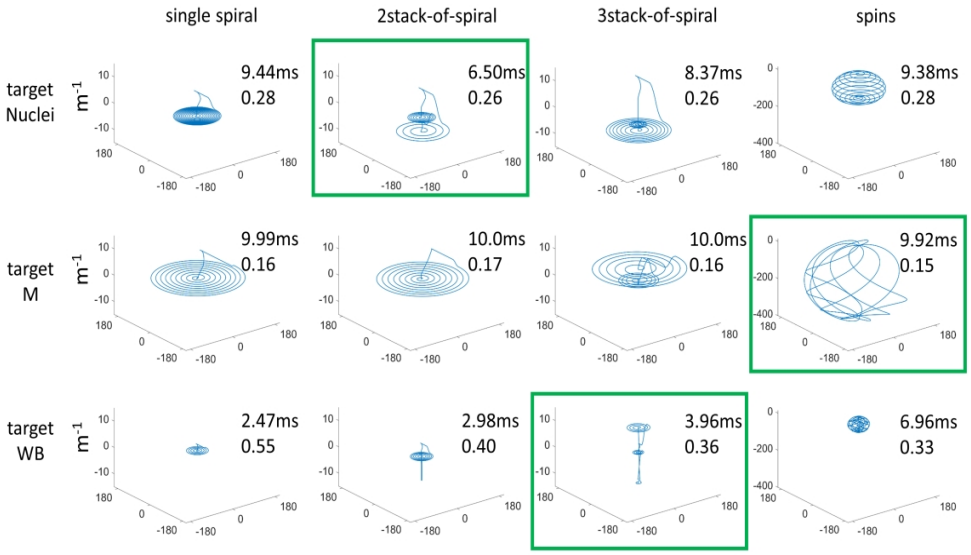

Figure 2: Optimized transmit trajectories. In each column, the same basis trajectory (1SOS, 2SOS, 3SOS or SPINS) was utilized, respectively. Each row presents the results for one of the three test target patterns, respectively. For each optimized trajectory the duration of the trajectory (in ms) and the RMSE (in °) that the trajectories enables, is displayed.

317x164mm (300 x 300 DPI)

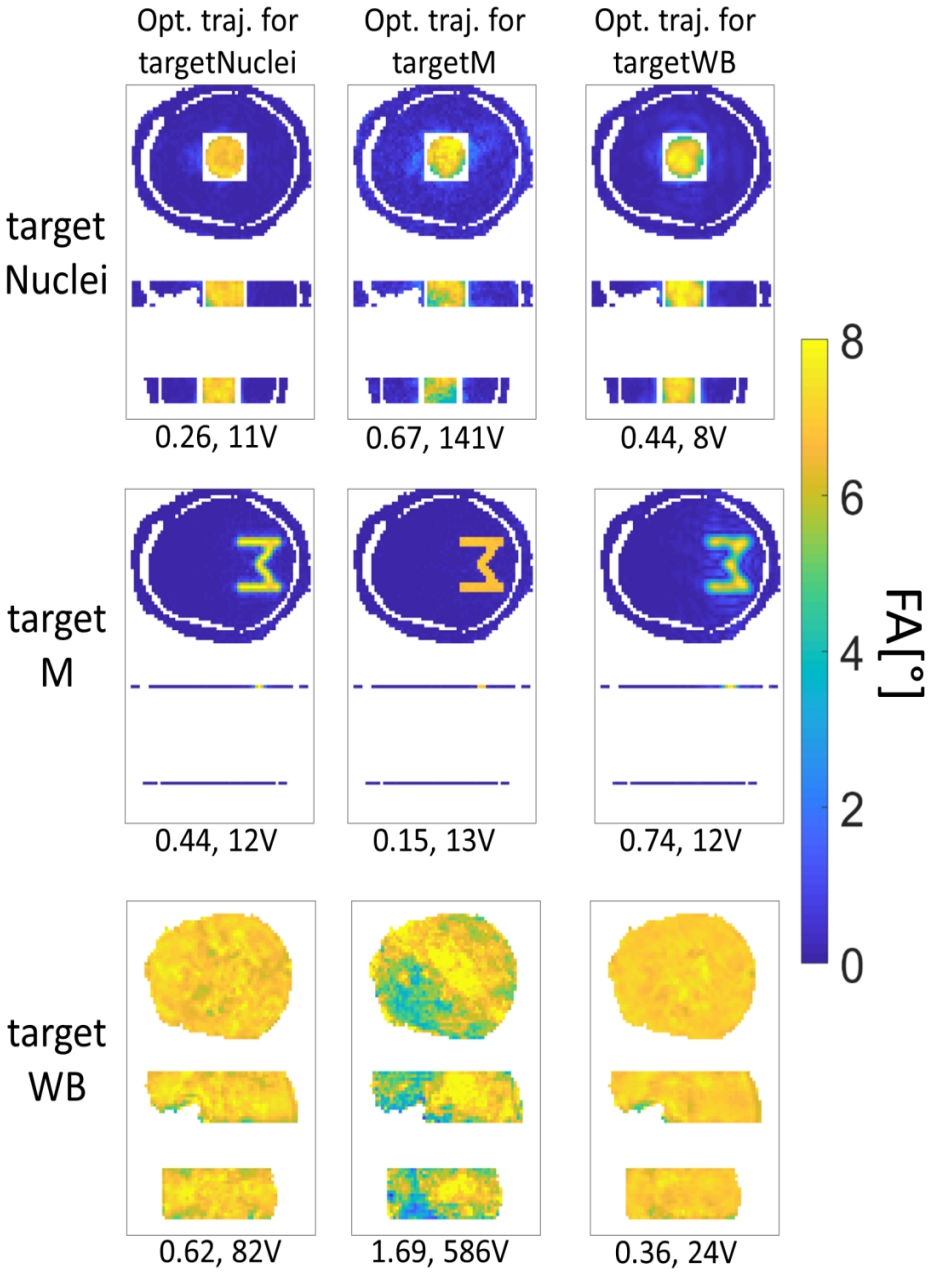

Figure 3: Bloch simulated FA profiles of RF pulses designed for different target patterns and different transmit trajectories. In the first row subject specific TPs aiming at excitation of targetNuclei were applied. Each pulse was designed based on another trajectory (depicted in the columns). In the first column, the underlying trajectory was the optimized trajectory for targetNuclei. In the second (third) column, the underlying trajectory was the optimized trajectory for targetM (targetWB). Analog, in row two and three TPs were applied aiming at excitation of targetM and target WB, respectively. Below each profile, the corresponding RMSE and the maximum amplitude of each TP is displayed.

143x178mm (300 x 300 DPI)

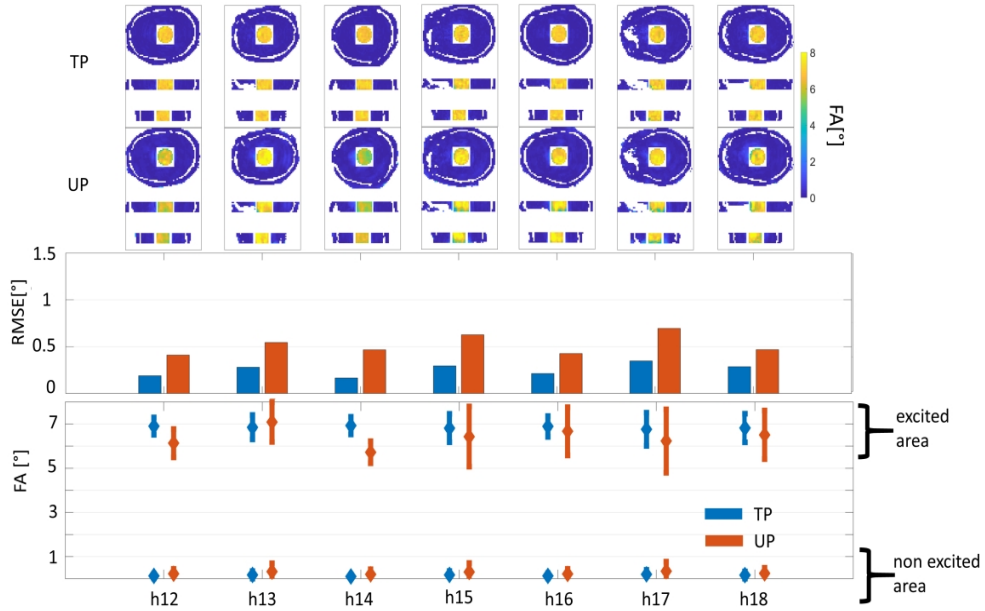

Figure 4: TargetNuclei. The images above present the resulting FA profiles for the corresponding TPs (first row) and UP (second row) for the heads 12-18 (non-database heads for the UP). The bar plot displays the corresponding RMSE values for TPs and UP for the FA profiles from above. The plot below shows the mean FAs in the excited and non-excited areas from the FA profiles above. The means are depicted by small diamonds. The bars below and above the diamonds present the standard deviations.

331x188mm (300 x 300 DPI)

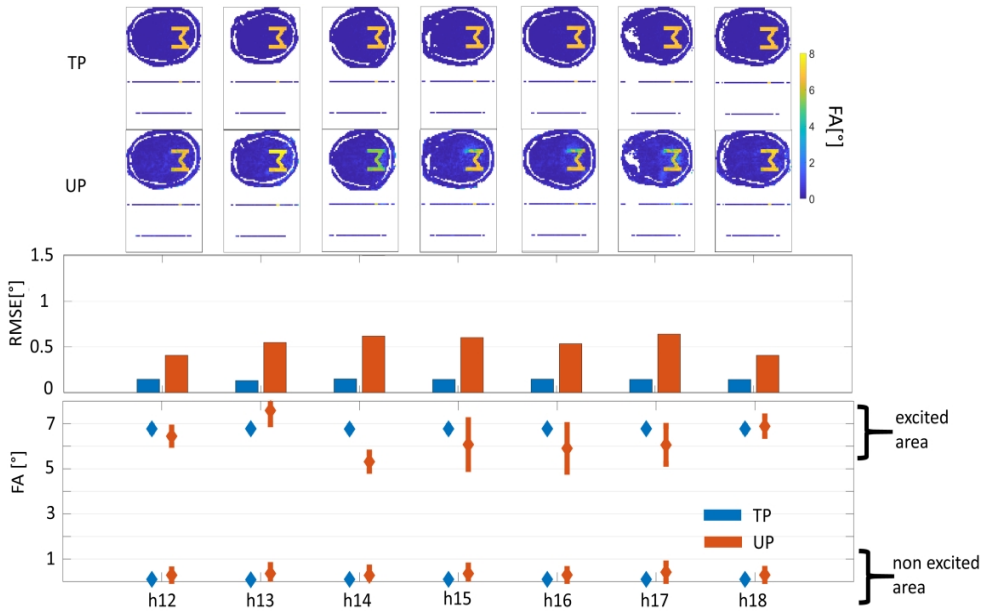

Figure 5: TargetM. The images above present the resulting FA profiles for the corresponding TPs (first row) and UP (second row) for the heads 12-18 (non-database heads for the UP). The bar plot displays the corresponding RMSE values for TPs and UP for the FA profiles from above. The plot below shows the mean FAs in the excited and non-excited areas from the FA profiles above. The means are depicted by small diamonds. The bars below and above the diamonds present the standard deviations.

330x188mm (300 x 300 DPI)

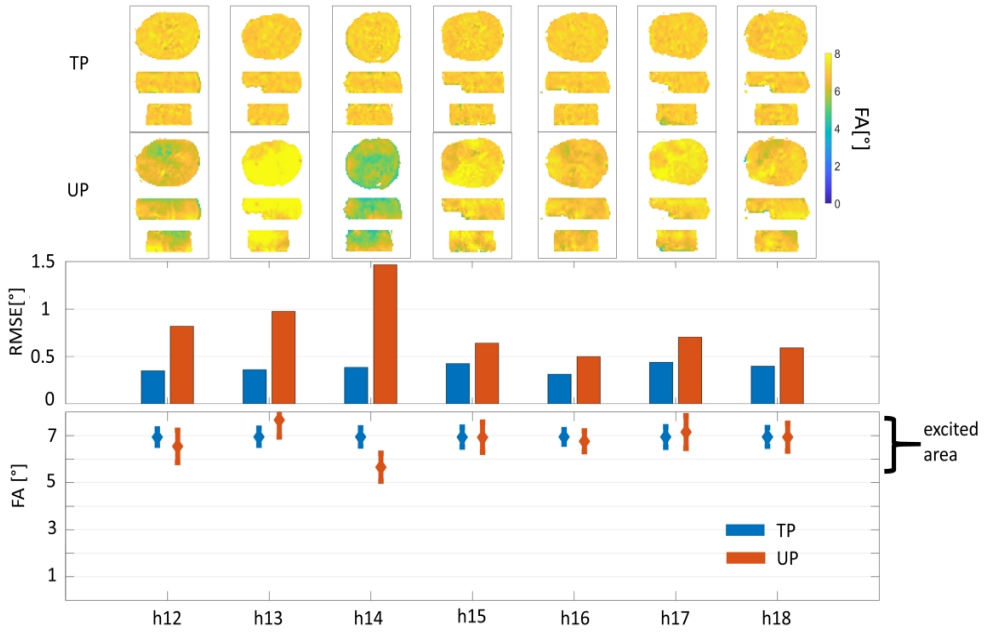

Figure 6: TargetWB. The images above present the resulting FA profiles for the corresponding TPs (first row) and UP (second row) for the heads 12-18 (non-database heads for the UP). The bar plot displays the corresponding RMSE values for TPs and UP for the FA profiles from above. The plot below shows the mean FAs in the excited areas from the FA profiles above. The means are depicted by small diamonds. The bars below and above the diamonds present the standard deviations.

320x187mm (300 x 300 DPI)

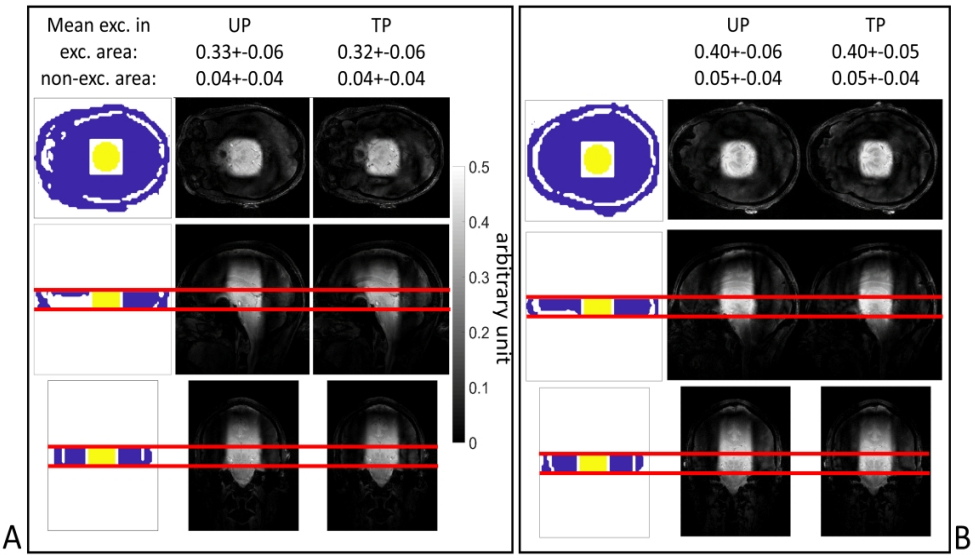

Figure 7: A and B present two different subjects. The structure is the same in both boxes. The images in the left column show the pulse design mask with the target excitation area (yellow) and non-excitation areas (blue) with a representative transversal, sagittal and coronal slice for targetNuclei. The black-white images are GRE acquisitions utilizing the UP and the respective TP for targetNuclei on two non-database head. Only the voxels between the two red horizontal lines on the sagittal and coronal images were taken into account for the pulse design. The numbers above depict the mean signal and standard deviation in desired excitation and non-excitation regions, calculated by means of the masks on the left. The GRE images are expressed in normalized arbitrary unit, i.e. the values of each voxel was divided by the maximum signal values in the whole acquisitions.

305x158mm (300 x 300 DPI)

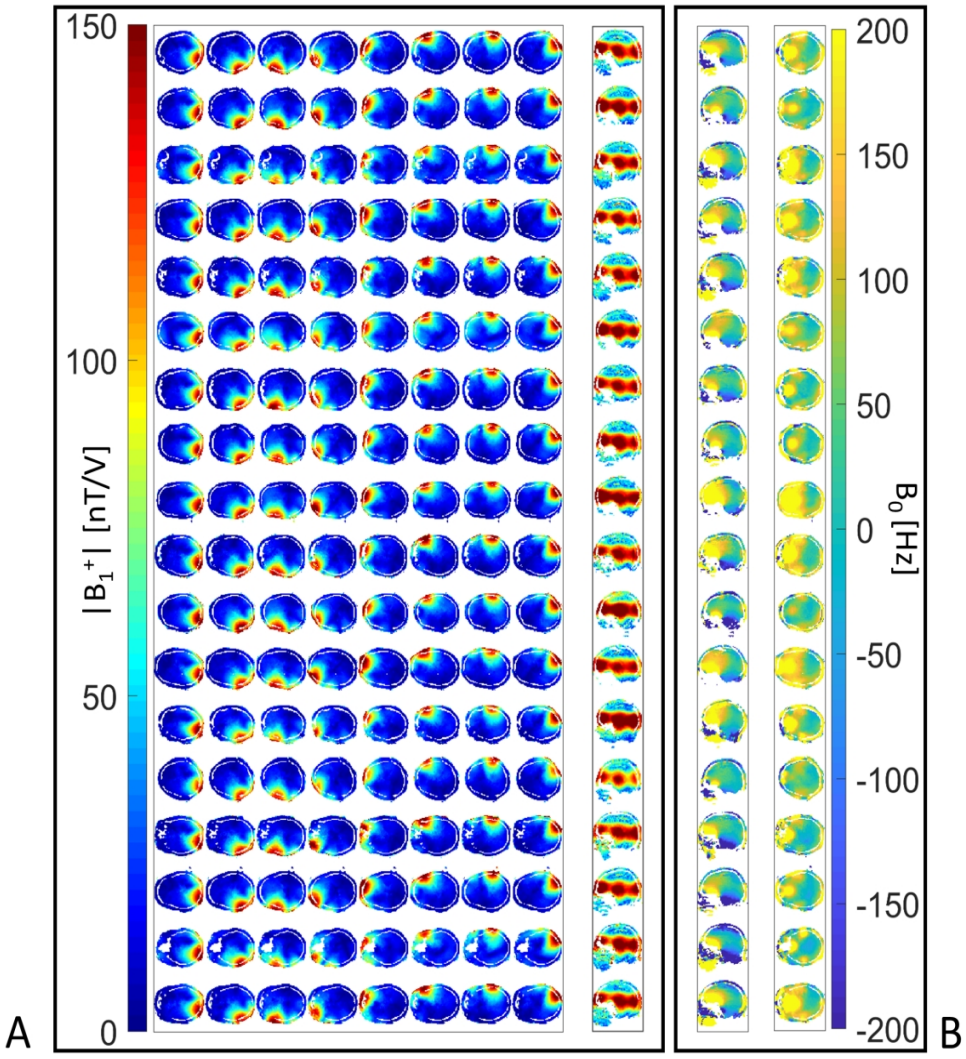

188x187mm (300 x 300 DPI)

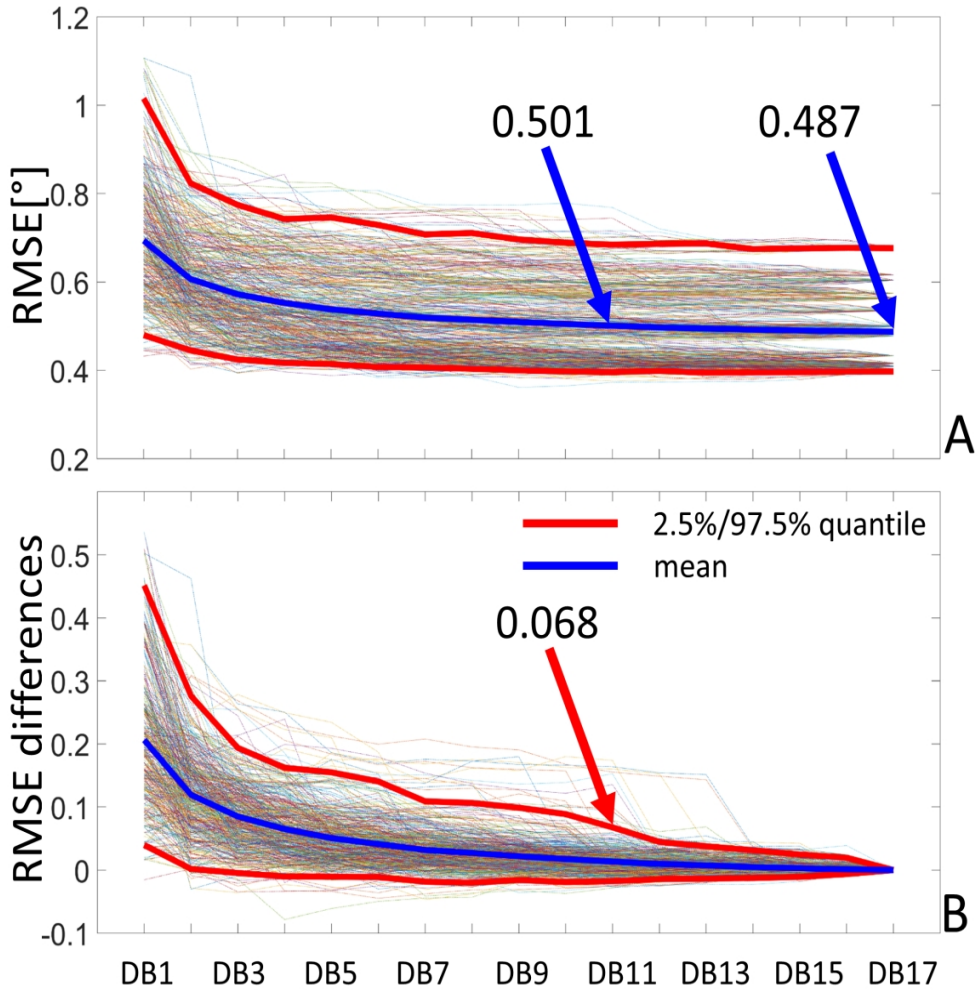

189x175mm (300 x 300 DPI)

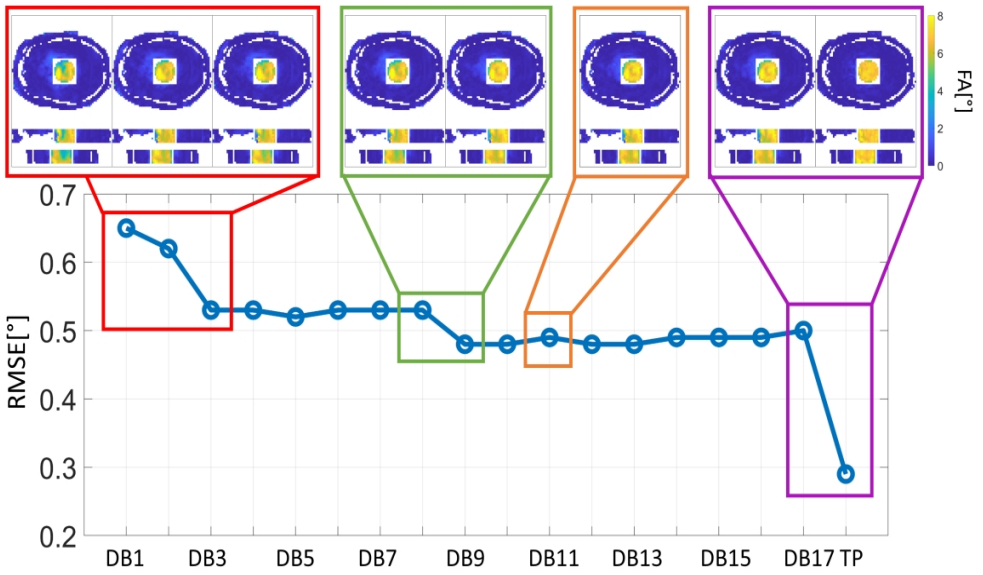

320x170mm (300 x 300 DPI)

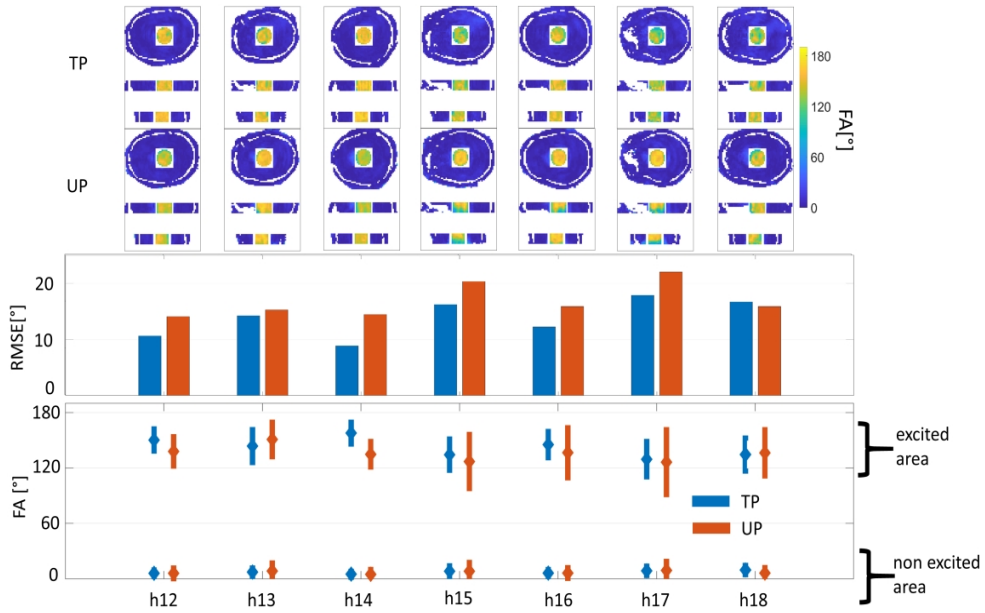

330x188mm (300 x 300 DPI)